

**NORTHWESTERN UNIVERSITY**

**Multiscale Plasmonic Metamaterials**

**A DISSERTATION**

**SUBMITTED TO THE GRADUATE SCHOOL  
IN PARTIAL FULFILLMENT OF THE REQUIREMENTS**

**for the degree**

**DOCTOR OF PHILOSOPHY**

**Field of Chemistry**

**By**

**Joel Henzie**

**EVANSTON, ILLINOIS**

**December 2007**

**ABSTRACT****MULTISCALE PLASMONIC METAMATERIALS****Joel Henzie**

Metallic nanostructures are able to confine and manipulate electromagnetic fields because light can couple to free electron oscillations called surface plasmons (SPs). These plasmons exist on metal surfaces as localized (short-range) or as propagating (long-range) modes depending upon the size and geometry of the nanostructure. This dichotomy is primarily an issue of scale that has largely been studied with sample geometries dominated by one type of plasmon mode. We believe this difference in length scale provides a unique opportunity to design new plasmonic nanostructures with effective, tunable optical properties by organizing metallic building blocks over multiple length scales. This approach takes advantage of both propagating and confined plasmon modes in the same nanoscale system, with tunable coupling between different SPs. This dissertation describes a new set of techniques for high-throughput nanofabrication based on soft lithography. We have generated metallic structures that expand on the fundamental science of surface plasmons, and our major observations include: (i) metallic pyramids with nanoscale tips that exhibit multipolar optical resonances depending on the direction and polarization of the incident light. (ii) SP standing waves between microscale arrays of nanoscale holes that enhance light transmission through the holes by a factor of 8X. (iii) Plasmonic metamaterials that exhibit optical properties by changing the lattice spacings of subwavelength nanohole arrays. (iv) Ultra-

narrow, hybridized plasmon resonances and far-field beaming with finite-arrays of nanoholes. Such unique metallic structures have established a better understanding of the relationship between localized and propagating SPs and now enable an accessible platform for applied studies in nanophotonics and single molecule imaging.

## ACKNOWLEDGEMENTS

I would like to thank everyone at Northwestern University for creating a truly engaging and stimulating community while I lived there and conducted my research. Teri Odom has been an outstanding advisor who gave me immeasurable support and intellectual freedom. This work would have been impossible without the help of wonderful collaborators including Professor George Schatz, Dr. Stephen Gray, Dr. Eun-Soo Kwak, Professor Shih-Hui Chang, Dr. Kevin Shuford, Hanwei Gao, Min Hyung Lee, and Jeff McMahan. I also would like to thank my Ph.D committee—Vinayak Dravid, Chad Mirkin, Mark Ratner, and George Schatz—who gave me a critical view of my research and helped guide me in the right direction.

My earliest research experience was as an undergraduate in the lab of Professor Catherine Chia at the University of Nebraska-Lincoln. I would like to thank her for teaching me how to work with cells (in particular *Dictyostelium discoideum*) because it gave me a level of patience and hand-eye coordination that is difficult to obtain in a chemistry lab. Throughout my thesis work I've continually been told that it is infinitely more difficult for a biologist to become a chemist than the other way around. Whether this is true or not, my experience in the NSF-REU program at Columbia University with Professor Kenneth Eisenthal and Professor Alex Benderskii (now at Wayne State) solidified my desire to make the transition to chemistry in part because of their generous explanations of complex physical phenomena. I think this is also the place where I developed a curiosity for high-tech scientific instruments.

The entire Odom lab has been a well of support during my thesis work. I was the 6<sup>th</sup> member to join a group that was instantly welcoming and helpful. I miss the days of making

PDMS hands and dropping a piece of dry ice in the sink to make the lab look more aesthetically pleasing. It was nice to have that core group of people—Liza Babayan, Jeremy Barton, Eric Greyson, Perumal Sekar, and Chris Stender—to chat with and think of new and crazy ideas. In particular I would like to thank Dr. Eun-Soo Kwak who was my collaborator, friend, and ally during parts of my tumultuous first two years in the group. Hanwei Gao and Min Hyung Lee have been outstanding collaborators, associates and friends with whom I will always have time to split a pitcher of beer and talk about science.

I would also like to thank my family for their support. They have helped me through all my years of schooling and talked me through some really tough parts. I promise to call more frequently now that I am finished. I would also like to thank Miss Ling Ma, who has been my closest friend and strongest support for greater than three years now. Her impact in my life has been limitless.

## TABLE OF CONTENTS

<b>Abstract</b> .....	2
<b>Acknowledgements</b> .....	4
<b>Table of Contents</b> .....	7
<b>List of Figures</b> .....	9

## CHAPTER 1

### INTRODUCTION TO NANOPATTERNING AND ITS IMPACT ON THE SCIENCE OF PLASMONIC METAMATERIALS .....

1.1 Introduction.....	18
<i>1.1.1 Brief Primer on Surface Plasmons</i> .....	20
<i>1.1.2 Conventional Methods to Plasmonic Structures</i> .....	22
1.2 Soft Lithography and Metal Nanostructures .....	23
1.3 Subwavelength Arrays of Nanoholes: The Archetype of Plasmonic Metamaterials .....	25
1.4 Summary and Future Outlook .....	27

## CHAPTER 2

### NANO- AND MICROSCALE METALLIC PYRAMIDS WITH NANOSCALE TIPS.....

2.1 Introduction.....	30
2.2 Fabrication of Metallic Pyramids with Nanoscale Tips.....	32

2.3	Encapsulation and Manipulation of Pyramid Arrays.....	40
2.4	Optical Characterization of Pyramid Arrays.....	43
2.5	Conclusion and Future Outlook.....	49

## CHAPTER 3

### FABRICATION OF ANISOTROPIC METALLIC PYRAMIDS AND THEIR OPTICAL PROPERTIES .....51

3.1	Introduction.....	52
3.2	Fabrication of Nanohole Arrays by PEEL.....	53
3.3	Characterization of Nanohole Films with NSOM.....	55
3.4	Modeling a Typical NSOM Experiment with FDTD.....	63
3.5	Measuring Enhanced Light Transmission Through Metallic Nanohole Arrays .....	64
3.6	Ultra-narrow Resonances Generated by Microscale Arrays of Nanoholes.....	67
3.7	Conclusion and Future Outlook.....	69

## CHAPTER 4

### MULTISCALE PATTERNING OF PLASMONIC METAMATERIALS.....70

4.1	Introduction.....	71
4.2	Fabrication and Characterization of Plasmonic Metamaterials.....	72
	4.2.1 Preparation of SIL PDMS Photomasks.....	72
	4.2.2 Soft Interference Lithography.....	72
	4.2.3 Fabrication of multiscale subwavelength nanohole array films by PEEL.....	75

4.2.4	<i>Optical characterization of nanohole arrays</i> .....	76
4.3	Multiscale Arrays of Nanoscale Holes.....	76
4.4	Au Nanohole Patches with Large Separations.....	83
4.5	Concentrating Light with Nanohole Patches.....	86
4.6	Metal Enhanced Fluorescence with Nanohole Patches .....	88
4.7	Multiscale Patterning of Metal and Dielectric Nanoparticles.....	91
4.8	Conclusion and Future Outlook.....	95
<b>CHAPTER 5</b>		
<b>MULTISCALE PATTERNING OF PLASMONIC METAMATERIALS</b> .....		
97		
5.1	Introduction.....	98
5.2	Fabrication of Nano-OLEDs.....	99
5.2.1	<i>Synthesis of Ru(bpy)<sub>3</sub>(BF<sub>4</sub>)<sub>2</sub></i> .....	99
5.2.2	<i>Fabrication of nanohole arrays in SU-8</i> .....	100
5.2.3	<i>Fabrication of ITO line arrays</i> .....	101
5.2.4	<i>Device Fabrication</i> .....	101
5.3	Characterization of Nano-OLEDs .....	104
5.4	Conclusion and Future Outlook.....	106
<b>REFERENCES</b> .....		107
<b>APPENDIX I</b> .....		120
<b>VITA</b> .....		121

## LIST OF FIGURES

- Figure 1.1.** Plasmonic Nanostructures. (A) Subwavelength bull's eye structure. (B) Ring resonator. (C) Gold stripe and nanoparticle waveguides. (D) Silver cubes. (E) Silver nanowires. (F) Gold stars. ....19
- Figure 1.2.** Different types of surface plasmons. (A) Surface plasmon polaritons at a metal-dielectric interface. (B) Localized surface plasmons on a metal nanoparticle excited by free-space light. ....21
- Figure 2.1.** Scheme illustrating the pyramid fabrication procedure. ....33
- Figure 2.2.** SEM images of the fabrication procedure for Ni pyramids. (A) Holes in Cr on Si(100) are etched, exposing the pyramidal Si pits (B). (C) Ni was deposited (inset bottom, image tilted 15°), followed by a Cr-etch to lift-off the nanohole film and expose (D) the Ni pyramids (inset bottom, image tilted 25°). ....34
- Figure 2.3.** SEM images of metallic pyramids of a single material after removal from the Si template. (A) 50-nm thick Ni pyramids aligned using a magnetic field. (B) 50-nm thick Ni pyramids isolated using a magnet. (inset) Zoom-in of a tip with  $r < 10$  nm. (C) 250-nm thick Ni pyramids. (inset) Zoom-in of a tip with  $r < 10$  nm. (D) 30-nm thick Au pyramids. (inset) Zoom-in of a tip with  $r < 8$  nm. ....36
- Figure 2.4.** SEM images of pyramids composed of multiple materials. (A) Two-toned pyramids with a 50-nm Au outer shell and a 50-nm Ni inner shell. (inset)

- Zoom-in showing the smooth edges of the pyramid faces. **(B)** Three-layer pyramids of 70 nm Ni in between 40 nm layers of Au. (inset) A tip from one these structures with  $r < 2$  nm. ....38
- Figure 2.5.** SEM image of a 100-nm diameter Au pyramids generated by PEEL using an SIL mask. (inset) Zoom-in showing a nanoscale pyramid. ....39
- Figure 2.6.** Scheme depicting the transfer and encapsulation of Au pyramids in a PDMS film. ....41
- Figure 2.7.** SEM images of the key manipulation steps. **(A)** 250-nm diameter Au pyramids situated in the centers of etched Si pits spaced by  $\sim 2$   $\mu\text{m}$ . **(B)** Etched Si(100) pedestals supporting the Au pyramids. **(C)** Au pyramids transferred and partially embedded within the PDMS film. **(D)** Etched Si(100) pedestals after removal of the pyramids. The dimensions of all insets are  $1 \mu\text{m} \times 1 \mu\text{m}$ . **(E)** Optical micrograph of a  $1\text{-cm}^2$  pyramid array encapsulated in a thin PDMS film. ....42
- Figure 2.8.** Optical characterization of Au pyramids in an array whose plane is *perpendicular* to the optical axis of the microscope (orientation I). **(A)** Illustration depicting the geometry of the particle array, the black arrow indicates the direction of the white light source while the gray area denotes the plane of the particle array. **(B)** DF microscope image of encapsulated Au pyramids with tips pointing directly at the white light source. **(C)** DF spectrum of the array of Au pyramids. **(D)** Calculated scattering cross

section of an Au pyramidal shell structure in this orientation with the polarization parallel to the base (orientation **I**). **(E)** DF spectrum of an array of 100-nm diameter Au pyramids spaced by 400-nm (center-to-center) in orientation **I**. **(F)** Calculated scattering cross section of the pyramids in **(E)**. .....44

**Figure 2.9.** Optical characterization of Au pyramids in an array whose plane is now *parallel* to the optical axis of the microscope (orientation **II**). **(A)** DF microscope image of Au pyramids oriented on their sides and whose tips point perpendicular to the white light source. The black arrow in the inset image indicates the direction of the optical axis, and gray area denotes the plane of the particle array. **(B)** DF spectra of the Au pyramids in **(A)** illuminated with white light that is polarized parallel to the pyramid base (upward-pointing triangle) and polarized perpendicular to the pyramid base (left-pointing triangle). The inset shows how the pyramids in the array are oriented in **(A)**, and  $\mathbf{k}$  denotes the propagation wavevector, which is parallel to and down the array plane. Both spectra are plotted on the same scale. **(C)** Calculated scattering cross section of a single Au pyramidal shell in this orientation for two perpendicular polarizations. ..47

**Figure 3.1.** **(A)** Scheme depicting the PEEL procedure. **(B)** PEEL generates both nanopyramids and nanohole arrays. ....54

**Figure 3.2.** **(A)** Optical micrograph of  $\sim 1 \text{ in.}^2$  free-standing film placed on a glass substrate. **(B)** and **(C)**, SEM images of representative areas of the film

illustrating the uniformity of the patterning. **(D)** SEM image of a single nanohole whose nearest neighbor hole is 15  $\mu\text{m}$ . .....56

**Figure 3.3.** Near-field and far-field optical images and calculations. **(A)** NSOM optical image of holes in a 100-nm Au film on glass. The image was acquired at a 200 x 200 pixel resolution at 5 ms/pixel scan rate using an Al-coated probe (tip aperture  $\sim 70$  nm, Veeco) with an unknown, but fixed, polarization. **(B)** Calculated near-field SPP standing wave pattern at the Au/air interface for four 200-nm holes, on a 1.6  $\mu\text{m}$  x 1.6  $\mu\text{m}$  array, and for a 100-nm Au film supported on glass. **(C)** Calculated far-field intensity of four holes. The fringe spacing of  $\lambda_w \sim \lambda_{pp}/2$  is present but is relatively smaller in amplitude compared to the transmission through the holes. **(D)** Cross-section of two neighboring holes from **(A)**. The standing waves between the holes have a period of  $\lambda_w \sim 322$  nm. ....57

**Figure 3.4.** NSOM images of 50-nm Au films with 250-nm holes that were illuminated using **(A)**  $\lambda_{ex} = 633$  and **(B,C)**  $\lambda_{ex} = 800$  nm light. The use of longer wavelength light effectively increases the thickness of the film, so that SPP standing waves can be observed. The white arrows indicate the polarization direction of the tip. **(B)** Polarization is parallel to the light from the tip. **(C)** Polarization is perpendicular to the light from the tip. ..60

**Figure 3.5.** Structural and optical properties of bi-layered and multi-layered films. **(A)**, SEM image of holes in a Au/Ni (50 nm/50 nm) film. The tilt angle is 35°. **(B)** and **(C)**, NSOM images of Au/Ni film with polarization parallel

and perpendicular to the light from the tip. The arrows indicate the direction of polarization, and the direction of the fringes flips as the polarization changes in orthogonal directions. (D), SEM image of 200-nm holes in a Au/Ni/Au (40/20/40) film. The tilt angle is  $25^\circ$ . (E), Cross-section of two neighboring holes in a 40/70/40 film imaged under local  $\lambda_{\text{ex}} = 633 \text{ nm}$  and  $\lambda_{\text{ex}} = 800 \text{ nm}$  light. The period  $\lambda_{\text{sw}}$  of the SPP standing wave between the holes increases as the excitation wavelength increases. ....61

- Figure 3.6.** Transmittance of gold films, isolated holes, and nanohole arrays. Solid films (+) and single holes (■) in 180 nm thick films exhibit only an intraband transition peak at 500 nm. 250-nm hole arrays ( $a_0 \sim 2 \mu\text{m}$ ) in 180-nm films (●) and 100-nm films (▲) exhibit a SPP band centered around 615 nm. ....65
- Figure 3.7.** Transmission of nanohole Au films in different refractive index environments. ....68
- Figure 4.1.** Optical micrograph of a  $14\text{-cm}^2$  array of 100-nm diameter Si posts ( $h$  and  $a_0 = 400 \text{ nm}$ ) prepared by interference lithography; (inset) SEM image zoom. This pattern was used as a master for preparing SIL PDMS photomasks. ....73
- Figure 4.2.** Scheme depicting the fabrication procedure of infinite nanohole arrays and finite-sized arrays (patches) of holes with PEEL and soft interference lithography (SIL). ....74

- Figure 4.3.** The optical setup (A) for characterizing the nanohole arrays. Optical micrographs of light transmission seen through an (B) Au and (C) Si subwavelength nanohole film generated by SIL. ....77
- Figure 4.4.** SEM images of (A) infinite Au nanohole array, (B) infinite Si nanohole array, (C) Au patch nanohole array and (D) Si patch nanohole array. The nanohole patches are separated by 4.5  $\mu\text{m}$ . All films were 50 nm thick and supported on glass. Zero-order transmission spectra of (E) an infinite Au hole array ( $\blacksquare$ ), patch hole array ( $\blacktriangleleft$ ), and solid film ( $\blacksquare$ ) and (F) an infinite Si hole array ( $\blacksquare$ ), patch hole array ( $\blacktriangleleft$ ), and solid film ( $\blacksquare$ ). 78
- Figure 4.5.** Refractive index sensing using Au nanohole arrays. (A) Zero-order transmission of infinite Au hole arrays on glass in air (refractive index,  $n = 1.0$ ) and in the presence of higher index immersion liquids ( $n = 1.000 - 1.7000$ ). The peaks shifted to longer wavelengths with higher  $n$  and split into multiple peaks at Wood's anomalies. The relative amplitude of peaks also changed as  $n$  increased. The image inset is 3.2  $\mu\text{m}$  x 5.2  $\mu\text{m}$ . (B) Zero-order transmission of patches of Au gold nanoholes on glass in air and in the presence of the same immersion liquids used in (a). Both films were 50 nm thick. Right inset depicts the narrowest resonance from the 2.5- $\mu\text{m}$  Au patches at  $n = 1.6$ . Left image inset is 3.2  $\mu\text{m}$  x 5.2  $\mu\text{m}$ . ....80
- Figure 4.6.** SEM images (top) and zero-order transmission spectra (bottom) of an isolated (A) 2.5- $\mu\text{m}$  Au patch, (B) a 5- $\mu\text{m}$  Au patch, and (C) a 10- $\mu\text{m}$  Au

patch in contact with the same liquids as in Fig. 3. The spectra for a given patch have been shifted linearly (0.07-0.10 units) for clarity. All films were 50-nm thick. ....84

**Figure 4.7.** Table summarizing the transmission of Au and Si patches of nanoholes. 87

**Figure 4.8.** Metal enhanced fluorescence from 1- $\mu\text{m}$  diameter fluorescent polystyrene beads on nanohole patches. (A) SEM image of a 10- $\mu\text{m}$  diameter Au nanohole patch ( $a_0 = 20 \mu\text{m}$ ,  $t = 50 \text{ nm}$ ) on a glass substrate. (B) Transmission image of beads on nanohole patch films. The beads are located on the patch (1) and the bare Au film (2). (C) TIRF image of the same beads shows bright fluorescence emission from the beads located on the patch. (D) Cross-section of the fluorescence intensity indicates that the bead fluorescence is enhanced by a factor of 1.6 .....90

**Figure 4.9.** (A) Scheme depicting the fabrication of large-area single and multi-layered nanoparticle arrays using SIL Au nanohole films as deposition masks. (B) SEM image of a Au nanoparticle array ( $d = 100 \text{ nm}$ ,  $h = 50 \text{ nm}$ ); (inset) image zoom. (C) DF scattering spectra for metal (Ag, Cu, Au) and dielectric (Si) nanoparticles ( $d = 100 \text{ nm}$ ,  $h = 50 \text{ nm}$ ). The scattering peaks were scaled to the height of the Ag peak as indicated on the graph. (D) DF scattering spectra for multi-layered metal/dielectric nanoparticle arrays in air ( $n = 1$ ); Au/Al<sub>2</sub>O<sub>3</sub> ( $\blacktriangle$ :  $h = 25/30 \text{ nm}$ ), Al<sub>2</sub>O<sub>3</sub>/Au ( $\blacksquare$ :  $h = 55/25 \text{ nm}$ ), and Au/Al<sub>2</sub>O<sub>3</sub>/Au ( $\bullet$ :  $h = 25/30/25 \text{ nm}$ ). (E) DF scattering spectra of the multi-layered nanoparticles in (D) surrounded by different

- refractive index liquids. ....92
- Figure 4.10.** (A) SEM image of a 10 x 10- $\mu\text{m}$  square of Au nanoparticles ( $h = 65 \text{ nm}$ ) fabricated using a nanohole patch film with a 25- $\mu\text{m}$  pitch. (B) DF scattering image of Cu (left) and Ag (right) nanoparticles ( $h = 15 \text{ nm}$ ) fabricated on a different portion of the mask used in (A). (C) DF image of Au (left) and Ag (right) nanoparticles ( $h = 65 \text{ nm}$ ) fabricated using a 10- $\mu\text{m}$  circular nanohole patch film. ....94
- Figure 5.1.** (A) Scheme for defining the anode area for fabricating nano-OLEDs. (B) Scheme for patterning addressable nano-OLEDs. ....102
- Figure 5.2.** (A) Optical micrograph of 250-nm circular openings in SU-8 (inset: AFM image of a single nanohole). (B) EL image of nano-OLEDs operated at 3.9 V. (C) Photograph of large-area emission from the nano-OLED array. (D) EL spectra of nano-OLEDs ( $\blacktriangle$ , orange line) and macroscale OLEDs ( $\blacksquare$ , green line). ....103
- Figure 5.3.** (A) SEM image of 250-nm circular openings in SU-8 patterned on 350-nm wide ITO lines spaced by 15  $\mu\text{m}$ . The dark spots indicate where the holes are in contact with the ITO lines. (B) EL image of an array of addressable nano-OLEDs. (C) EL image of an individually addressed row of nano-OLEDs (inset

**CHAPTER 1**  
**INTRODUCTION TO NANOPATTERNING AND ITS IMPACT ON PLASMONIC**  
**METAMATERIALS**

## 1.1 Introduction

Plasmonics is a field that encompasses the science and applications of noble metal structures that can guide and manipulate light at the nanometer scale. This area was so-named because it is an analog of photonics; instead of controlling light with dielectric materials, light is controlled by metal structures via plasmons, collective free electron oscillations.<sup>1</sup> Beyond these semantics, one of the early driving forces for research in plasmonics was the discovery that highly confined electromagnetic fields, in the form of propagating surface plasmons, could provide an alternative approach for miniaturizing optical devices while carrying electrical signals at optical frequencies.<sup>2</sup> Such properties are possible because plasmons, unlike photons, are not subject to the classical diffraction limit ( $\sim\lambda/2$ ).<sup>3</sup> Not surprisingly, the design of plasmonic devices was inspired by the fabrication techniques and device architectures of photonic ones, and plasmonic devices could also perform similar functions, but at physical dimensions approaching the length scales of the modern transistor.<sup>4,5</sup> Prototype devices such as waveguides,<sup>6,7</sup> interferometers,<sup>8</sup> demultiplexers,<sup>9</sup> and plasmonic bandgap crystals<sup>10</sup> have been demonstrated (**Figure 1A-C**).<sup>11</sup>

Rapid progress in plasmonics can be attributed to a combination of breakthroughs over the past decade, including: (1) Imaging tools. Near-field scanning optical microscopy enabled direct imaging of surface plasmon waves,<sup>12</sup> and optical microscopes outfitted with dark field scattering capabilities allowed localized surface plasmon resonances to be correlated with individual metal nanoparticles.<sup>13</sup> (2) Theoretical tools. Optimized electrodynamic calculation methods as well as improved computational resources have made detailed theoretical descriptions of the observed optical properties possible. (3) Nanomaterials methods. Advances in synthetic and fabricated

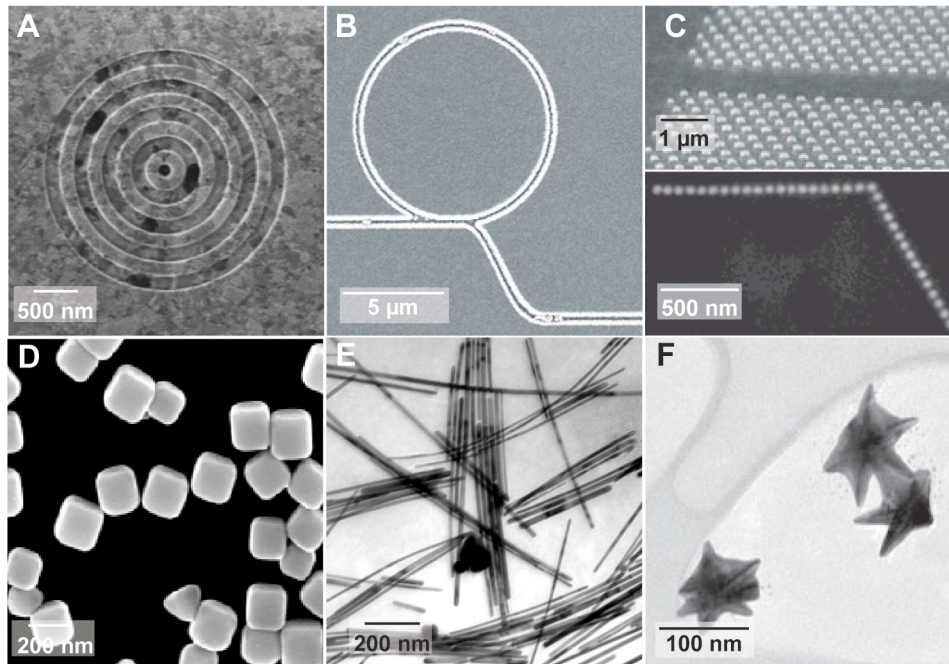


**Figure 1.1** | Plasmonic Nanostructures. (A) Subwavelength bull's eye structure.<sup>14</sup> (B) Ring resonator.<sup>15</sup> (C) Gold stripe<sup>16</sup> and nanoparticle waveguides.<sup>17</sup> (D) Silver cubes.<sup>18</sup> (E) Silver nanowires.<sup>19</sup> (F) Gold stars.<sup>20</sup>

approaches to produce nanostructures have allowed control over the shape and size of noble metal (Au, Ag, Cu) structures (**Figure 1D-F**). In particular, the development of nanofabrication tools capable of sub-100 nm resolution has played a key role in enabling groundbreaking discoveries in plasmonics: the demonstration of enhanced optical transmission through subwavelength hole arrays,<sup>21</sup> the collimation of light through a subwavelength bull's-eye structure,<sup>22</sup> negative permeability and refraction at visible wavelengths,<sup>23,24</sup> and second harmonic generation from magnetic metamaterials.<sup>25</sup>

This chapter will focus on how new types of nanofabrication tools, based on soft lithography, can generate a wide range of plasmonic structures with exceptional optical properties. There are two important features of these tools: (1) they provide a scalable and inexpensive approach to create arrays of complex metal structures (nanoholes and nanoparticles), and (2) they expand the types of plasmonic metamaterials that are possible because the metallic building blocks can now be organized over multiple length scales and over macroscale areas.

### ***1.1.1 Brief Primer on Surface Plasmons***

The optical properties of metals are determined in part by the resonant interaction between light and their surface free electrons at a metal-dielectric interface. These collective electron oscillations or charge density waves—surface plasmon polaritons (SPPs)—exist as propagating waves on planar metal films (**Figure 2A**). The amplitude of the SPPs extend farther in the dielectric region compared to the metal region. In order to excite SPPs on a surface using free-space light, additional momentum must be provided either by patterning a grating structure on the film or by evanescent coupling of light into the metal.<sup>26</sup> The propagation distance of SPPs

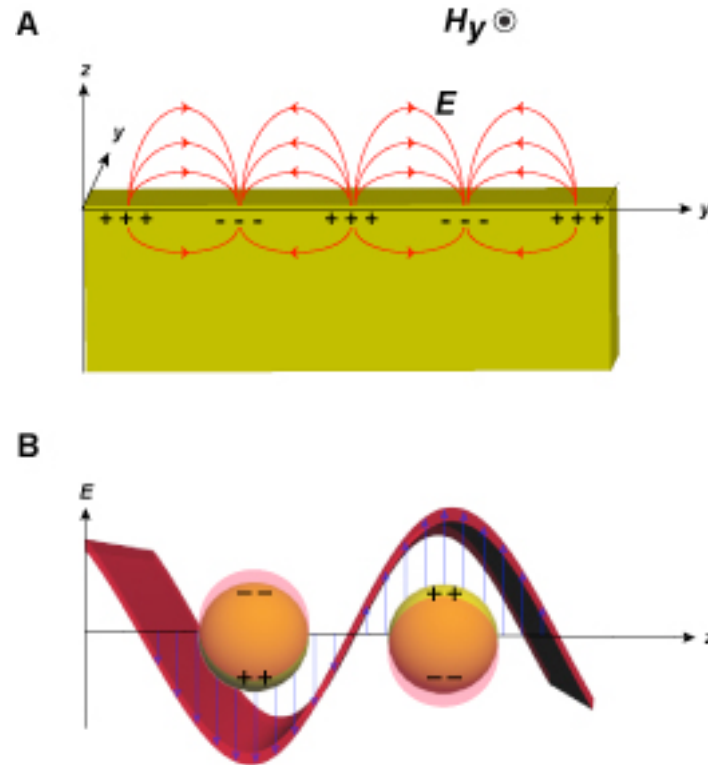


**Figure 1.2** | Different types of surface plasmons. **(A)** Surface plasmon polaritons at a metal-dielectric interface. **(B)** Localized surface plasmons on a metal nanoparticle excited by free-space light.

depends primarily on the absorption of the metal and the thickness and surface roughness of the film; for SPPs on Au films excited using 633-nm light, this decay length is around 10  $\mu\text{m}$ .<sup>27,28</sup>

Metal particles (< 250 nm in diameter) also interact strongly with light through plasmons that are confined within ca. 10 nm of the particle surface (**Figure 2B**); these resonant optical fields are called localized surface plasmons (LSPs). LSP resonances are highly sensitive to the size,<sup>29</sup> shape,<sup>30</sup> and dielectric environment of the metal particles and can be tuned from ultra-violet to near-infrared (NIR) wavelengths.<sup>31</sup> Spherical particles with sizes less than 50 nm support single LSP resonances that are dipolar in character, and their optical properties can be described reasonably well by the lowest order term in Mie theory.<sup>32</sup> In addition, slightly larger anisotropic particles (100-nm diameter Au pyramids) exhibit only a dipole resonance in contrast to pyramids with sizes of 250 nm or larger.<sup>33</sup> Rod-shaped Au nanoparticles can support both transverse and longitudinal modes depending on polarization.<sup>34,35</sup> Larger metallic particles (overall sizes > 100 nm) with anisotropic shapes can exhibit multiple LSP resonances<sup>36,37</sup> that correspond to higher order plasmon modes.<sup>38</sup> These multi-polar excitations depend on the direction of the wavevector as well as the polarization vector,<sup>39</sup> thus, certain excitation angles can allow selected resonances to be more pronounced.<sup>40</sup>

### ***1.1.2 Conventional Methods to Plasmonic Structures***

Chemical synthesis has been the primary means to grow a wide variety of metal nanoparticle shapes (**Figure 1D-F**), including prisms, stars, rods, boxes, and cages, because reaction conditions such as temperature, surfactants, and precursors can be independently controlled.<sup>41</sup> Although solution-based methods are scalable, the large distribution in nanoparticle

shape and size within a single reaction vessel is a challenge. Metal particles can also be assembled into two- (2D) and three-dimensional (3D) lattices using a variety of techniques; both the interparticle distances and the geometry of the lattices can be used to tune the optical properties of the assemblies.<sup>42-45</sup>

Nanofabrication methods offer an alternative strategy to organize plasmonic structures into arrays. Direct-write techniques such as electron-beam lithography can fabricate linear and 2D arrays of nanoparticles with different spacings,<sup>46,47</sup> which typically need to be on the order of the size of the particle or less ( $< 200$  nm) for efficient dipolar coupling.<sup>48</sup> Focused ion beam (FIB) milling has been the most common method to fabricate hole and slot structures in optically thick metal films.<sup>21</sup> This method can drill all the way or partially through the film and can control the diameter and spacing of the structures with reasonable precision (ca. 100 nm). Free-standing suspended films have also been fabricated by FIB and reactive ion etching, but the generation of multi-layered metal films is difficult and laborious.<sup>49</sup> Although serial lithographic methods have been instrumental for fabricating prototype structures whose unique properties opened the field of plasmonics, the patterned areas were small (hundreds of square microns) and access to multi-scale structures is limited. Soft lithography can meet these challenges.

## **1.2 Soft Lithography and Metal Nanostructures**

Soft lithography is a catch-all term for fabrication techniques that use wafer-scale (several square inches) poly (dimethylsiloxane) (PDMS) stamps or masks to transfer patterns from one material or surface to another.<sup>50</sup> To extend these capabilities to produce sub-100 nm features, the mechanical properties of the PDMS were improved,<sup>51</sup> and composite PDMS stamps composed

of a thin, stiff layer of hard *h*-PDMS supported by a thick slab of 184 PDMS were developed.<sup>52-</sup>

<sup>57</sup> Soft lithographic methods offer three important advantages over the serial ones described in *section 1.1.2* to produce plasmonic structures: (1) Parallelism. PDMS molded against a master forms a transparent, elastomeric mask that can be used to create arrays of structures simultaneously. (2) Simplicity. Only widely available microfabrication techniques are required, including photolithography, wet chemical etching, e-beam deposition, reactive ion etching, and microtoming.<sup>58</sup> (3) Flexibility. Patterns can be generated with various symmetries and spacings, out of multiple materials, and with exquisite control over the thickness of each layer.

The most widely used soft lithographic approach to fabricate metal nanostructures starting from metal films involves micro-contact printing followed by chemical etching.<sup>59,60</sup> Here, a PDMS stamp is “inked” with an alkanethiol solution and then brought into conformal contact with a noble metal surface; the molecules are transferred from the stamp to the metal and self-assemble into a monolayer (SAM) with the same pattern as the stamp. These patterned SAMs can function as etch masks for the underlying metal film, and thus after subjected to a chemical etch, the protected metal patterns have the same characteristics as the PDMS stamp. A range of metal nanostructures have been generated, from arrays of 90-nm lines that acted as linear polarizers to slots in metal films that could be used as frequency selective surfaces.<sup>61</sup> One variation on this printing and etching method is decal transfer lithography, where the bas-relief patterns on a PDMS stamp are first chemically bonded to the metal surface.<sup>62</sup> When the PDMS stamp is removed from the surface, remnants of PDMS remain on the substrate (and, as a drawback, the pattern on the stamp is destroyed). These PDMS surface-patterns can then act like etch masks to produce metal patterns identical to those on the original PDMS stamp.

Another strategy to produce metal nanostructures is to deposit the metal directly on patterned PDMS stamps or polymeric structures using sputtering, e-beam or thermal evaporation. In nano-transfer printing, a thin layer of Au is deposited on the patterned PDMS using line-of-sight deposition and then placed on a chemically modified surface.<sup>63</sup> When the stamp is removed, only the gold portions in contact with the surface remain. If, however, the deposited metal is allowed to accumulate on the sidewalls of the pattern (through a combination of sample rotation and angled deposition), films that follow the complex 3D topography of the stamp can be fabricated and then released to yield free-standing structures.<sup>64</sup> High aspect-ratio metal nanostructures can also be produced if the metal patterns on the PDMS mold are sectioned with a microtome tool; the optical properties of such structures depend strongly on the polarization of the incident light.<sup>65</sup> Composite structures can also be fabricated by depositing a thin (50 nm) Au layer on arrays of 500-nm diameter wells molded in a polymeric substrate. This hole-particle system exhibits interesting properties in the NIR because the LSPs of the nanoparticles in the wells interact with the SPPs of the hole film on the top surface.<sup>66</sup>

### **1.3 Subwavelength Arrays of Nanoholes: The Archetype of Plasmonic Metamaterials**

The wireless flow of information in modern societies has its origins in the 19<sup>th</sup> and early 20<sup>th</sup> century with the discovery of the laws of electromagnetism. These laws describe the interaction of electromagnetic (EM) waves with different materials such as metals and insulators, which is central to technologies such as radios, cellphones, and the television. Metal antennae are able to transmit and receive EM waves because the free electrons in conductors oscillate in response to external electrical fields. The key design principles for antennae depend on size and shape; in

general, the size of an antenna determines the wavelengths it can operate at, and its shape determines the direction it can transmit and receive signals. So, as the range of usable EM waves began to spread from the long wavelengths of radio waves to shorter wavelengths like the infrared, new classes of antennae were developed to accommodate them. Technologies using microwaves became important during the 1940's when Britain was developing microwave frequency radar components during World War II. During that time, Hans Bethe developed a theory of diffraction of EM waves by small apertures (or holes) in perfectly conducting films.<sup>67</sup> He predicted that microwave transmission through subwavelength apertures in opaque metal films was expected to be very small, with intensities proportional to  $(r/\lambda)^4$  based on geometric optics.<sup>68</sup>

Bethe's theoretical study set the precedent for experiments using subwavelength apertures across the entire EM spectrum. It was not until the discovery of enhanced optical transmission through subwavelength hole arrays by Thomas Ebbesen in 1998 that Bethe's prediction was called into question. These measurements revealed that optical transmission through nanohole arrays could exceed predictions by orders of magnitude, and moreover, showed that the wavelength of transmission could be tuned by changing the material of the film, hole size, and the array spacing and geometry. Light incident on the nanohole array can resonantly couple to SPPs on the metal film. These SPPs can then tunnel through the holes and emerge from the opposite side and be converted back into free-space light. The wavelength of transmission is given by an approximate equation for the SPP Bloch waves ( $\lambda_{\text{SPP}}$ )

$$\lambda_{SPP} = \frac{a_0}{\sqrt{i^2 + j^2}} \sqrt{\frac{\epsilon_{Au} \epsilon_d}{\epsilon_{Au} + \epsilon_d}}$$

where  $a_0$  is the periodicity of the nanoholes,  $i$  and  $j$  are integers that define the particular order of the Bloch modes,  $\epsilon_{Au}$  is the dielectric constant of the Au, and  $\epsilon_d$  is the dielectric constant of the surrounding dielectric material. SPPs were first discovered in 1957 by measuring energy loss of fast electrons passing through metal films.<sup>69</sup> Since Bethe's model used an ideal metal that was perfectly conducting, it could not support SPPs.<sup>70</sup>

The relationship between Bethe's work in antenna theory and Ebbesen's work in subwavelength optics is important because both fields share similar concepts that size, shape, and periodicity are directly related to the operating wavelength of the structure. The connection between subwavelength hole arrays and metamaterials was made by Pendry et al.,<sup>71</sup> because the features of these structures can be fabricated so that their size is far smaller than the wavelength of light. Such a structure is an optical metamaterial because it behaves as a homogenous medium—its optical properties do not change between two points within the material—and can be described by effective medium theory. Optical metamaterials, operating at visible frequencies, only recently became available as new nanopatterning techniques made it possible to pattern below 100-nm.

#### 1.4 Summary and Future Outlook

Fundamental plasmonics research is laying the foundation for future technologies in diverse areas ranging from optics to electronics to imaging. To meet these challenges and to

advance the science forward, however, the methods by which plasmonic nanostructures are constructed need to be simplified and made scalable. Multiscale patterning—and soft interference lithography in particular—provides a first step towards realizing new types of plasmonic architectures because (1) microscale ordering can be imposed on the nanoscale patterns, and thus plasmonic coupling strengths can be tuned and (2) complexity of plasmonic metamaterials can be built-up simply by starting with a different master. The prospect for multiscale plasmonic structures is considerably bright. In the short term, because they support intense and concentrated electromagnetic fields, plasmonic materials can be used for highly sensitive refractive index sensing using films with arrays of nanoholes as well as multiplexed, label-free detecting and screening of analytes using arrays of particles. In the long term, active or hybrid plasmonic metamaterials will become important for understanding how plasmons can enhance or manipulate the properties of non-linear media, and such metamaterials combined with superresolution imaging techniques could yield an unprecedented platform for studying biological processes of a cell.

## **CHAPTER 2**

### **NANO- AND MICROSCALE METALLIC PYRAMIDS WITH NANOSCALE TIPS**

## 2.1 Introduction

The optical properties of noble metals depend critically on their size and shape at the nanoscale. Solution-phase syntheses provide a flexible route to different metallic nanoparticles by using variables such as reaction temperature, surfactants, and precursor concentration, enabling the careful tuning of their optical properties.<sup>30,35</sup> The properties of anisotropic nanoparticles can be quite different from spherical particles of similar sizes because surface plasmon resonances are extremely sensitive to the nanoscale topography of the particle in addition to its dielectric environment.<sup>29,30,73</sup> Theoretical studies have shown that very sharp points—tips—in noble metals can concentrate electromagnetic fields, which can dominate the optical properties of nanostructures.<sup>74-77</sup> A common drawback of solution-based syntheses of noble metal nanoparticles, however, is the formation of various other shapes in addition to that of the desired product. With structures so small, any slight variation in the size or shape from particle-to-particle changes the measured spectra of a large ensemble of particles.<sup>13</sup> Spherical particles with sizes less than 50 nm support single local surface plasmon (LSP) resonances that are dipolar in character. Accordingly, their optical properties can be explained reasonably well by the lowest order term in Mie theory.<sup>78</sup>

In contrast, larger metallic particles (diameters > 100 nm) with anisotropic shapes can exhibit multiple LSP resonances<sup>36,37</sup> that correspond to higher order modes.<sup>38</sup> Observations of these resonances in submicron particles have only recently been enabled by improved chemical methods to synthesize high-quality crystals and fabrication techniques to generate particles with uniform sizes and shapes. Before these methods, random dispersion of different-shaped particles in solution ensured that all resonant plasmon modes were measured simultaneously, and thus

some peaks were obscured because of polarization averaging. Multipolar excitations can, however, depend on the direction of the wavevector and polarization vector;<sup>75</sup> thus, certain excitation angles can make selected resonances more pronounced.<sup>40</sup> Strategies that can both isolate particles and control their orientation are essential to correlate the orientation of the particles with specific plasmon modes directly. Drop-coating or spin-casting dilute colloidal solutions onto glass slides has resulted in isolated particles although their orientation on the substrate was not well-defined,<sup>79</sup> and asymmetric particles were generated by electroless deposition but were closely spaced and still attached to the supporting Au film.<sup>80</sup> Electron beam (e-beam) lithography can create isolated particles with multipolar resonances, but the shapes are limited to two-dimensional (2D) planar shapes.<sup>81</sup>

Sacrificial templates are useful for molding the size and shape of interesting free-standing nano- and mesostructures. Typically, solid and supported structures, such as nanometer-sized pores in anodized alumina membranes or micrometer-sized etched pits in silicon, are used as templates. Electrodeposition of conducting materials or molding of polymers is used to reproduce the shape and structure of the template; the templates are then removed by the appropriate etchants. Free-standing structures such as metallic (and multilayered) rods, pyramidal tips for scanning probe applications, and micrometer-sized metallic pyramidal shells can be produced from solid templates.<sup>82-86</sup> The pyramidal shells were found to exhibit tips with a radius of curvature ( $r$ ) as small as 50 nm.<sup>86</sup> Other types of templates, including silica spheres, have recently been used to fabricate metallic structures with unusual shapes. Such structures were generated by e-beam deposition of metal onto silica spheres followed by etching of the sphere template. Submicrometer “half-shells” made from different metals as well as “crescent

moon” structures with sharp edges in silver were produced.<sup>87,88</sup> The edges of these silver shell structures enhanced the local electromagnetic field, and the Raman scattering of rhodamine 6G from isolated, individual crescent moon structures could be detected.<sup>88</sup>

## 2.2 Fabrication of Metallic Pyramids with Nanoscale Tips

**Figure 2.1** outlines the **PEEL** procedure for generating metallic pyramids within the etched pits of a silicon (100) substrate, using a Cr-film patterned with sub-250 nm holes as *both* the etch mask and deposition mask.<sup>89</sup> PEEL is a patterning method that is a combination of **P**hase-shifting photolithography (PSP), **E**tching, **E**lectron-beam deposition, and **L**ift-off of the film to generate pyramidal nanostructures and nanohole films simultaneously.<sup>90</sup> First, a square array (covering  $\sim 1 \text{ in.}^2$ ) of photoresist posts (typical diameters  $\sim 250 \text{ nm}$ ; smallest diameters  $\sim 100 \text{ nm}$ ) was patterned on a silicon (Si) wafer using PSP. In brief, these posts were formed by exposing photoresist (Shipley 1805) through a *h*-PDMS mask patterned with a square array of dots<sup>91-93</sup> and removing the exposed resist with 351 Microposit developer. 20 nm of Cr was deposited by e-beam on these photoresist posts, and lift-off of the resist was achieved by sonicating the pattern in acetone. Round holes, with very smooth edges, were formed in the Cr-film (**Figure 2.2A**). Next, we anisotropically etched the exposed Si with a KOH/isopropyl alcohol (IPA) solution to form pyramidal pits underneath the Cr-nanoholes (**Figure 2.2B**). We took advantage of this undercutting to fabricate pyramids *smaller* than the size of the etched pyramidal pits and defined by the size of the Cr-hole. The smoothness and circular symmetry of the nanoholes in the Cr-etch mask are crucial in forming symmetrical (square) pyramidal pits.

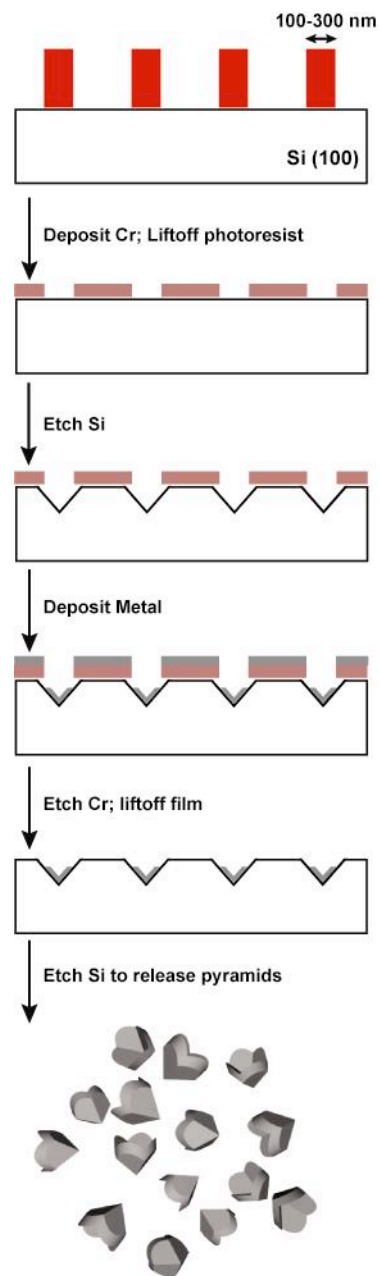


**Figure 2.1** | Scheme illustrating the pyramid fabrication procedure.

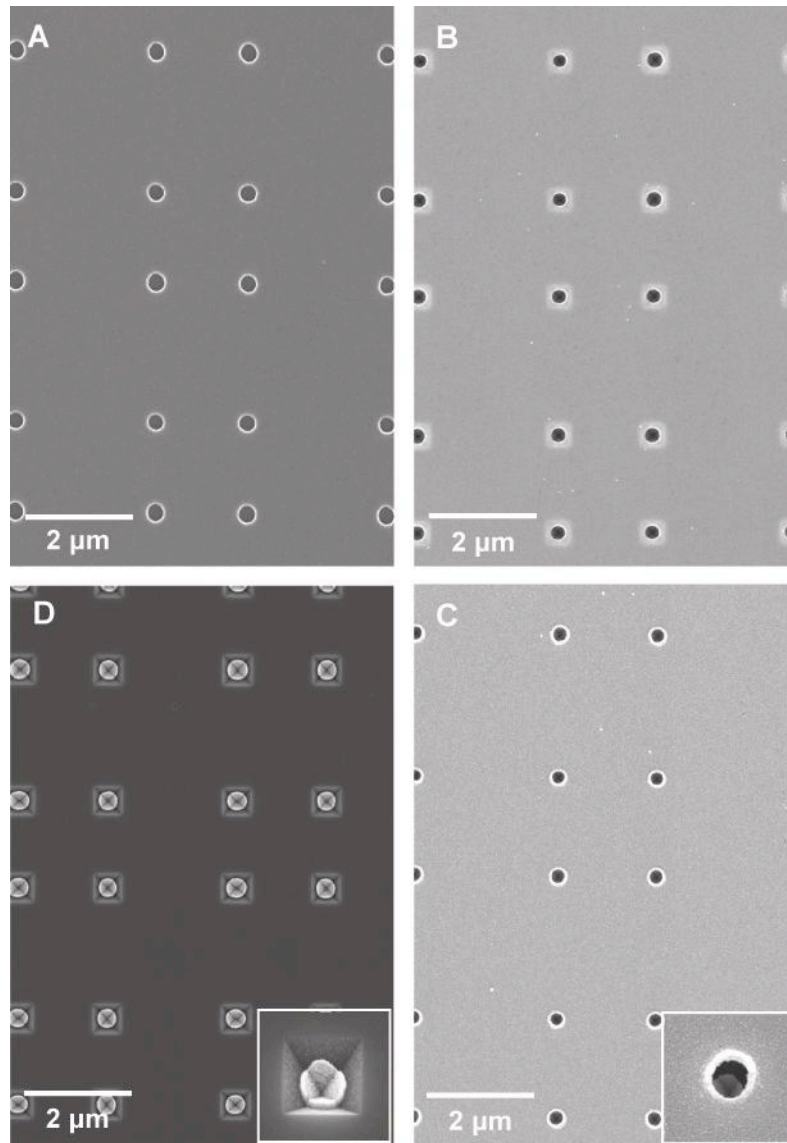


**Figure 2.2** | SEM images of the fabrication procedure for Ni pyramids. (A) Holes in Cr on Si(100) are etched, exposing the pyramidal Si pits (B). (C) Ni was deposited (inset bottom, image tilted 15°), followed by a Cr-etch to lift-off the nanohole film and expose (D) the Ni pyramids (inset bottom, image tilted 25°).

Oblate or rough Cr-holes produced rectangular or irregularly shaped pyramids. We then used the Cr-mask as a deposition mask and evaporated 50-nm Ni film (1-4 Å/s) onto these patterns (**Figure 2.2C**); to fabricate pyramids composed of different materials, we needed to deposit a different material at this step. The patterned samples were placed in the evaporator so that they were line-of-sight with the evaporation source; the film thickness was monitored with a quartz crystal microbalance. Finally, we etched the Cr-film with a commercial etchant (Transene Corp., Danvers, MA) to reveal Ni pyramids (50 nm thick and ~250 nm across their base) situated within the centers of the silicon pyramidal pits (**Figure 2.2D**). The monodispersity of the pyramids was estimated by the differences in the sizes of the Cr-holes. From SEM images taken at over seven different and representative locations over a large sample, we estimate a monodispersity of ~5%.

In order to release the Ni-pyramids from the silicon template, we etched this pattern with KOH/IPA (**Figure 2.3A**). For our patterned area (pyramids spaced  $2\ \mu\text{m} \times 2\ \mu\text{m}$  over  $1\ \text{in.}^2$ ), we generated  $\sim 10^8$  pyramids/inch<sup>2</sup>. These mesoscale pyramids can be isolated using a ~1 T SmFeB magnet or centrifugation (3000 rpm for 5 minutes). Since Ni is a hard magnetic material, the 50-nm thick pyramids could be isolated with the strong magnet. Pyramids that were pre-magnetized in the Si template tended to align in chains after release because their remnant magnetization assisted in their alignment (**Figure 2.3A**). Ni pyramids that were not pre-magnetized tended to clump together (**Figure 2.3B**). Importantly, a majority (> 99.9%) of the pyramidal tips we observed had a radius of curvature  $r < 10\ \text{nm}$  (**Figure 2.3B**, inset). The facets of the Ni-pyramids are remarkably smooth. We propose that the exposed, crystalline Si(111) planes of the pyramidal pits assisted in molding and merging the Ni grains as they are deposited onto the surface.

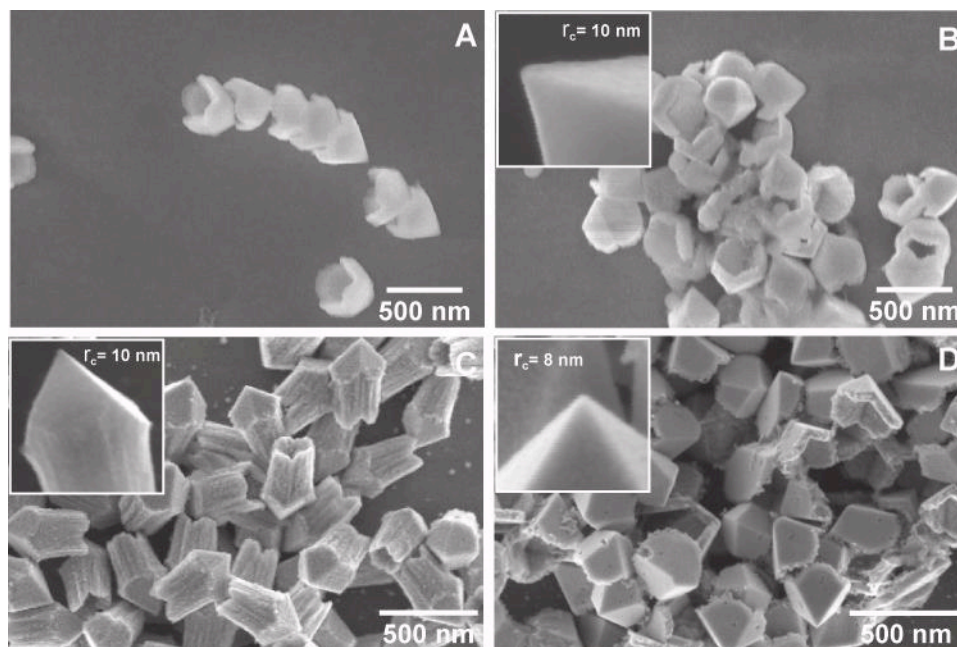


**Figure 2.3** | SEM images of metallic pyramids of a single material after removal from the Si template. (A) 50-nm thick Ni pyramids aligned using a magnetic field. (B) 50-nm thick Ni pyramids isolated using a magnet. (inset) Zoom-in of a tip with  $r < 10$  nm. (C) 250-nm thick Ni pyramids. (inset) Zoom-in of a tip with  $r < 10$  nm. (D) 30-nm thick Au pyramids. (inset) Zoom-in of a tip with  $r < 8$  nm.

We also used this procedure to fabricate pyramids with much thicker side-walls; 250 nm of Ni was deposited through the Cr-mask of holes (**Figure 2.3C**). Certain distinct features of these arrow-like particles indicated the mechanism of the pyramid formation: (i) the ridges or notches along the shaft of the arrow reproduced exactly the granular structure of the Cr deposition mask (**Figure 2.3C**, inset); (ii) the diameter of the shaft became smaller along the length of the particle, which indicated that the Cr-holes were decreasing in size; and (iii) the interior of the shaft was grainy because the metal is no longer depositing directly against a smooth surface. Because of their unique shape, these types of three-dimensional particles would be difficult to fabricate by other nanofabrication routes. In addition to Ni pyramids, we fabricated 50-nm thick Au pyramids using our method (**Figure 2.3D**). The smoothness of the facets and the sharpness of the tips (we observed tips with  $r < 8$  nm) make them ideal structures for studying the local electromagnetic field enhancement of noble metal tips.

One of the greatest advantages (besides creating nanoscale tips) of our nanofabrication procedure is our ability to control both the materials and chemical functionality of these pyramids. We have used the layer-by-layer feature of e-beam deposition to create multi-layered pyramids with variable thicknesses. To create two-layered pyramids, we evaporated 25 nm of Au and then 25 nm of Ni through the same Cr-deposition mask (**Figure 2.4A**). The right inset image (tilted 15°) shows a Au/Ni pyramid before it was removed from the etched Si pit. Also, we formed three-layer pyramids (Au/Ni/Au, similar to core-shell structures) that responded to a magnetic field and could have two different or orthogonal types of chemical functionality. Tri-layer pyramids with different thicknesses of Au and Ni were also fabricated (**Figure 2.4B**); remarkably, in these mesostructures, pyramidal tips exhibited radii of curvature  $r < 2$  nm (inset).

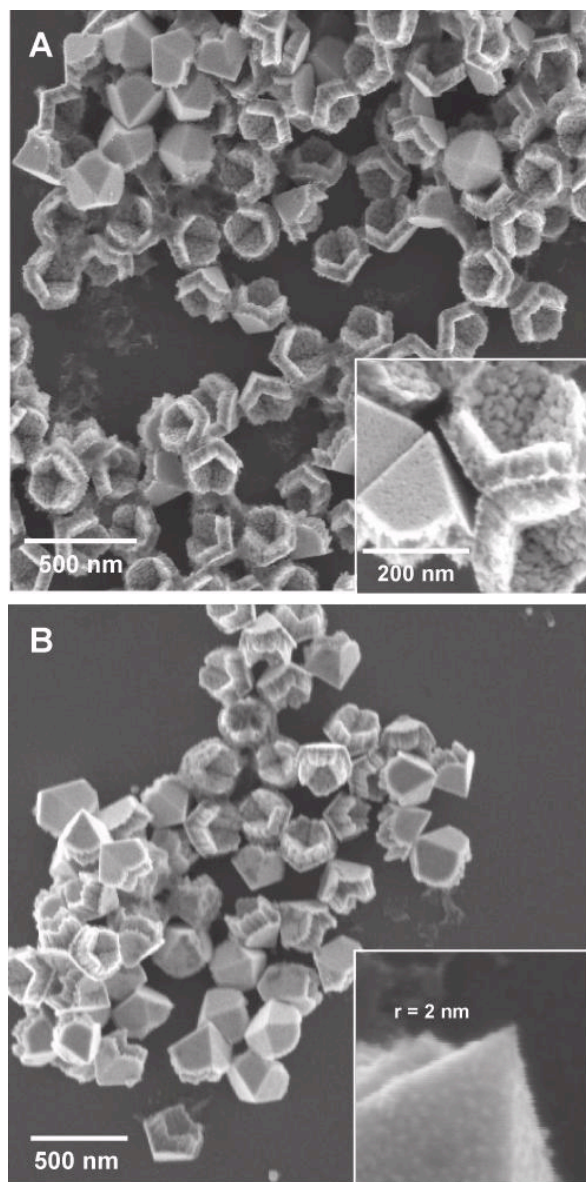


**Figure 2.4** | SEM images of pyramids composed of multiple materials. (A) Two-toned pyramids with a 50-nm Au outer shell and a 50-nm Ni inner shell. (inset) Zoom-in showing the smooth edges of the pyramid faces. (B) Three-layer pyramids of 70 nm Ni in between 40 nm layers of Au. (inset) A tip from one these structures with  $r < 2$  nm.

\

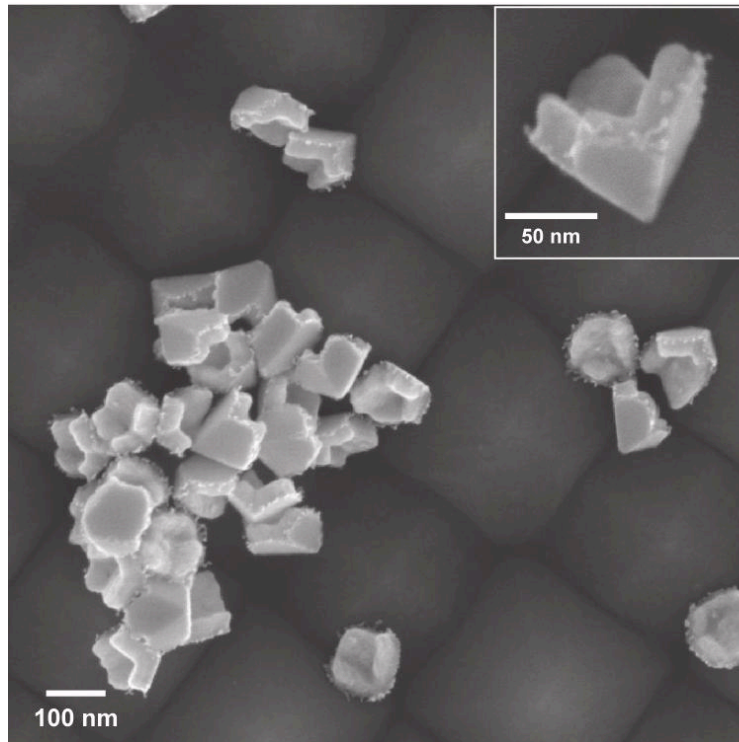


**Figure 2.5** | SEM image of a 100-nm diameter Au pyramids generated by PEEL using an SIL mask. (inset) Zoom-in showing a nanoscale pyramid.

Pyramids with sub-100 nm diameters can be fabricated with PEEL simply by using PSP masks that that can generate sub-100 nm photoresist features. **Figure 2.5** shows a SEM image of 50-nm thick, Au pyramids. We can fabricate these smaller pyramids using a variation of PSP called soft interference lithography with PEEL. This procedure is described in more detail in Chapter 4.

### 2.3 Encapsulation and Manipulation of Pyramid Arrays

**Figure 2.6** outlines a procedure for transferring Au pyramids situated within the etched pits of a Si mold into a transparent PDMS film. First, the Si substrate containing the Au pyramids (**Figure 2.7A**) was subjected to an anisotropic Si etch solution (23 g KOH, 33 mL isopropyl alcohol, in 100 mL H<sub>2</sub>O at 72°C). The pyramids acted as etch masks and protected the underlying Si; the exposed Si surface was etched quickly, leaving the Au pyramids supported on Si pedestals (**Figure 2.7B**). The Si substrate was then passivated with tridecafluoro-1,1,2,2-tetrahydrooctyl-1-trichlorosilane (Gelest, Inc.) under vacuum for 90 min. To improve adhesion between the pyramids and PDMS matrix, the Au pyramids were functionalized by immersing them in a 3 mM solution of (3-mercaptopropyl)trimethoxysilane (MPTMS, Aldrich) in ethanol for 30 s and then washing them with de-ionized water and ethanol.<sup>62</sup> The pattern was placed in a solution of 1 mM HCl for 15 min and rinsed again in de-ionized water and ethanol and then pressed against a thin (10 μm) layer of unpolymerized *h*-PDMS that was supported by a 0.5 mm-layer of Sylgard 184-PDMS. Before curing in an oven at 70°C for 30 min, it was critical to remove all air bubbles by placing the sample in a vacuum dessicator for 10 min. Afterward, the *h*-PDMS film (with the Au pyramids now partially embedded) was pulled off the substrate with tweezers, and the pyramidal tips protruded partially from the PDMS mold (**Figure 2.7C**, inset).

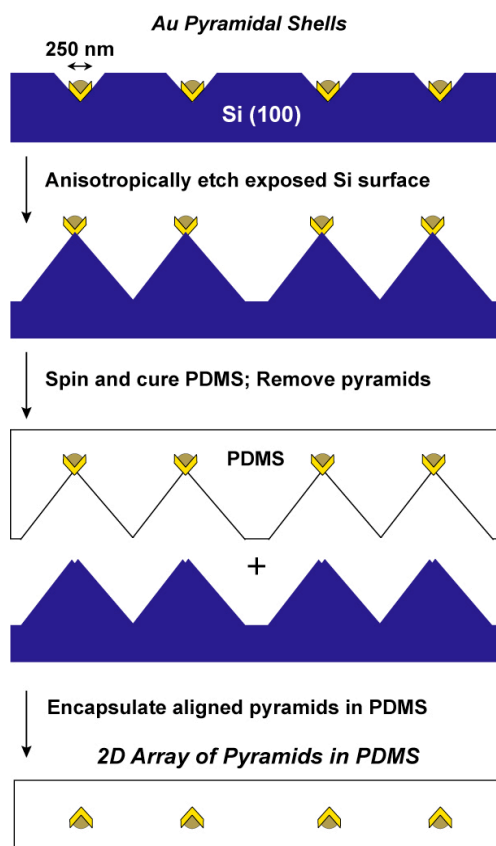


**Figure 2.6** | Scheme depicting the transfer and encapsulation of Au pyramids in a PDMS film.

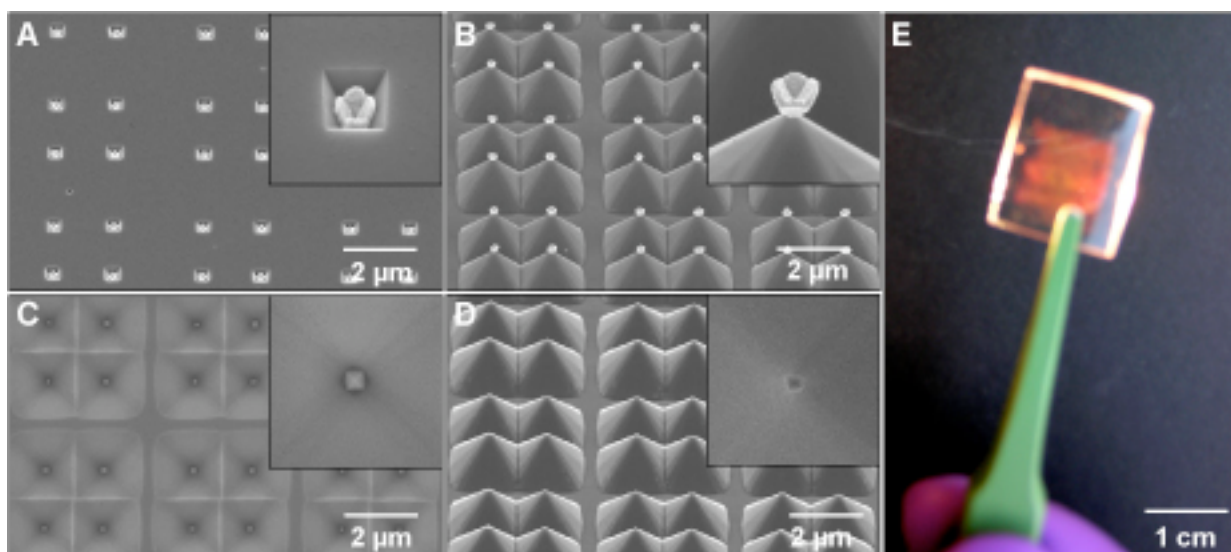


**Figure 2.7** | SEM images of the key manipulation steps. **(A)** 250-nm diameter Au pyramids situated in the centers of etched Si pits spaced by  $\sim 2 \mu\text{m}$ . **(B)** Etched Si(100) pedestals supporting the Au pyramids. **(C)** Au pyramids transferred and partially embedded within the PDMS film. **(D)** Etched Si(100) pedestals after removal of the pyramids. The dimensions of all insets are  $1 \mu\text{m} \times 1 \mu\text{m}$ . **(E)** Optical micrograph of a  $1\text{-cm}^2$  pyramid array encapsulated in a thin PDMS film.

We checked that the pyramids were transferred into PDMS by characterizing the etched Si substrate (**Figure 2.7D**). To encapsulate the Au pyramids fully, we exposed the array of pyramidal tips to mercaptosilane and then spin-coated a thin (10  $\mu\text{m}$ ) layer of *h*-PDMS on top. **Figure 2.7E** is a photograph of a large-area PDMS film encapsulating 1-cm<sup>2</sup> array of 250-nm Au pyramids.

## 2.4 Optical Characterization of Pyramid Arrays

Dark field (DF) microscopy and spectroscopy were used to characterize the optical properties of the pyramidal particles. Excitation of the arrays was achieved by passing collimated white light (Halogen-tungsten bulb) through a DF condenser (NA 0.8-0.95) equipped with a rotatable polarizer so the incident light could be polarized at certain angles with respect to the particle array. Although some of the light passing through the condenser acquired a polarization component perpendicular to the sample, we found that blocking this component with a “wedge” did not affect the spectral response. Therefore, we assumed that most of the light incident on the particle array maintained its polarization after the condenser. The scattered light from the pyramid array was collected using a 20X objective (NA 0.75) and then analyzed using a Czerny-Turner spectrometer (Triax 552/ LN<sub>2</sub>-Cooled CCD, Horiba Jobin Yvon, Inc.).

We first characterized a planar array of pyramids whose tips pointed toward the incident light and whose base planes were oriented perpendicular to the optical axis of the microscope (orientation **I**) (**Figure 2.8A**). **Figure 2.8B** depicts a DF microscopic image of an array of red spots that correspond to an array of Au pyramidal particles. Note that because 95% of the pyramids in the sample are identical as a result of our top-down lithographic procedure,<sup>16</sup> the

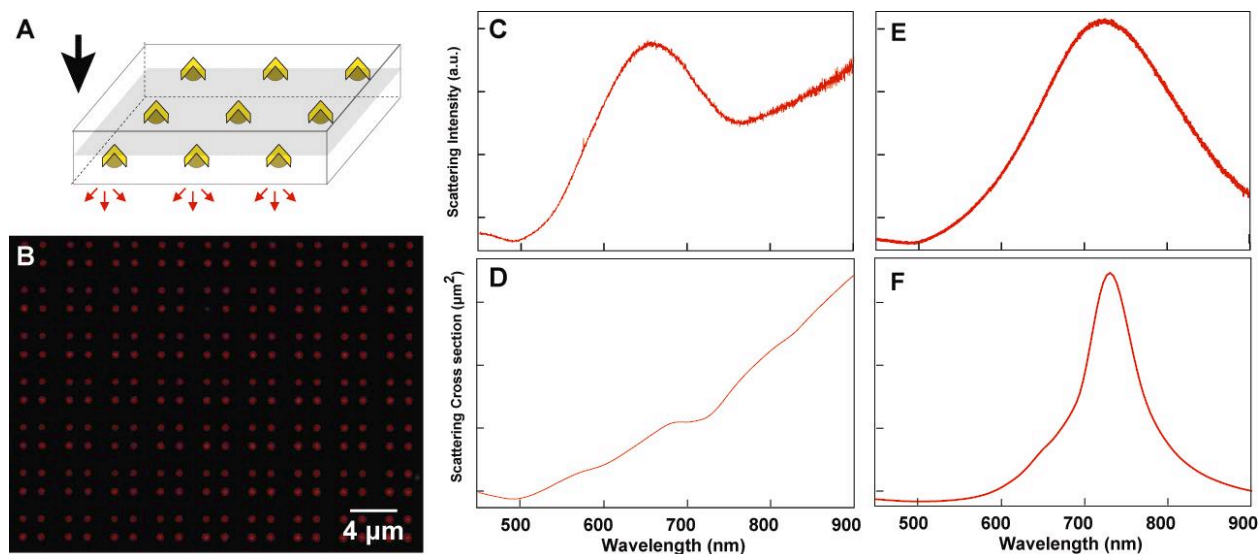


**Figure 2.8** | Optical characterization of Au pyramids in an array whose plane is *perpendicular* to the optical axis of the microscope (orientation I). (A) Illustration depicting the geometry of the particle array, the black arrow indicates the direction of the white light source while the gray area denotes the plane of the particle array. (B) DF microscope image of encapsulated Au pyramids with tips pointing directly at the white light source. (C) DF spectrum of the array of Au pyramids. (D) Calculated scattering cross section of an Au pyramidal shell structure in this orientation with the polarization parallel to the base (orientation I). (E) DF spectrum of an array of 100-nm diameter Au pyramids spaced by 400-nm (center-to-center) in orientation I. (F) Calculated scattering cross section of the pyramids in (E)

spot sizes of the scattered light are uniform, and the color (red) of every spot is the same. The scattered spectrum obtained with unpolarized white light exhibited a strong peak at red wavelengths ( $\sim 650$  nm) and another that appeared to extend into the near-infrared region (**Figure 2.8C**). The optical resonance of this array did not change, however, when the incident light was polarized because the pyramidal particles in this orientation were symmetric with respect to the optical axis. Also, the scattering spectrum from the same array with tips pointing away from the light source (the PDMS film was flipped over) was identical to the spectra in **Figure 2.8C**.

To interpret these spectra, we collaborated with Dr. Kevin Shuford and Prof. George Schatz to perform discrete dipole approximation (DDA) calculations for a pyramidal structure that models the optical properties of the Au pyramids fabricated in the experiments. The DDA calculations here are only for a single pyramid since the separation between the 250-nm Au pyramids is sufficiently large ( $\sim 2$   $\mu\text{m}$ ) that the electromagnetic interactions between them are expected to be weak. Note also that these calculations determine the Rayleigh scattering integral cross section. This cross section is not the same as the angle-resolved cross section measured in the DF spectra, but the same resonance structure should be present. **Figure 2.8D** shows that the calculated theoretical spectrum of a single Au pyramidal shell exhibits a weak peak at 680 nm superimposed on a background that increases at longer wavelengths. An analysis of the induced polarizations from the calculations indicates that the peak at 680 nm is from a quadrupole resonance-localized in the base plane of the pyramid, and that the background increases at longer wavelengths due to the tail of a dipolar excitation that peaks in the near-infrared. **Figures 2.8C** and **2.8D** show that experiment and theory are in qualitative agreement, with the main difference being the intensity of the quadrupole resonance. This difference in intensity could result from

several factors, including the difference between the calculated integral and angle-resolved cross sections noted above or the sensitivity of the calculations to subtle structural features of the pyramids. The details of the DDA calculations are described in detail in the supplemental materials in Ref<sup>94</sup>. To test the DDA calculations, we also modeled a 100-nm diameter Au pyramid and compared it with the scattering spectrum obtained for an array of 100-nm diameter Au pyramids spaced by 400-nm. The experimentally measured spectrum for these pyramids (**Figure 2.8E**) has a single resonance centered at 720 nm, in good agreement with the calculated value which had a resonance at 730-nm that corresponded to a dipolar resonance (**Figure 2.8F**).

To investigate whether the optical properties of the pyramidal shells depended on their orientation, we exploited the flexible nature of PDMS and sliced the *h*-PDMS film containing the Au pyramids into thin (500  $\mu\text{m}$ ) sections using a microtome. One of these cross-sections was placed on a glass substrate such that the planar array of pyramids as well as the pyramid base planes were parallel to the optical axis of the microscope, and the tips were pointed perpendicular to this axis (orientation **II**) (**Figure 2.9A**, inset). Since the orientation of the particles is now *not* symmetric with respect to the incident light, we could study the effects of polarization on the scattering spectra. **Figure 2.9A** shows a DF image of a thin cross-section of an array with only the bottom layer of pyramids in the depth of focus (hence the scattered light is collected only from a single layer of pyramids). Excitation by unpolarized white light (not shown) produced only broad features in the DF spectra, unlike in orientation **I**, where unpolarized as well as polarized light produced a defined quadrupole peak.

**Figure 2.9B** shows the resulting spectra for the cases where the polarization vector is parallel (upward-pointing triangle) and perpendicular (left-pointing triangle) to the base: all

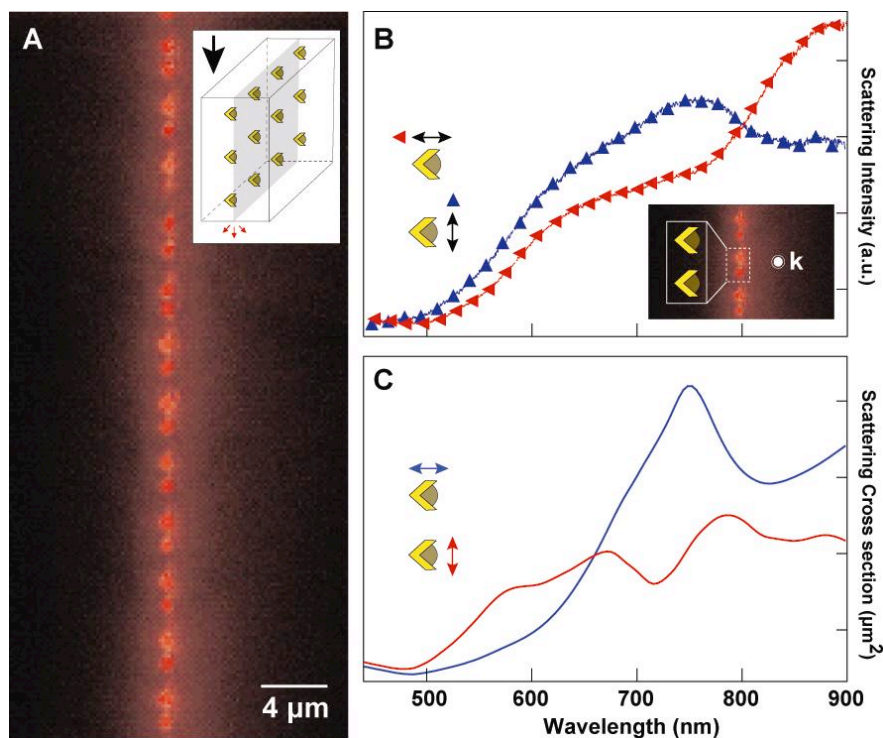


**Figure 2.9** | Optical characterization of Au pyramids in an array whose plane is now *parallel* to the optical axis of the microscope (orientation II). **(A)** DF microscope image of Au pyramids oriented on their sides and whose tips point perpendicular to the white light source. The black arrow in the inset image indicates the direction of the optical axis, and gray area denotes the plane of the particle array. **(B)** DF spectra of the Au pyramids in **(A)** illuminated with white light that is polarized parallel to the pyramid base (upward-pointing triangle) and polarized perpendicular to the pyramid base (left-pointing triangle). The inset shows how the pyramids in the array are oriented in **(A)**, and  $\mathbf{k}$  denotes the propagation wavevector, which is parallel to and down the array plane. Both spectra are plotted on the same scale. **(C)** Calculated scattering cross section of a single Au pyramidal shell in this orientation for two perpendicular polarizations.

polarization directions were defined relative to the base plane. Rotating from parallel to perpendicular polarization produced a color change in the scattered light from deep-red to light-red, respectively, corresponding to the appearance of a resonance peak around 750 nm for the parallel case, and 880 nm for the perpendicular case. When the polarization vector was  $45^\circ$ , the spectra were roughly the average of that from parallel and perpendicular polarization directions and were also similar to the spectra produced from unpolarized white light (see **Appendix I**). The calculated spectrum showed a strong resonance at 750 nm for parallel polarization (**Figure 2.9C**), in good agreement with the experiment. A polarization vector analysis indicates that this peak is the *same* quadrupole mode localized in the base plane as the one observed for orientation **I**. The calculated spectrum for the perpendicular polarization indicates the presence of several resonances with an overall envelope that is qualitatively similar to the measured result, except that the intensity of the peak at approximately 880 nm is too weak. Similar to the comparison of results for pyramids in orientation **I**, the resonance poles of the theoretical calculation match experiment well, but there are some differences in overall peak intensity.

It is interesting that the spectrum for polarization parallel to the base in **Figure 2.9B** is red-shifted from the spectrum in **Figure 2.8C**, even though they appear at first glance to be optically equivalent. In both cases the polarization vector is parallel to the base, but the wavevectors relative to the base plane are different. In **Figure 2.9B** the wavevector is parallel, but in **Figure 2.8C** the wavevector is perpendicular. This wavevector-dependence typically arises primarily when particles are large compared to the wavelength of light, because the electric field shows significant oscillations along the propagation direction. For example, when the wavevector is perpendicular to the base, the pyramids are relatively “thin,” and the excitation field is in-phase

at the base of the particle; however, when the wavevector is parallel to the base, the pyramids are relatively “thick,” and the excitation field is no longer completely in-phase. These differences can lead to excitation of different superpositions of multipoles, which has the net effect of shifting the nominal wavelength of the dominant multipole, which, for the 250-nm Au pyramids, is the quadrupole mode. In particular, the wavevector parallel to the pyramid base should result in a stronger admixture of dipolar excitation, leading to a peak that is red-shifted (**Figure 2.9B**) compared to the wavevector perpendicular to the base (**Figure 2.8C**). This present experiment and theory comparison is probably the clearest example where this effect has been observed.

## 2.5 Summary and Future Outlook

In summary, we have developed a simple procedure for fabricating free-standing, metallic pyramids with nanoscale tips. Our method is only limited by the dimensions of our *h*-PDMS mask, and hence the size of the pyramids can be shrunk and their density increased by using the fabrication procedure described in **Chapter 4**. We anticipate that the multi-layered pyramids will be most useful in investigations of biological systems because their surface functionality can be easily tailored.<sup>95</sup> Arrays of aligned, pyramidal nanoparticles exhibit orientation-dependent optical properties, which were found to be sensitive to both the propagation wavevector and polarization direction. These larger particle sizes turned out to be far more interesting than smaller, 100-nm diameter pyramids that exhibited only dipolar resonances. Most importantly, we have begun to correlate the orientation and anisotropic shape of 250-nm particles with specific multipolar plasmon resonances. Such an understanding of these unusual properties of relatively large

plasmonic particles, especially those with sharp tips and edges, can be used to enhance the capabilities of plasmon-based applications from cancer therapy to sub-wavelength optics.

**CHAPTER 3**

**MICROSCALE ARRAYS OF NANOSCALE HOLES**

### 3.1 Introduction

The enhanced transmission of light through subwavelength hole arrays has generated considerable interest in the fundamental science of surface plasmons (SPs) in part because it demonstrated that subwavelength confinement of light is feasible.<sup>21,96</sup> Nanohole arrays make possible new fundamental studies of SP interactions with periodic structures<sup>14,97,98</sup> as well as novel technologies such as spectroscopically-based chemical and biological sensors and photonic devices.<sup>96,99-101</sup> Although most research has focused on nanoscale holes with subwavelength spacings (*subwavelength nanohole arrays*), we developed a parallel nanofabrication method that can construct large-area arrays of nanoholes with microscale spacings (*microscale nanohole arrays*) that are also a product of the PEEL procedure along with nanopylamids (**Chapter 2**). The most common method to fabricate hole arrays is focused ion beam (FIB) milling,<sup>21</sup> a serial and low throughput approach that can control the diameter and spacing of the holes with reasonable precision. Free-standing suspended films have been fabricated by FIB and reactive ion etching, but the generation of multi-layered films is challenging and laborious and has been limited to only a few metals.<sup>49</sup>

Our procedure has four key advantages over current methods: (i) *Use of masters*. Masters are high-quality patterns from which many low-cost copies can be duplicated. We use inexpensive masters patterned with arrays of subwavelength features in photoresist over 1 in.<sup>2</sup> generated by phase-shifting photolithography (PSP),<sup>102,103</sup> although the procedure is readily applicable to masters prepared by other methods. (ii) *Parallelism*. Poly(dimethylsiloxane) (PDMS) is cast against a master to form an elastomeric mask, which will be used repeatedly to fabricate arrays of structures in the first step of the procedure. Our method creates all the holes in

the array simultaneously compared to drilling through a film one hole at a time. (iii) *Simplicity*. The strategy uses widely available lithographic techniques such as photolithography, wet chemical etching, and e-beam deposition. (iv) *Flexibility*. Multi-layered films of hole arrays consisting of noble metals, magnetic materials, and dielectric materials can be fabricated with exquisite control over the thickness of each layer.

Microscale arrays of nanoscale holes are important to understanding in detail the optical properties of metallic surfaces because SPPs can be imaged on their surface with near-field optical techniques<sup>27,90</sup> This chapter will reintroduce the PEEL nanofabrication method and describe in detail how to fabricate nanoholes separated by several microns. In addition, we will show near-field and far-field imaging and spectroscopy methods to demonstrate how SPPs interact with holes on an Au surface, and the extent to which they contribute to enhanced optical transmission.

### **3.2 Fabrication of Nanohole Arrays by PEEL**

Large-area films of subwavelength hole arrays were prepared using the same technique—**PEEL**—to fabricate the metallic nanopillars (**Figure 3.1**). Briefly, a nearly square array of 250-nm circular posts in positive-tone photoresist was patterned on a Si (100) wafer using PSP and a PDMS mask, followed by e-beam deposition of a thin layer of Chromium (Cr). After removal of the photoresist, the Cr-film was perforated with round holes having very smooth edges.<sup>104</sup> This Cr-layer has two functions: (i) a template for the hole patterns in the metallic films and (ii) a sacrificial layer to create free-standing films. Next, the exposed Si was

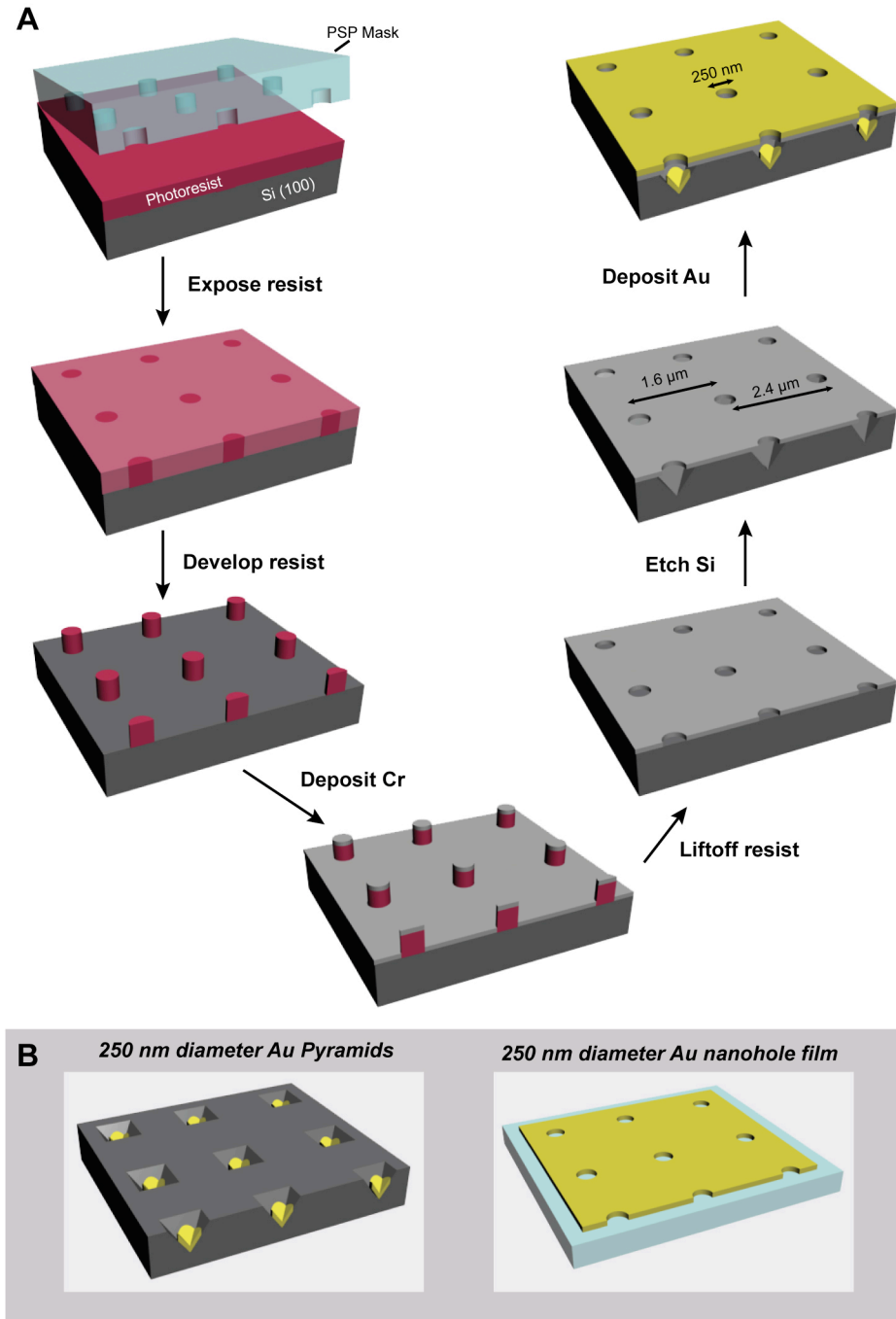


**Figure 3.1** | (A) Scheme depicting the PEEL procedure. (B) PEEL generates both nanopyramids and nanohole arrays.

anisotropically etched to form pyramidal pits beneath the Cr-holes. This void beneath the holes is a crucial step to allow relatively thick films to be created. E-beam evaporation was then used to deposit a single metal or multiple materials of desired thickness (as thick as 500 nm) onto the patterned Cr-film. By etching away the Cr-film, the perforated metallic film was detached from the Si-substrate. The free-standing films were then rinsed several times in Milli-Q water and placed on a glass cover slip to dry. **Figure 3.2A** depicts an optical micrograph of a 100-nm thick ( $t = 100$  nm) Au film perforated with 250-nm holes spaced  $1.6 \mu\text{m} \times 2.4 \mu\text{m}$ ; different, representative areas imaged by scanning electron microscopy (SEM) (**Figure 3.2B** and **3.2C**) indicate that this “single crystal” array of holes is nearly defect-free. We can also change the separation of the nanoholes by starting with photoresist posts at different spacings, including holes that are effectively isolated because their separation is larger than the plasmon propagation distance of  $\sim 10 \mu\text{m}$  at 633 nm (**Figure 3.2D**). Unlike most hole arrays fabricated by FIB, the overall topography of these large-area films is flat and very uniform.

### 3.3 Characterization of Nanohole Films with NSOM

To test the optical quality of these films, we investigated their properties using near-field scanning optical microscopy (NSOM). Optically thick Au films having 250-nm holes, sitting on a glass substrate, were analyzed using an NSOM (Aurora III) in illumination mode with Al-coated optical fiber probes. Light (excitation wavelength:  $\lambda_{\text{ex}}$ ) from a 633-nm HeNe laser or an 800-nm Ti/sapphire laser was coupled into a NSOM fiber tip that was scanned near the air/Au interface, and the transmitted light into the glass substrate was collected in the far-field with an avalanche photodiode. Although far-field light intensity is collected, the optical image,

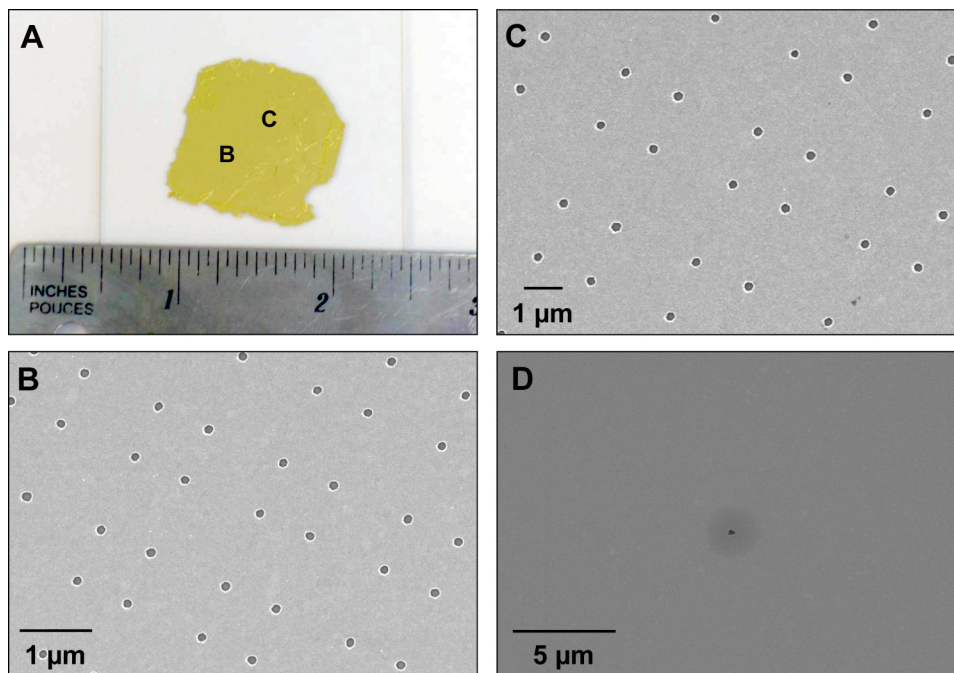


**Figure 3.2** | (A) Optical micrograph of  $\sim 1 \text{ in.}^2$  free-standing film placed on a glass substrate. (B) and (C), SEM images of representative areas of the film illustrating the uniformity of the patterning. (D). SEM image of a single nanohole whose nearest neighbor hole is  $15 \mu\text{m}$ .

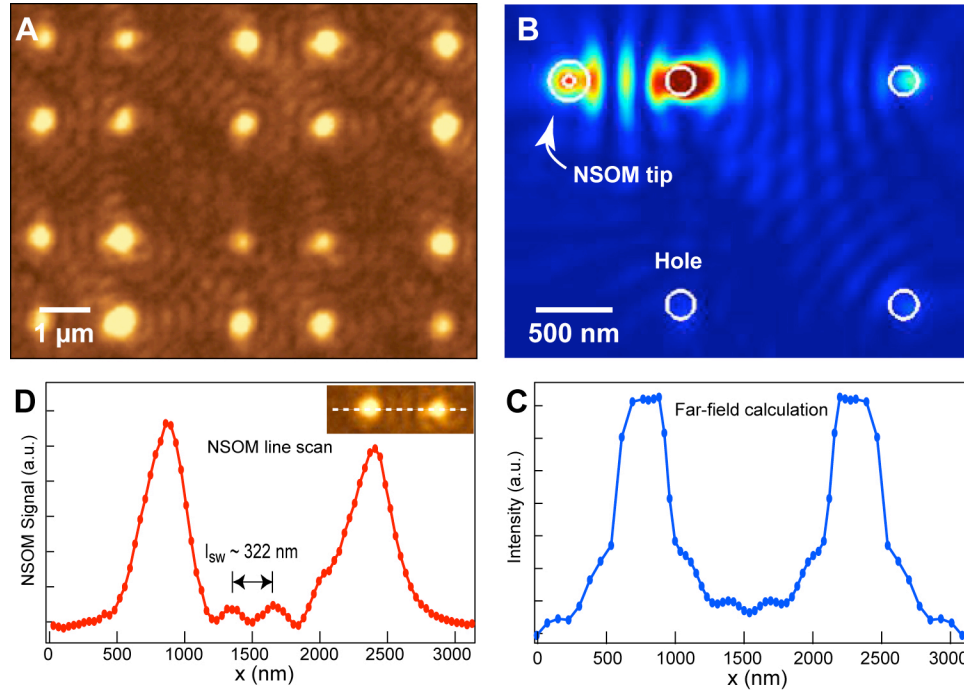


**Figure 3.3** | Near-field and far-field optical images and calculations. **(A)** NSOM optical image of holes in a 100-nm Au film on glass. The image was acquired at a 200 x 200 pixel resolution at 5 ms/pixel scan rate using an Al-coated probe (tip aperture  $\sim 70$  nm, Veeco) with an unknown, but fixed, polarization. **(B)** Calculated near-field SPP standing wave pattern at the Au/air interface for four 200-nm holes, on a  $1.6 \mu\text{m} \times 1.6 \mu\text{m}$  array, and for a 100-nm Au film supported on glass. **(C)** Calculated far-field intensity of four holes. The fringe spacing of  $\lambda_w \sim \lambda_{pp}/2$  is present but is relatively smaller in amplitude compared to the transmission through the holes. **(D)** Cross-section of two neighboring holes from **(A)**. The standing waves between the holes have a period of  $\lambda_w \sim 322$  nm.

constructed by plotting this light intensity as a function of the probe position, provides information about near-field phenomena. Under local illumination of 633-nm light, a 100-nm thick Au film (**Figure 3.3A**) exhibited enhanced transmission at the holes, which can be attributed to the localized SPs (LSPs) of the holes coupling resonantly with the incident light. Interestingly, fringes reminiscent of standing wave patterns were observed between adjacent holes.

Our results indicate that light from the NSOM tip is locally exciting surface plasmon polariton (SPP) waves on the film surfaces.<sup>105,106</sup> To verify the role of SPPs, we carried out three-dimensional Finite Difference Time Domain (FDTD) simulations in a manner similar to those in Ref<sup>107</sup>. The calculations involved a 100-nm Au film with four holes in a square array (1.6- $\mu\text{m}$  center-to-center distance) with air above and a glass substrate below. We also included a model of the NSOM tip, similar to that used in previous calculations<sup>15</sup> but in illumination mode. The incident wave was a fundamental  $\text{TM}_{11}$  mode of the NSOM fiber core that was launched from the upper part of the tip. SPP waves were generated not only on the top Au/air interface, but also on the bottom Au/glass interface because of the finite thickness of the metal film. The SPPs exhibited a  $\cos^2\Phi$  dependence in intensity along the polarization direction of the incident wave. At each NSOM tip location, the far-field signal was calculated as the surface integral of the Poynting vector in the downward direction, at a distance away from the Au/glass interface. The near-field pattern was plotted as the total electric field intensity on the Au/glass interface.

We found that fringes in the calculated near-field intensity appeared on both the top and the bottom (**Figure 3.3B**) metal surfaces because of the interference between the SPP waves generated by the tip and the SPPs reflected by the holes. These standing wave patterns were most

pronounced when the NSOM tip was located over a position of the SPP wave that corresponded to the maximum intensity. The fringes produced by the standing wave in the near-field should lead, in the far-field, to intensity maxima with a period ( $\lambda_{\text{sw}}$ ) that is approximately half of the SPP wavelength ( $\lambda_{\text{SPP}} = 603 \text{ nm}$ <sup>5</sup>) at the Au film/air interface (**Figure 3.3C**); indeed, fringes with  $\lambda_{\text{sw}} \approx 322 \text{ nm}$  (roughly  $\lambda_{\text{SPP}}/2$ ) were measured in the experiment (**Figure 3.3D**). The slight difference in the measured period of the fringes and the calculated  $\lambda_{\text{SPP}}/2$  is not surprising because the fringe pattern follows a Bessel function versus position rather than a  $\cos^2$  function.<sup>5</sup> Thus, the first few peaks have a somewhat longer peak-to-peak distance. Note that each point of the theoretical result in **Figure 3.3C** represents a separate calculation with the NSOM tip at a different position.

A more quantitative understanding of the NSOM images requires consideration of both the near-field excitation of the hole and the SPP standing waves surrounding the hole. When SPP waves encounter a hole, they are partially reflected back, which leads to standing wave formation, and partially converted into far-field light. LSP resonances at the holes are also excited, and, if the incident light is close to such a LSP resonance ( $\lambda_{\text{ex}} \approx \lambda_{\text{LSP}}$ ), far-field scattering is enhanced. This scenario describes what we observed in the 100-nm Au film on glass with 250-nm holes (**Figure 3.3A**), for which  $\lambda_{\text{LSP}} \approx 630 \text{ nm}$ , which is close to  $\lambda_{\text{ex}} = 633 \text{ nm}$ .<sup>5</sup> As the film thickness is decreased, light transmitted directly through the film will, in the far-field, dominate over that coming from SPP scattering at the holes, and the amplitude of the fringe pattern will decrease significantly or disappear, which is what we observed in 50-nm Au films (**Figure 3.4A**) using  $\lambda_{\text{ex}} = 633 \text{ nm}$ . We were able to recover faint fringes in this 50-nm film using  $\lambda_{\text{ex}} = 800 \text{ nm}$

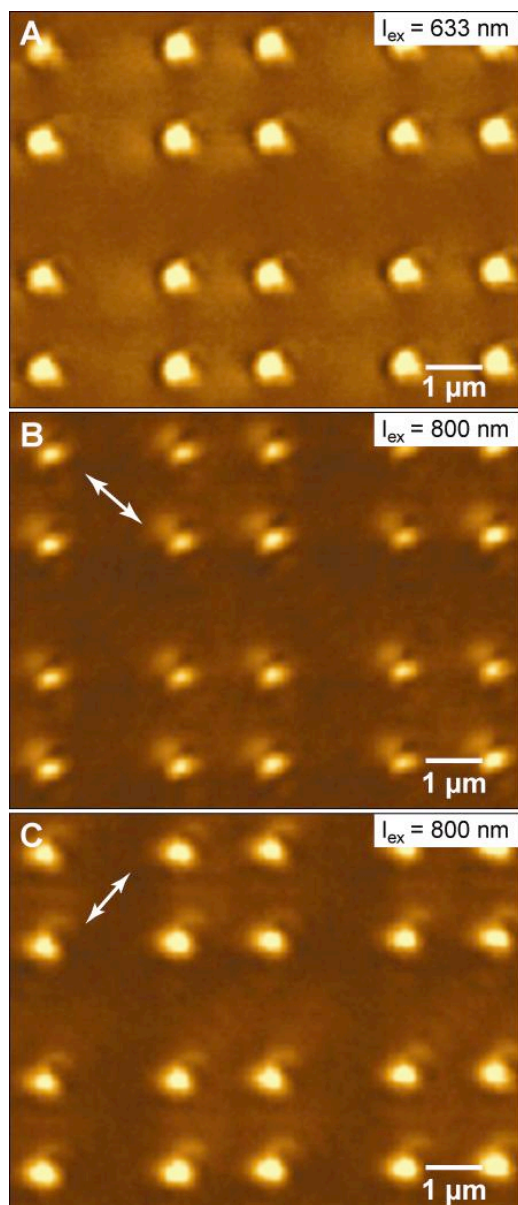


**Figure 3.4** | NSOM images of 50-nm Au films with 250-nm holes that were illuminated using (A)  $\lambda_{\text{ex}} = 633$  and (B,C)  $\lambda_{\text{ex}} = 800$  nm light. The use of longer wavelength light effectively increases the thickness of the film, so that SPP standing waves can be observed. The white arrows indicate the polarization direction of the tip. (B) Polarization is parallel to the light from the tip. (C) Polarization is perpendicular to the light from the tip.

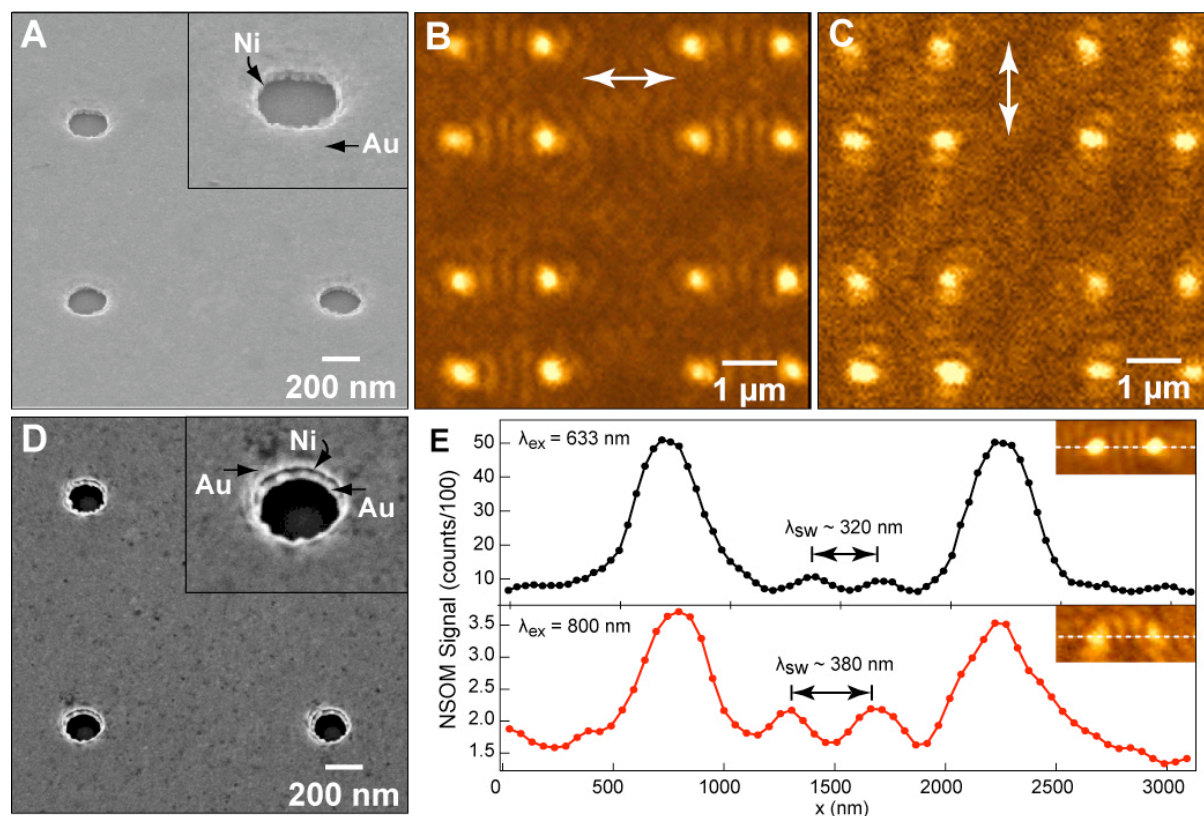


**Figure 3.5** | Structural and optical properties of bi-layered and multi-layered films. (A), SEM image of holes in a Au/Ni (50 nm/50 nm) film. The tilt angle is  $35^\circ$ . (B) and (C), NSOM images of Au/Ni film with polarization parallel and perpendicular to the light from the tip. The arrows indicate the direction of polarization, and the direction of the fringes flips as the polarization changes in orthogonal directions. (D), SEM image of 200-nm holes in a Au/Ni/Au (40/20/40) film. The tilt angle is  $25^\circ$ . (E), Cross-section of two neighboring holes in a 40/70/40 film imaged under local  $\lambda_{ex} = 633$  nm and  $\lambda_{ex} = 800$  nm light. The period  $\lambda_{sw}$  of the SPP standing wave between the holes increases as the excitation wavelength increases.

because less light can penetrate through the Au film at longer wavelengths. Moreover, we selected polarization directions that were relative to the unknown, but fixed, polarization of the tip by placing a polarizer after the film and before the detector. In this way, we observed how the orientation of the fringe patterns changed at different polarizations (**Figure 3.4B** and **3.4C**).

To provide further evidence that the formation of the fringe patterns was a result of interfering SPPs, we prepared and analyzed films of subwavelength hole arrays constructed from layers of different metals, namely, Au and Ni (**Figure 3.5A** and **3.5D**). We chose Ni because it exhibits a complex dielectric constant that is different from Au in the wavelengths of our experiments<sup>108</sup> and because it can function as an absorbing layer. A 100-nm thick bilayer film made of 50-nm Au and 50-nm Ni (Au/Ni; 50/50) was tested in the NSOM in two different configurations. In the first case, the film was placed on a glass substrate with the Ni side facing up (the Au side was against the glass). No fringe patterns were observed because no SPPs were excited in the Ni film. In the second case, the bilayer film was placed on the glass with the Au side facing up, and standing wave patterns were observed between the holes. We also investigated their dependence on polarization (**Figure 3.5B** and **3.5C**), and the directional dependence of the patterns clearly supports that the standing waves can be attributed to SPP propagation combined with scattering from the holes.

In addition, we constructed films of hole arrays consisting of three layers to show the versatility of our procedure. These multilayered films (Au/Ni/Au) consisted of a Ni core sandwiched between two layers of Au with thicknesses of 40/20/40 nm (**Figure 3.5D**) and 40/70/40 nm. Under  $\lambda_{\text{ex}} = 633$  nm light, both films exhibited standing wave patterns with a period of  $\lambda_{\text{sw}} \approx 320$  nm (**Figure 3.5E**), which is nearly identical to the pure Au film case. We

also imaged the 40/70/40 film with  $\lambda_{ex} = 800$  nm ( $\lambda_{SPP} \approx 784$  nm<sup>5</sup>) and observed fringes with an increased spacing of  $\lambda_{sw} \approx 380$  nm, which is  $\sim \lambda_{SPP}/2$  at this excitation wavelength (**Figure 3.5E**) and consistent with our theoretical model.

### 3.4 Modeling a Typical NSOM Experiment with FDTD

Our results indicate that light from the NSOM tip is locally exciting SPP waves on both sides of the film surface.<sup>106,109</sup> To verify the role of SPPs, we collaborated with Dr. Shih-Hui Chang, Prof. Stephen K. Gray, and Prof. George C. Schatz to carry out three-dimensional FDTD simulations in a manner similar to those of Refs<sup>98,106</sup>. Conventional SPPs on a metal film/dielectric interface propagate in the plane with wave vector magnitude

$$k_{SPP} = \frac{\omega}{c} \left( \frac{\epsilon_{Au} \epsilon_d}{\epsilon_{Au} + \epsilon_d} \right)^{1/2}$$

and a wavelength of

$$\lambda_{SPP} = \lambda_{ex} \left( \frac{\epsilon_{Au} + \epsilon_d}{\epsilon_{Au} \epsilon_d} \right)^{1/2}$$

where  $\lambda_{SPP}$  is the SPP wavelength,  $\lambda_{ex}$  is the free-space excitation wavelength,  $\epsilon_{Au}$  is the dielectric constant of gold, and  $\epsilon_d$  is the dielectric constant of air. In the Drude model

$$\epsilon_{Au}(\omega) = \epsilon_{\infty} - \frac{\omega_D^2}{\omega^2 + i\gamma_D \omega}$$

for Au (500-1000 nm), the best fits are  $(\epsilon_{\infty}, \omega_D, \gamma_D) = (11.4577, 9.4027$  eV,  $0.08314$  eV). Thus at  $\lambda_{ex} = 633$  nm,  $\epsilon_{Au} = -11.44 + i0.9698$  and air  $\epsilon_d = 1$ , and  $\lambda_{SPP} = 603$  nm. At  $\lambda_{ex} = 800$  nm,  $\epsilon_{Au} = -25.196 + i1.965$  and  $\epsilon_d = 1$ , and  $\lambda_{SPP} = 784$  nm. Our calculations included a model of the NSOM

tip in illumination mode. We found that fringes in the calculated near-field intensity appeared on both the top and bottom (**Figure 3.3B**) metal surfaces due to the interference between the SPP waves reflected by the holes and the SPPs from the tip. These standing wave patterns are most pronounced when the NSOM tip is located over a position of the SPP wave corresponding to maximum intensity. The fringes produced in the near-field should lead to, in the far-field, standing waves with a period ( $\lambda_{sw}$ ) approximately half of the SPP wavelength and are consistent with expected wavelengths calculated by the Drude model.

### 3.5 Measuring Enhanced Light Transmission through Metallic Nanohole Arrays

In recent years, the role of SPPs in the phenomenon of enhanced optical transmission has been the topic of much debate. SPPs were initially proposed to assist in enhanced transmission,<sup>110</sup> although subsequent theoretical and experimental work claimed different mechanisms.<sup>111-113</sup> Understanding the role of SPPs in enhanced transmission is crucial for exploiting its nature to beat diffraction in applications such as subwavelength optics and nanophotonics. We already observed SPP standing waves on using NSOM in Section 3.3. By measuring far-field transmission intensities of isolated nanoholes with arrays of nanoholes, we can determine the contribution of SPPs to the enhanced optical transmission of Au nanohole arrays. We fabricated nanoholes that were effectively isolated by patterning holes with an interhole spacing ( $a_0 = 15 \mu\text{m}$ ) much larger than the plasmon propagation distance (**Figure 3.2D**). The transmission intensity of each sample was measured using the same field of view (100X objective, NA 0.9), so the total area of the holes in each sample must be corrected for using the standard definition of transmissivity,

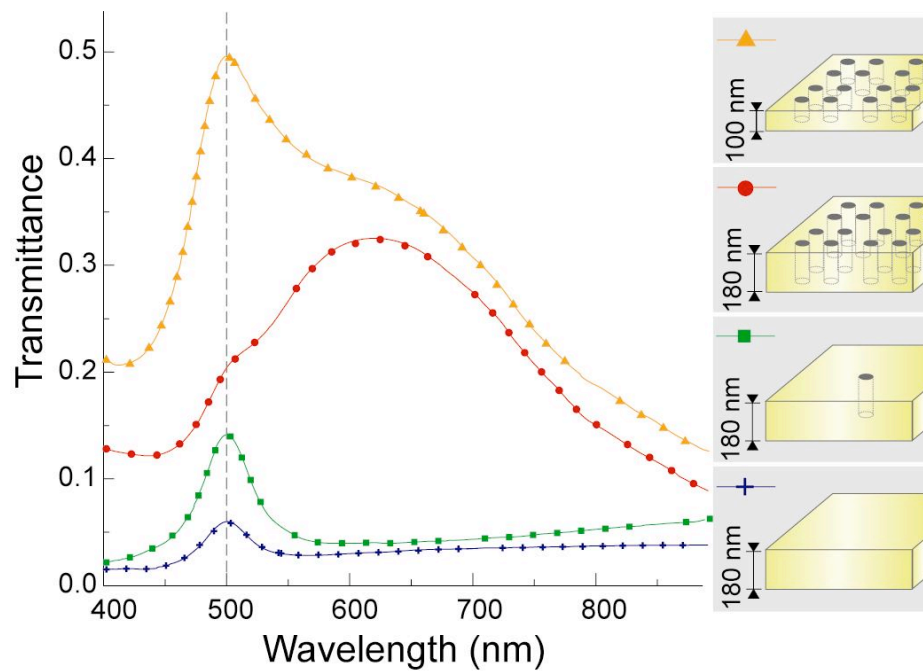


**Figure 3.6** | Transmittance of gold films, isolated holes, and nanohole arrays. Solid films (+) and single holes (■) in 180 nm thick films exhibit only an intraband transition peak at 500 nm. 250-nm hole arrays ( $a_0 \sim 2 \mu\text{m}$ ) in 180-nm films (●) and 100-nm films (▲) exhibit a SPP band centered around 615 nm.

$$T_{array} \cdot (A_{hole} + A_{film}) = T_{hole} \cdot A_{hole} + T_{solid} \cdot A_{film}$$

where  $T_{array}$  is the transmittance of the hole array films,  $T_{hole}$  is the transmittance of a single nanohole,  $T_{solid}$  is the transmittance of the solid film (without holes),  $A_{hole}$  and  $A_{film}$  are the areas of the holes and film in the hole array films.  $T_{array}$  and  $T_{solid}$  are measured by normalizing the transmission spectra of hole arrays and the solid film with respect to the profile of the excitation source. Using this definition of transmittance,  $T_{hole}$  and  $T_{array}$  were measured for *both* isolated nanoholes and nanoholes in arrays. The transmittance of all gold films showed a distinct peak around 500 nm, which represents the intraband transition and is an inherent property of the gold material.<sup>32</sup> Besides this peak, isolated 250-nm holes with  $t = 180$  nm did not exhibit any other features (**Figure 3.6**) within the wavelength range of our measurement (400-900 nm).<sup>114</sup> In contrast, nanohole arrays with the same film thickness or less than the isolated hole displayed a broad band centered around 615 nm. At the time that we took this measurement, our white light excitation source was not well-collimated, so the broad peak represents a range of SPP modes excited at multiple angles of incidence. Interestingly, the ratio of the intensity between the 500-nm peak and the 615-nm band decreased with increasing film thickness. This similar trend was also observed in part through our transmission mode NSOM studies above, where the ratio of the directly transmitted light to SPP-transmitted light decreased with increasing film thickness. This study was borne out in more detail using collection mode NSOM,<sup>115</sup> and the combination of these far-field and near-field results show that the 615-nm band is caused by the presence of SPPs launched between the nanoholes. We observed transmissivity ratios up to a factor of 8x, in

agreement with current theoretical estimates. We also measured the transmissivity of the nanoholes in silicon films and observed no significant enhancement.

### 3.6 Ultra-narrow Resonances Generated by Microscale Arrays of Nanoholes

To observe discrete SPP Bloch modes from zero-order transmission through nanohole arrays, it is crucial that the incident light is well collimated. The measurements in Section 3.4 were obtained by first passing the collimated light through a Kohler condenser and then through the sample. In this optical setup, the light was focused by this lens, acquiring a divergence of  $\theta \sim 30^\circ$ . We improved the collimation by adding an aperture before the condenser to achieve  $\theta \sim 4^\circ$  and measured the transmission spectrum of the same array of nanoholes in air and in index matching oil ( $n = 1.5$ ). **Figure 3.7** shows that both spectra exhibit a pronounced set of peaks that have Fano lineshapes indicating they are caused by SPP Bloch waves. When the incident light is normal to a square array of nanoholes of periodicity  $a_0$  in a gold film, an approximate equation for the SPP Bloch waves ( $\lambda_{SPP}$ ) is given by<sup>116</sup>

$$\lambda_{SPP} = \frac{a_0}{\sqrt{i^2 + j^2}} \sqrt{\frac{\epsilon_{Au} \epsilon_d}{\epsilon_{Au} + \epsilon_d}}$$

$i$  and  $j$  are integers corresponding to the mode order along the two lattice directions. The microscale spacing of the array produced ultra-narrow features in the transmittance (some had FWHM <15 nm) because of high order Bragg modes, where the square lattice has a spacing of  $a_0 = 4 \mu\text{m}$  (the unit cell size, since the two sets of spacings are 1.6  $\mu\text{m}$  and 2.4  $\mu\text{m}$ ). Thus, the SPP-Bragg modes are constrained by  $17 \leq (i^2 + j^2) \leq 58$  at the Au/air interface and  $40 \leq (i^2 + j^2) \leq 200$

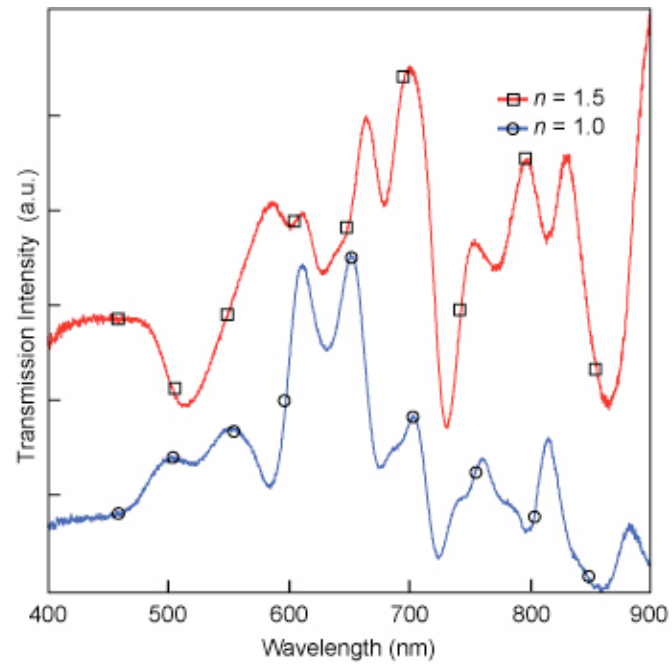


**Figure 3.7** | Transmission of nanohole Au films in air ( $n = 1.0$ ) and in oil ( $n = 1.5$ ).

at the Au/glass interface in the range defined by the Drude model in Section 3.3. High order surface plasmon Bragg modes is thus expected with microscale arrays, in contrast with the low order modes (e.g. (1,0) and (1,1)) observed in subwavelength nanohole arrays.

### 3.7 Summary and Future Outlook

In this chapter, we demonstrated a materials-general procedure to prepare arrays of nanoholes with different microscale pitches. We have used near-field and far-field spectroscopic techniques to show that plasmons exist on the surface of metallic films, and that they do enhance optical transmission—our papers<sup>115,117</sup> are part of an increasing consensus that plasmons play an important role in this phenomenon. We also showed preliminary measurements that indicate microscale arrays of nanoholes have potential use in refractive index sensing and surface their microscale spacing. The fabrication Au nanohole arrays will provide a new platform to generate optical metamaterials at visible frequencies, and metals with short wavelength plasmons (ie. aluminium) could be used for metal-enhanced fluorescence in fluorescence imaging. The future of nanophotonics is more diverse than tiny holes in metal films, but such structures are a gateway to the fundamental science of surface plasmons.

**CHAPTER 4**

**MULTISCALE PATTERNING OF PLASMONIC METAMATERIALS**

## 4.1 Introduction

The interaction of light with surface plasmons in metallic nanostructures has resulted in demonstrations of enhanced optical transmission,<sup>21</sup> collimation of light through a subwavelength aperture,<sup>22</sup> negative permeability and refraction at visible wavelengths,<sup>23,24</sup> and second-harmonic generation from magnetic metamaterials.<sup>25</sup> The structures that display these plasmonic phenomena typically consist of ordered arrays of particles or holes with sizes on the order of 100 nm. Surface plasmons can interact with each other over much longer distances, however, and so the ability to organize nanoscale particles or holes over multiple length scales could lead to new plasmonic metamaterials with novel optical properties.<sup>118</sup> In this chapter we present a high-throughput nanofabrication technique—soft interference lithography (SIL)—that combines the ability of interference lithography<sup>119</sup> to produce wafer-scale nanopatterns with the versatility of soft lithography<sup>120</sup> and use it to create such plasmonic metamaterials. Metal films perforated with quasi-infinite arrays of 100-nm holes were generated over areas greater than 10 cm<sup>2</sup>, exhibiting sharp spectral features that changed in relative amplitude and shifted to longer wavelengths when exposed to increased refractive index environments. Moreover, gold nanohole arrays patterned into microscale patches exhibited strikingly different transmission properties: for instance, patches of nanoholes displayed narrow resonances (< 14.5 nm FWHM) that resulted in high refractive index sensitivities far exceeding those reported previously.<sup>121</sup> SIL was also used to produce various infinite and finite-area arrays of nanoparticles, including optically distinct particles patterned side-by-side and those that contained both metallic and dielectric materials.

## 4.2 Fabrication and Characterization of Plasmonic Metamaterials

### 4.2.1 Preparation of SIL PDMS Photomasks:

A silicon SIL master (**Figure 4.1**) patterned with arrays of posts (diameter ( $d$ ) = 100 nm, height ( $h$ ) = 400 nm, pitch ( $a_0$ ) = 400 nm) was passivated with a fluorosilane (tridecafluoro-1,1,2,2-tetrahydrooctyl-1-trichlorosilane, Gelest, Inc.) for 24 h in a vacuum desiccator. SIL PDMS masks are composite masks, made from two layers of PDMS, where the bottom layer was a stiffer version of 184-PDMS (called  $h$ -PDMS).<sup>122</sup> The  $h$ -PDMS was spin-cast onto the SIL master and cured briefly (120 s, 70 C); a liquid pre-polymer of 184-PDMS (~3 mm) was then poured on the  $h$ -PDMS and cured for an additional 1.5 h.

### 4.2.2 Soft Interference Lithography:

Soft interference lithography uses nanoscale patterns generated by interference lithography (IL) as high quality masters for soft lithography. The Si master was molded against a transparent elastomer (polydimethylsiloxane, PDMS) to produce SIL PDMS photomasks. Hundreds of SIL PDMS masks can be replicated from a single IL-master without exhibiting observable defects. **Figure 4.2** shows the SIL procedure. A positive tone photoresist (Shipley 1805, diluted 1:3 with 1-methoxy-2-propyl acetate) was spin-cast on Si (100) wafers (5000 rpm, 40 s) and baked (90 s, 105 C). The patterned side of the SIL PDMS mask was placed in conformal contact with the photoresist and exposed to broadband UV light (Quintel Q2000) in a soft lithographic technique referred to as phase-shifting photolithography. At this point, the SIL PDMS mask was removed, and the exposed photoresist was either developed in a dilute solution of Microposit 351 (1:5 in

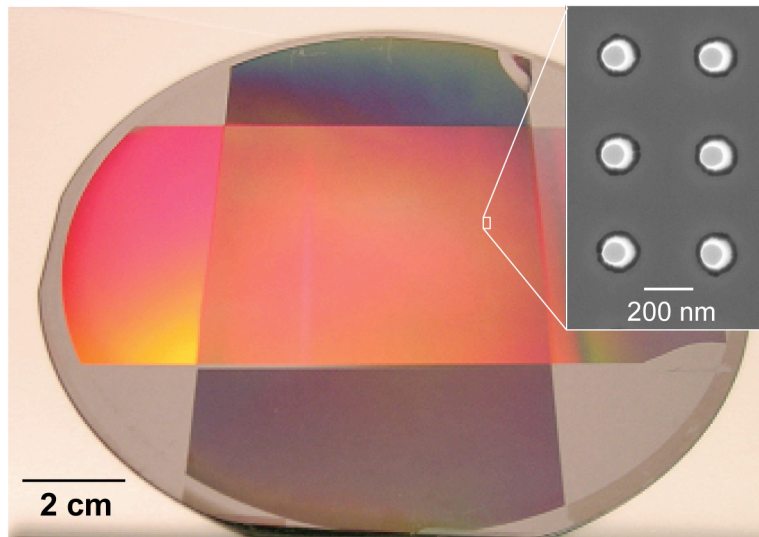


**Figure 4.1** | Optical micrograph of a 14-cm<sup>2</sup> array of 100-nm diameter Si posts ( $h$  and  $a_0 = 400$  nm) prepared by interference lithography; (inset) SEM image zoom. This pattern was used as a master for preparing SIL PDMS photomasks.

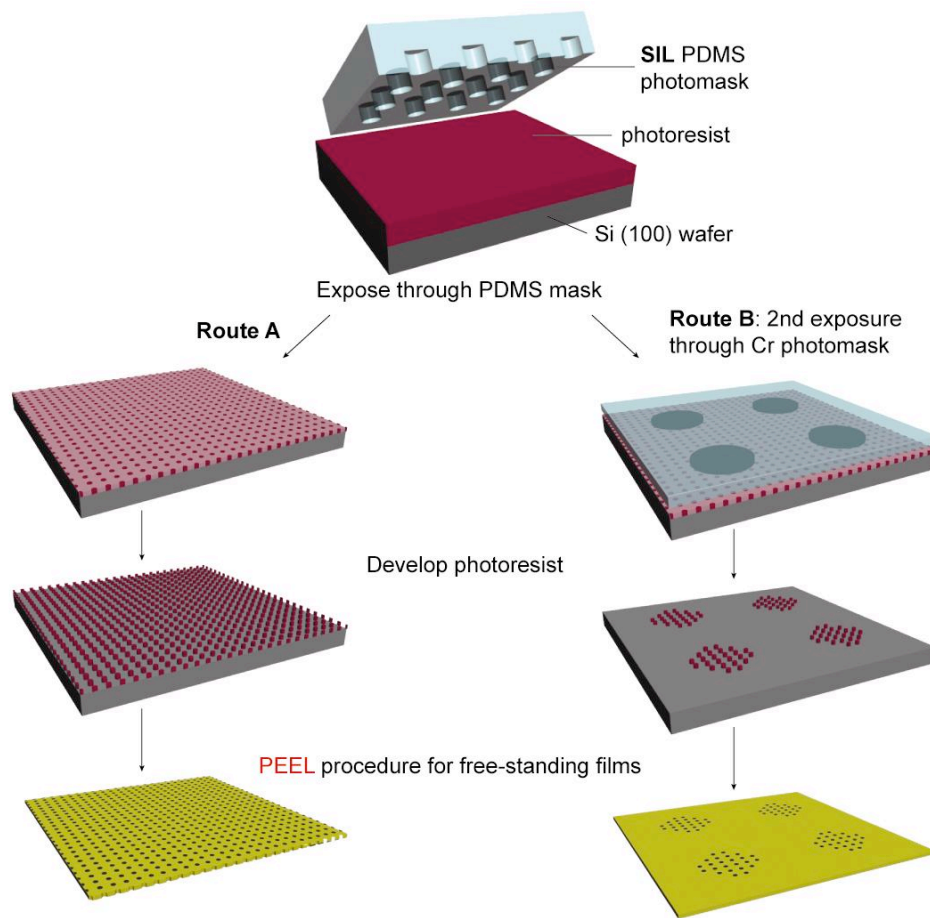


**Figure 4.2** | Scheme depicting the fabrication procedure of infinite nanohole arrays and finite-sized arrays (patches) of holes with PEEL.

water) to produce arrays of photoresist posts with the same lateral size, shape, and pitch as the master (i.e. infinite arrays) (**Route A**), or subjected to a second exposure (**Route B**) through a chromium (Cr) mask in contact photolithography and developed to achieve microscale patterns of photoresist posts (i.e. finite-sized arrays). Because the size of the patterned area of exposed photoresist posts has macroscale dimensions (ca. 2 in x 2 in), we could align the vertical and top edges of this pattern with the Cr mask pattern (ca. 1 in x 1 in) by hand. This simple method achieved relatively good rotational alignment between nanoscale arrays and microscale patterns, with a misalignment of the arrays less than  $5^\circ$ . We have also used a mask aligner to improve the misalignment to around  $1^\circ$ . Spatial alignment can be realized if the patterns on the Cr mask are commensurate with the photoresist post lattice.

#### ***4.2.3 Fabrication of Multiscale Subwavelength Nanohole Array Films by PEEL:***

Photoresist patterns were transferred into free-standing metal or dielectric films perforated with holes using a soft nanofabrication procedure called PEEL.<sup>123,124</sup> PEEL is described in detail in Chapter 2. Cr (10 nm) was e-beam deposited on the photoresist posts, and the resist was removed by sonicating the pattern in acetone to reveal round holes in the Cr film. Pyramidal pits were formed beneath the holes by etching the exposed Si with an anisotropic wet chemical etchant (23 g KOH, 33 mL isopropyl alcohol, in 100 mL H<sub>2</sub>O at 72° C). 50-nm of Au or Si was e-beam deposited on this pattern to generate a film of nanohole arrays on the Si (100) surface, and pyramidal nanostructures in the pits.<sup>124</sup> The nanohole array was released from the Si substrate by wet chemical etching (Transene Corp., Danvers, MA) of the Cr underlayer, and was then transferred to a glass coverslip under water and dried for 24 h.

#### 4.2.4 Optical Characterization of Nanohole Arrays:

Zero-order transmission spectra were collected using an inverted microscope. Collimated white light (divergence  $<4^\circ$ ) from a 100 W halogen source was passed through the nanohole film or solid film on glass collected with a 100X objective (NA 0.5) and then focused onto an imaging spectrometer (**Figure 4.3A**). The data was corrected by dividing the film spectrum by the lamp transmission profile through the glass coverslip ( $n = 1.523$ ). Bright field optical micrographs of Au (**Figure 4.3B**) and Si (**Figure 4.3C**) infinite nanohole arrays exhibited uniform intensities across the entire field of view. The index measurements were performed by placing a drop of immersion liquid ( $n = 1.293, 1.350, 1.400, 1.450, 1.5000, 1.5500, 1.6000, 1.6500, \text{ and } 1.7000 \pm 0.0005$ ; Cargille Labs) between the gold nanohole films and the objective. The spectra for the patch arrays were collected from individual nanohole patches.

### 4.3 Multiscale Arrays of Nanoscale Holes

To investigate how the properties of multi-scale patterns of nanostructures depended on materials, we fabricated arrays of nanoholes in Au and Si. High-resolution scanning electron microscopy (SEM) images of Au and Si infinite nanohole arrays reveal that the topography of both patterned materials is similar (**Figure 4.4A** and **4.4B**); the 100-nm holes are circular, and the areas surrounding the holes are smooth. **Figure 4.4C** and **4.4D** shows images of finite-sized arrays (or patches) in Au and Si generated by PEEL starting from 100-nm photoresist posts patterned into square arrays of circular regions ( $d = 2.5\mu\text{m}$ ,  $a_0 = 4.5\mu\text{m}$ ). In total,  $1 \times 10^7$  hole-array patches were fabricated simultaneously, and each 2.5- $\mu\text{m}$  patch contained around 30 nanoholes. **Figure 4.4E** highlights the differences between the zero-order transmission spectra of

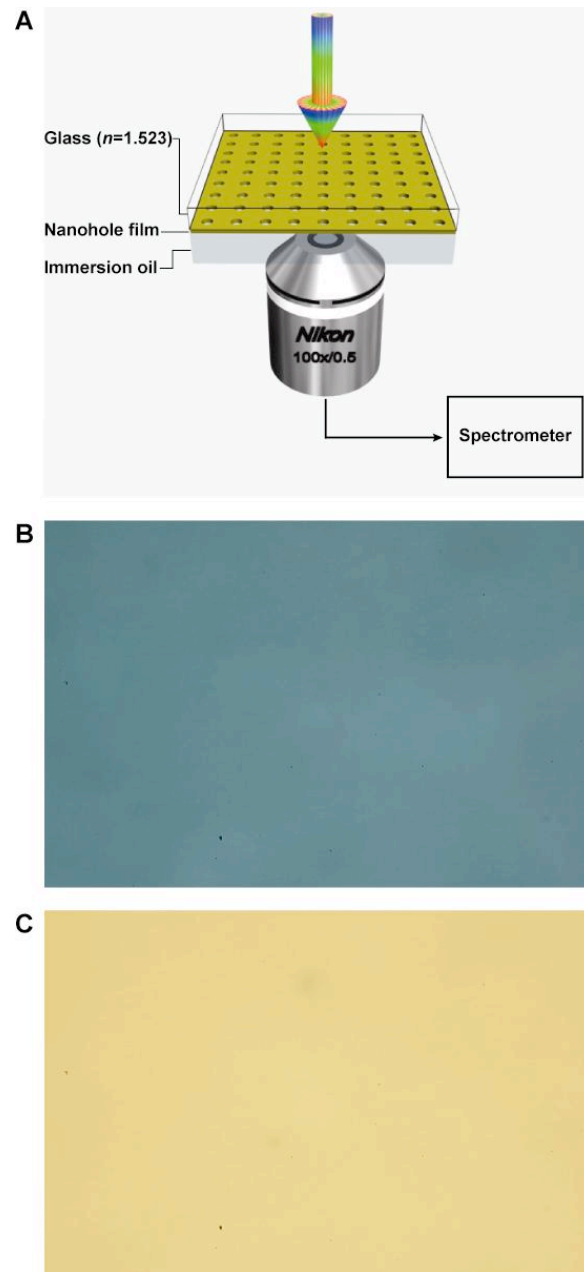


**Figure 4.3** | (A) Optical setup for characterizing the nanohole arrays. Optical micrographs of transmission seen through an (B) Au and (C) Si subwavelength nanohole film generated by SIL.

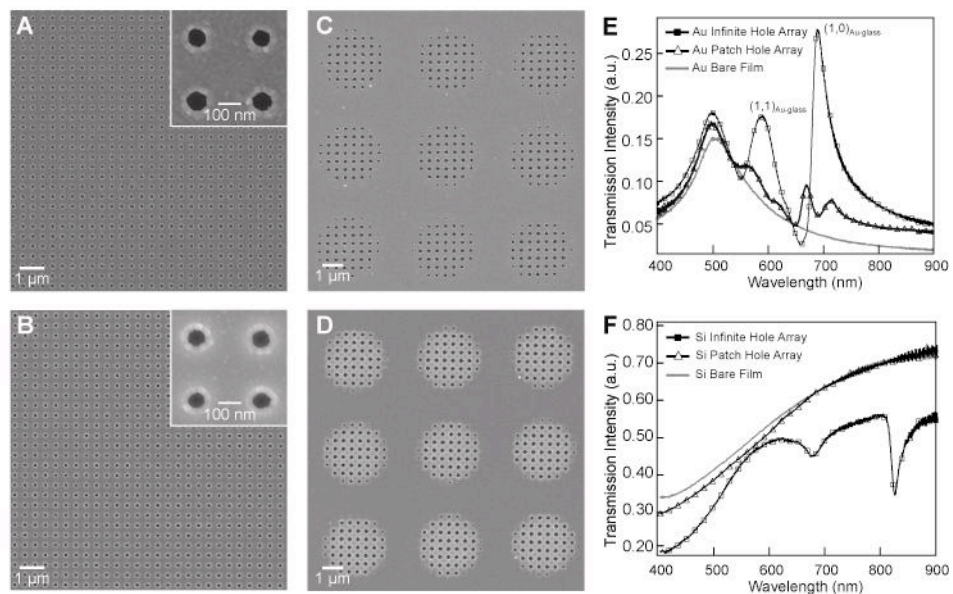
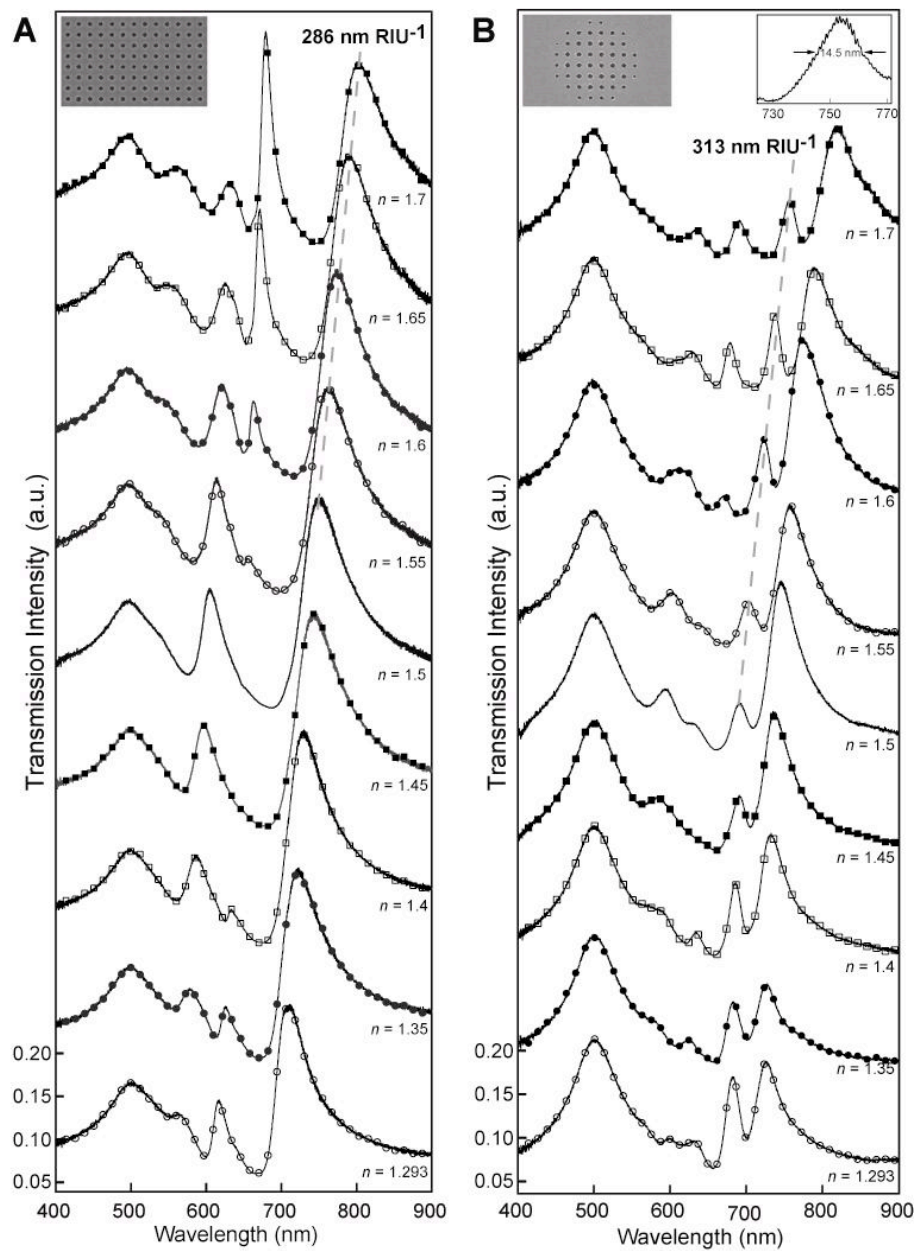


**Figure 4.4** | SEM images of (A) infinite Au nanohole array, (B) infinite Si nanohole array, (C) Au patch nanohole array and (D) Si patch nanohole array. The nanohole patches are separated by 4.5 μm. All films were 50 nm thick and supported on glass. Zero-order transmission spectra of (E) an infinite Au hole array (—■—), patch hole array (—△—), and solid film (—) and (F) an infinite Si hole array (—■—), patch hole array (—△—), and solid film (—).

infinite and finite-sized Au nanohole arrays. The intensity of the bulk plasmon resonance around  $\lambda = 500$  nm was similar for all spectra. The infinite nanohole arrays exhibited peaks characteristic of SPP-Bloch waves (BW) at the Au-glass interface of  $\lambda_{(1,0)} = 690$  nm and  $\lambda_{(1,1)} = 588$  nm,<sup>125</sup> where the subscripts (1,0) and (1,1) are integer pairs that define the particular order of the SPP-BW. The minimum in the spectra at  $\lambda = 659$  nm can be associated with a Wood's anomaly (i.e. light diffracted parallel to the surface of the film).<sup>107</sup> Compared to the calculated transmission of hole arrays based only on geometry, SIL Au nanohole arrays exhibited enhanced optical transmission factors as large as 11, providing evidence that SIL can produce hole arrays of optical quality similar to those fabricated by focused ion beam (FIB) milling.<sup>21</sup> Strikingly, the spectra of Au patches of nanoholes exhibited a marked decrease in the relative intensity of the (1,0) SPP-BW resonance, which indicated that short range coupling between holes was reduced, and the width of this peak was significantly narrower than that of the infinite array (full-width-at-half-maximum, FWHM = 18.3 vs. 34.1 nm). Moreover, a new, narrow peak emerged at  $\lambda = 660$  nm with a FWHM of 16.8 nm. In contrast, infinite Si nanohole arrays showed decreased transmission compared to solid films, and finite-sized arrays exhibited transmission slightly less than bare films (**Figure 4.4F**). Despite the different hole arrangements of individual patches, the spectra from single patches were identical because they contained on average the same number of holes.

**Figure 4.5** displays how the narrow spectral features from SIL Au nanohole arrays can be exploited for highly sensitive refractive index ( $n$ ) sensing. We controlled the dielectric

**Figure 4.5** | Refractive index sensing using Au nanohole arrays. **(A)** Zero-order transmission of infinite Au hole arrays on glass in air (refractive index,  $n = 1.0$ ) and in the presence of higher index immersion liquids ( $n = 1.000 - 1.7000$ ). The peaks shifted to longer wavelengths with higher  $n$  and split into multiple peaks at Wood's anomalies. The relative amplitude of peaks also changed as  $n$  increased. The image inset is  $3.2 \mu\text{m} \times 5.2 \mu\text{m}$ . **(B)** Zero-order transmission of patches of Au gold nanoholes on glass in air and in the presence of the same immersion liquids used in (a). Both films were 50 nm thick. Right inset depicts the narrowest resonance from the  $2.5\text{-}\mu\text{m}$  Au patches at  $n = 1.6$ . Left image inset is  $3.2 \mu\text{m} \times 5.2 \mu\text{m}$ .



environment on the top surface (previously air,  $n = 1$ ) of films of infinite and finite-sized Au nanohole arrays by using immersion oils with different  $n$ . As expected for infinite Au nanohole arrays<sup>126</sup>, the SPP-BW peaks shifted to longer wavelengths as  $n$  increased, while the bulk plasmon peak remained unchanged (**Figure 4.5A**). Also, additional SPP resonances that were previously obscured by the bulk plasmon emerged, and existing peaks red-shifted and were split by Wood's anomalies. On careful inspection, it is clear that as  $n$  increased, the relative amplitudes of peaks between 500-700 nm changed, which enables unexpected possibilities for using both the wavelengths of multiple resonances and their amplitudes to determine the refractive index of an analyte. A full theoretical analysis of the physical nature of the transmission resonances has revealed that at  $n = 1.7$ , the peak at  $\lambda = 563$  nm is a localized resonance, the peak at  $\lambda = 620$  nm is the (1,1) Au-oil resonance, the sharp peak at  $\lambda = 681$  nm arises, in part, from first order diffraction, and the peak around 800 nm can mostly be attributed to the (1,0) Au-oil resonance (J. McMahon, J. Henzie, T.W. Odom, G.C. Schatz, and S.K. Gray, accepted). Finite-sized arrays of Au nanoholes under the same dielectric environments also exhibited trends similar to the infinite arrays (**Figure 4.5B**), but noticeably, several peaks remained very narrow over the entire range of  $n$  tested; for example, the peak that shifted from  $\lambda = 690$  nm ( $n = 1.5$ ) to  $\lambda = 756$  nm ( $n = 1.7$ ) had an average FWHM of  $14.8 \pm 0.6$  nm, which is the narrowest spectral width reported to date for a surface plasmon resonance excited using an incoherent light source.

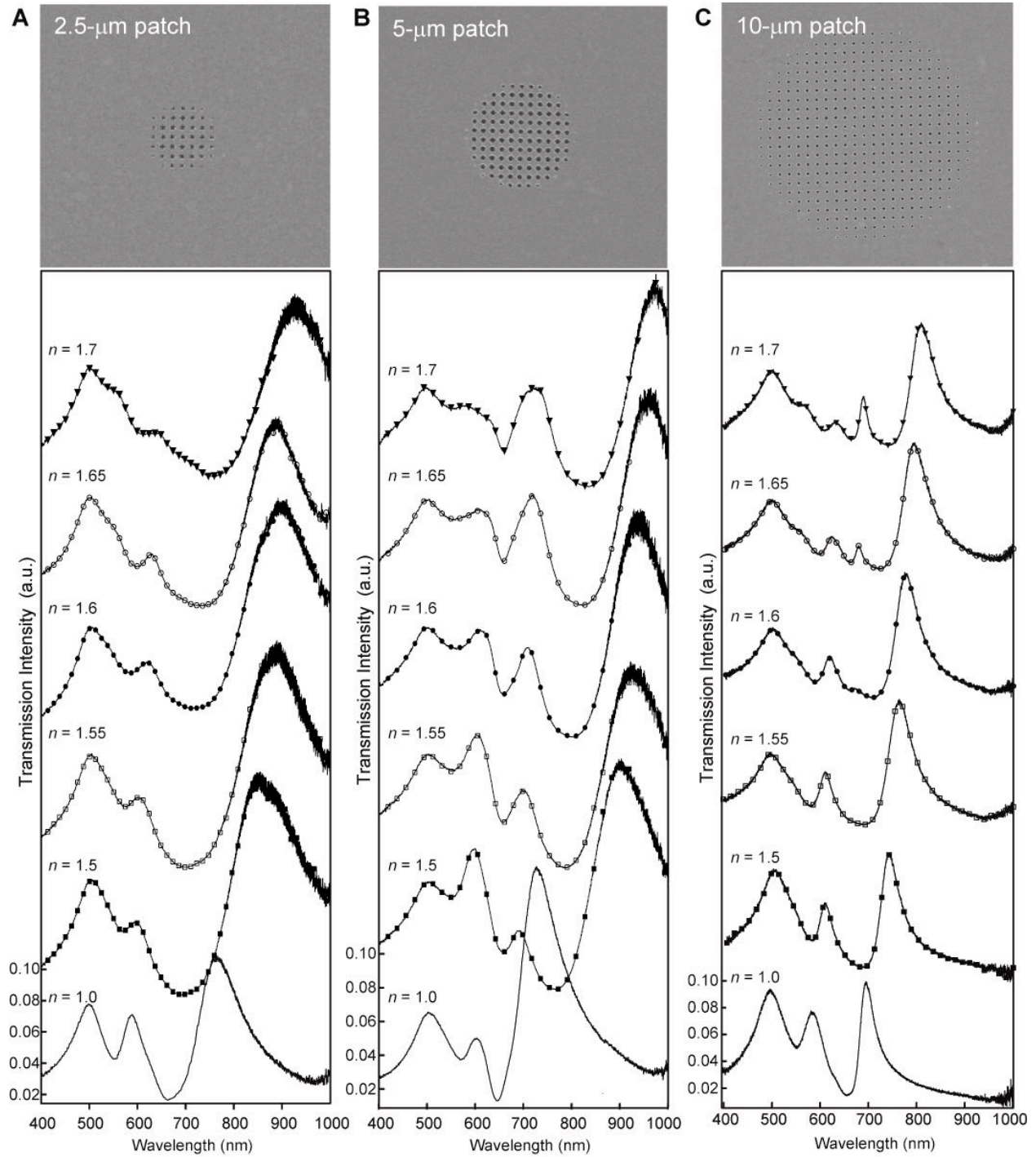
One strategy to compare the sensitivity of different metallic nanostructure systems for refractive index sensing is to calculate their figure of merit (FOM), which is the shift per

refractive index unit (RIU) divided by the width of the surface plasmon resonance (calculated in units of eV).<sup>127</sup> The SPP-BW peaks for the infinite Au nanohole arrays were relatively broad (FWHM = 70 nm) and with a shift of 286 nm RIU<sup>-1</sup> from  $n = 1.5$ - $1.7$ , and the highest FOM achieved was ca. 4.1 for the  $\lambda_{(1,0)}$  resonance (**Figure 4.5A**). The resonances for the Au patches shifted slightly more than the infinite array (313 nm RIU<sup>-1</sup>; or 0.747 eV RIU<sup>-1</sup> from  $n = 1.5$ - $1.7$ ), and considering the peak nearest to  $\lambda_{(1,0)}$  (whose FWHM = 14.5 nm at  $n = 1.7$ ; or 0.032 eV), a FOM as large as 23.3 was produced. This value far exceeds the range reported for metal nanoparticles (FOM = 0.9-5.4)<sup>121</sup> as well as that of a recently reported structure made from a metal film deposited over polystyrene spheres.<sup>128</sup> Surprisingly, the best architecture for arrays of patches for refractive index sensing consisted of patches that were close enough (e.g.,  $a_0 = 4.5$   $\mu\text{m}$ ) to interact within the plasmon propagation length ( $\sim 10$   $\mu\text{m}$ ).<sup>28</sup>

#### 4.4 Au Nanohole Patches with Large Separations

We fabricated circular Au nanohole patches with spacings larger than the SPP propagation length to examine the effects of inter-patch coupling on optical transmission. **Figure 4.6** shows isolated Au nanohole patches with 2.5- $\mu\text{m}$ , 5- $\mu\text{m}$ , and 10- $\mu\text{m}$  diameters (all separated by 15  $\mu\text{m}$  edge-to-edge). Because these patches did not exhibit ultra-narrow spectral features—compared to the geometry with 2.5- $\mu\text{m}$  patches spaced by 4.5  $\mu\text{m}$  center-to-center—we can conclude that inter-patch coupling plays a significant role in the spectral narrowing process. This new design principle is important because it shows that multiscale patterning can be used to tune the optical properties of the nanohole film without changing the primitive lattice spacing. Different

**Figure 4.6** | SEM images (top) and zero-order transmission spectra (bottom) of an isolated (A) 2.5- $\mu\text{m}$  Au patch, (B) a 5- $\mu\text{m}$  Au patch, and (C) a 10- $\mu\text{m}$  Au patch in contact with the same liquids as in Fig. 3. The spectra for a given patch have been shifted linearly (0.07-0.10 units) for clarity. All films were 50-nm thick.



geometries can be explored to understand how finite-size effects such as patch size and shape affect SPP coupling. Interestingly, as we examined the refractive index response of the isolated nanohole patches, the 10- $\mu\text{m}$  Au patches exhibited spectral signatures characteristic of the infinite array. This observation indicates that the 10- $\mu\text{m}$  patch size (with ca. 400 holes) was at or near the threshold where a finite array of holes starts to behave like an infinite array. The formula for SPP Bloch waves assumes a periodic medium. Since the 2.5- and 5- $\mu\text{m}$  diameter patches are smaller than the propagation length of the SPP, their SPP-Bloch waves are not fully formed.<sup>129</sup>

#### 4.5 Concentrating Light with Nanohole Patches

In contrast to the infinite Au nanohole arrays, light emitted from the finite-sized Au hole arrays was not uniform and appeared to be localized in the central region of the patch (**Figure 4.7**). To test if this effect was related to the surface plasmon, we collected a series of bright field images of different nanohole patches using a variety of illumination wavelengths that were controlled using 40-nm bandpass (BP) filters. The transmission images were collected above the film of patches (i.e., in the liquid ( $n = 1.5500$ ) layer) using a microscope objective (100X, NA 0.5) coupled to a CCD camera. 2.5- $\mu\text{m}$  Au patches spaced by 4.5  $\mu\text{m}$  exhibited transmission spots with narrow lateral dimensions (768 nm) whose intensity changed in coincidence with the transmission spectra of the film at  $n = 1.550$ . In contrast, 2.5- $\mu\text{m}$  Si patches spaced by 4.5  $\mu\text{m}$  exhibited dark spots at the location of the patches, providing evidence that the material properties and not just the geometric structure are important in transmission. Noticeably, 2.5- $\mu\text{m}$  Au patches spaced by 18  $\mu\text{m}$  did not exhibit the same absolute intensities as those closely spaced ( $a_0 = 4.5 \mu\text{m}$ ) because of the lack of coupling between patches. 5- $\mu\text{m}$  Au patches spaced by 20  $\mu\text{m}$

	<b>Au 2.5-<math>\mu\text{m}</math> patch</b> $a_0 = 4.5 \mu\text{m}$	<b>Si 2.5-<math>\mu\text{m}</math> patch</b> $a_0 = 4.5 \mu\text{m}$	<b>Au 2.5-<math>\mu\text{m}</math> patch</b> $a_0 = 18 \mu\text{m}$	<b>Au 5-<math>\mu\text{m}</math> patch</b> $a_0 = 20 \mu\text{m}$
SEM images				
White light				
BP = 600 nm				
BP = 650 nm				
BP = 700 nm				
BP = 750 nm				
BP = 800 nm				

**Figure 4.7** | Table summarizing the transmission of Au and Si patches of nanoholes.

exhibited transmission spots with slightly larger dimensions. The relative intensities of patches at large separations using different band-pass filters are consistent with spectra shown in **Figures 4.5 and 4.6**.

#### **4.6 Metal Enhanced Fluorescence on Nanohole Patches**

Metal surfaces can dramatically affect the excited-state lifetime and quantum yield of single molecules because surface plasmons can couple to molecular resonances.<sup>130</sup> This effect can cause either fluorescence quenching or enhancement depending on the separation between the metal and the fluorophore; fluorescence typically peaks at  $\sim 5$  nm from the surface and then is dramatically quenched as this distance decreases.<sup>131</sup> At a distance large enough to prevent quenching, the EM field near the surface is so intense that it affects these emissive properties. Thus, structures that exhibit strong LSP resonances such as nanoparticles enhance fluorescence more strongly than flat metal surfaces. For nanopatterned metal surfaces this tradeoff in intensity is balanced by the increase in homogeneity of the EM field and thus this distance dependence of fluorescent emission is not as strong. This type of enhancement would be ideal for imaging experiments where multiple fluorophores can be detected simultaneously, independent of their location away from the surface. Engineering metal surfaces with the desired emissive properties is an important problem in nanophotonics because the SP modes supported on the metal surface depend on its geometry. We used 10- $\mu\text{m}$  diameter Au nanohole patches (characterized in **Figure 4.6C**) as substrates for metal enhanced fluorescence.

**Figure 4.8A** shows an SEM image of a single nanohole patch separated by 20- $\mu\text{m}$  from its nearest neighbors. An aqueous solution of 1- $\mu\text{m}$  diameter fluorescent polystyrene beads

(Molecular Probes; excitation 633 nm, emission 680 nm) was dispersed on the surface of the nanohole patch film and allowed to dry. The transmission image of this sample in air showed the nanohole patches with beads dispersed randomly on the surface (**Figure 4.8B**). The sample illumination geometry was identical to the earlier zero-order transmission experiments (**Figure 4.3A**), with the nanohole sample positioned closest to the objective lens. The polystyrene beads located on the nanohole patches (1) were noticeably brighter than beads located on the bare Au film (2). This can be attributed to a combination of enhanced optical transmission and a lensing effect caused by the refractive index difference between the polystyrene bead ( $n \approx 1.57$ ) and air ( $n \approx 1.0$ ). We matched  $n$  by putting a drop of oil ( $n \approx 1.575$ ) on the sample—the optical properties of the polystyrene were matched with its environment and thus the beads could not be imaged in the brightfield. However, the fluorophores inside the beads could be imaged using total internal reflection fluorescence (TIRF) microscopy. The details of TIRF microscopy are described elsewhere.<sup>132</sup> In brief, laser light illuminates the sample at an incident angle greater than the critical angle for total internal reflection (TIR). The TIR geometry generates an evanescent EM field at the surface of the sample, selectively illuminating fluorophores within  $\sim 100$  nm of the surface.

**Figure 4.8C** shows the TIRF image of the sample in **Figure 4.8B**. The fluorescence intensity from the beads on the patches appears to be stronger than beads located on bare gold film, and a cross-section of their intensities shows that they differ by a factor of 1.6X. (**Figure 4.8D**). While this enhancement is smaller than typical figures found in nanoparticles ( $\sim 6$ - $8$ X), this system unoptimized and we think it can be improved. Moreover, this illumination geometry is ideal for SPP-supporting surfaces because the light can excite SPPs efficiently, which can also

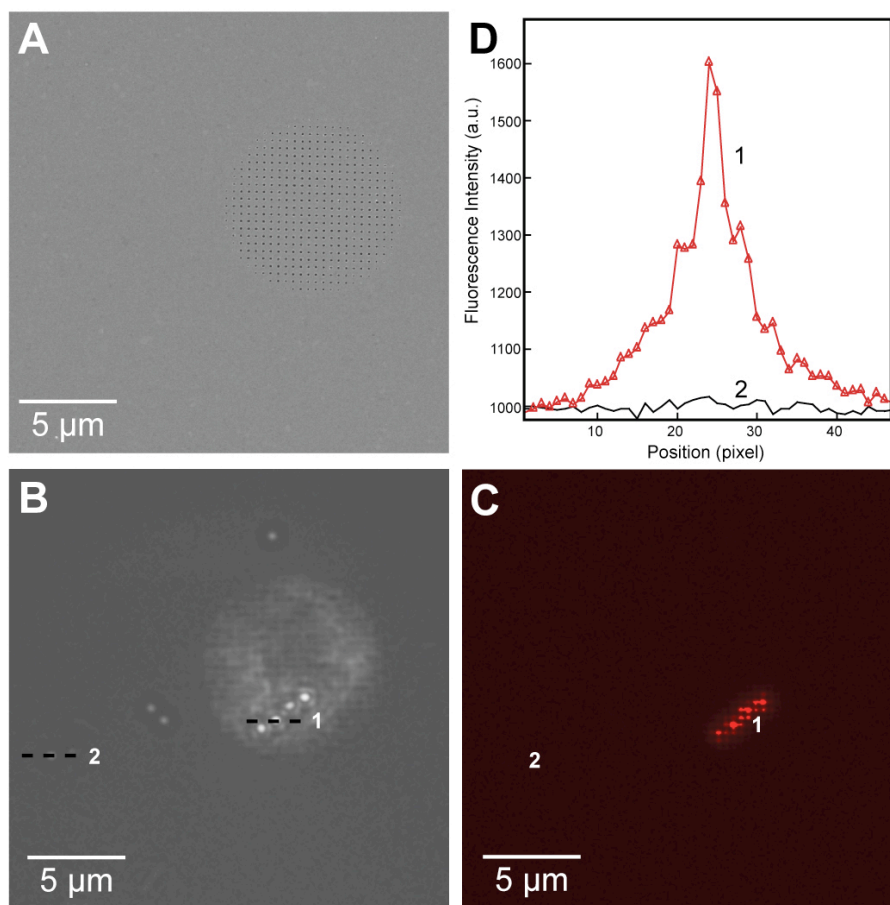


**Figure 4.8** | Metal enhanced fluorescence from 1- $\mu\text{m}$  diameter fluorescent polystyrene beads on nanohole patches. **(A)** SEM image of a 10- $\mu\text{m}$  diameter Au nanohole patch ( $a_0 = 20 \mu\text{m}$ ,  $t = 50 \text{ nm}$ ) on a glass substrate. **(B)** Transmission image of beads on nanohole patch films. The beads are located on the patch (1) and the bare Au film (2). **(C)** TIRF image of the same beads shows bright fluorescence emission from the beads located on the patch. **(D)** Cross-section of the fluorescence intensity indicates that the bead fluorescence is enhanced by a factor of 1.6.

enhance the fluorescence of adjacent fluorophores. In addition, the profile of the SPP extends farther from the surface (greater than 500 nm) than normal TIRF, and thus could excite fluorophores that are far away from the surface. The use of surfaces that can support SPPs could have use in live cell imaging, because cells are typically larger than 1 micron in height.

#### 4.7 Multiscale Patterning of Metal and Dielectric Nanoparticles

To establish further the versatility of our multiscale nanofabrication approach, we used SIL-generated Au nanohole films to fabricate large-area arrays of metallic and dielectric nanoparticles. **Figure 4.9A** illustrates how SIL Au nanohole films can function as deposition masks to create arrays of nanoparticles. Because the nanohole films produced by PEEL are inherently free-standing, they can be easily removed from any substrate by peeling them off in water. Hence, any materials-combination (metal or dielectric) can be deposited within the holes to form nearly cylindrical nanoparticles. **Figure 4.9B** depicts a portion of an array of Au nanoparticles ( $d = 100$  nm,  $h = 50$  nm) supported on a glass substrate (no adhesion layer is necessary) with the same pitch ( $a_0 = 400$  nm) as the infinite nanohole mask. Nanoparticles of other single component materials (Si, Ag, Cu) were fabricated and exhibited characteristic dark field (DF) scattering peaks from ultra-violet to visible wavelengths (**Figure 4.9C**). Scattering spectra of the nanoparticle arrays were collected using a standard transmission DF setup with the same microscope-spectrometer used in the transmission experiments. The nanoparticle arrays on glass were illuminated through a DF condenser (NA = 0.8 - 0.95) and the scattered light was collected with a 20X objective (NA = 0.75) and focused onto the spectrometer. The scattering data were corrected by dividing the lamp scattering profile of an etched glass coverslip.

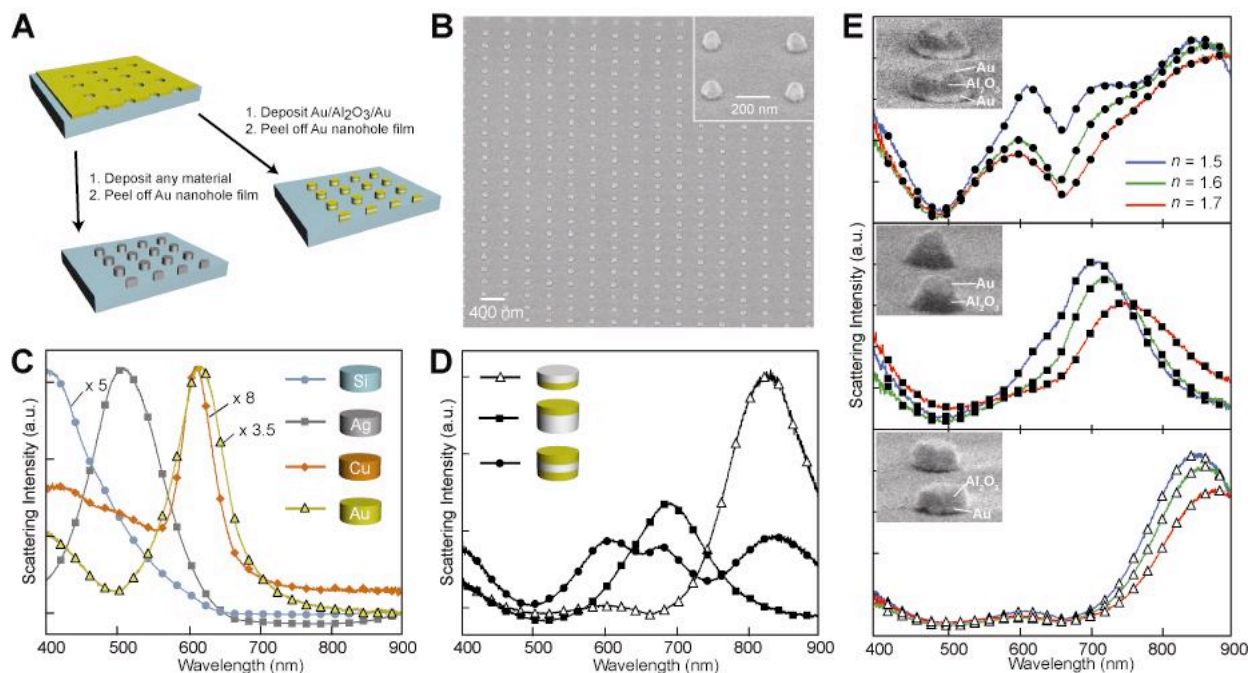


**Figure 4.9** | (A) Scheme depicting the fabrication of large-area single and multi-layered nanoparticle arrays using SIL Au nanohole films as deposition masks. (B) SEM image of a Au nanoparticle array ( $d = 100$  nm,  $h = 50$  nm); (inset) image zoom. (C) DF scattering spectra for metal (Ag, Cu, Au) and dielectric (Si) nanoparticles ( $d = 100$  nm,  $h = 50$  nm). The scattering peaks were scaled to the height of the Ag peak as indicated on the graph. (D) DF scattering spectra for multi-layered metal/dielectric nanoparticle arrays in air ( $n = 1$ ); Au/Al<sub>2</sub>O<sub>3</sub> ( $\blacktriangle$ :  $h = 25/30$  nm), Al<sub>2</sub>O<sub>3</sub>/Au ( $\blacksquare$ :  $h = 55/25$  nm), and Au/Al<sub>2</sub>O<sub>3</sub>/Au ( $\bullet$ :  $h = 25/30/25$  nm). (E) DF scattering spectra of the multi-layered nanoparticles in (D) surrounded by different refractive index liquids.

Calculations of their scattering properties were in good agreement with experiment and indicated that nanoparticles on this pitch behaved as isolated particles (S. Zhou and G.C. Schatz, unpublished).

Multi-layered nanoparticles were also fabricated by sequential deposition through SIL Au nanohole films. We selected Au and alumina ( $\text{Al}_2\text{O}_3$ ) as our building materials to investigate how metal nanoparticles coupled through a dielectric spacer. **Figure 4.9D** shows scattering spectra of three types of structures, all with Au-layers 25 nm thick. The nanoparticles with two layers, Au/ $\text{Al}_2\text{O}_3$  ( $h = 25/30$  nm) and  $\text{Al}_2\text{O}_3/\text{Au}$  ( $h = 55/25$  nm), exhibited single resonance peaks of comparable widths, although the former occurred at longer wavelengths as expected. The properties of nanoparticles in a sandwich structure (Au/ $\text{Al}_2\text{O}_3/\text{Au}$ ,  $h = 25/30/25$  nm), with upper and lower layers identical to the two-layered nanoparticles above, supported three peaks: two of the peaks were similar to those from the two-layered nanoparticles, while the third peak at shorter wavelengths ( $\lambda = 600$  nm) might be attributed to coupling between the upper and lower Au disks or a hybridized plasmon resonance. Finally, we surrounded the nanoparticle arrays with different refractive index liquids to determine their FOM values. The refractive index measurements were performed by placing a drop of immersion liquid between the array and a 100X objective (NA = 0.75). As expected, localized surface plasmon (LSP) dipolar resonances shifted to longer wavelengths as  $n$  increased, and the apparent blue-shift of the short wavelength peak from the sandwich structure (**Figure 4.9E**, bottom graph) could be due to the appearance of a multi-polar resonance.<sup>133</sup> Characteristic of dipolar LSP resonances, the broad peak widths (FWHM = 128 nm) of the multi-layered nanoparticles resulted in a FOM of ca. 1.3, which is comparable to those of other nanoparticle systems. In addition, Au films perforated with

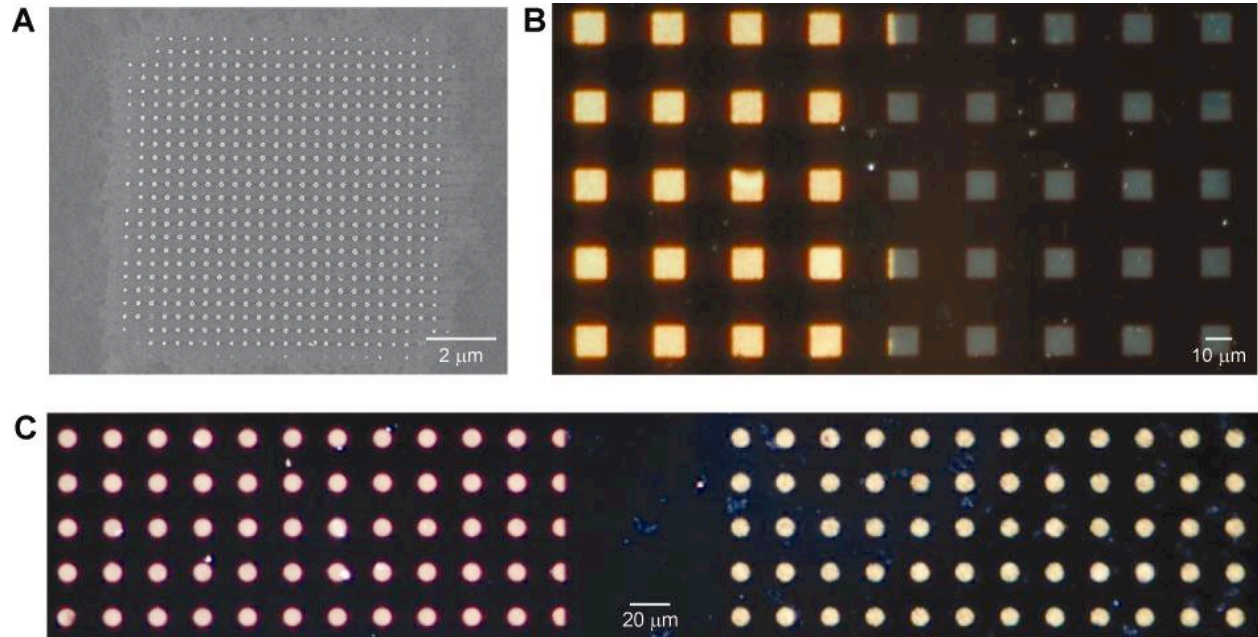


**Figure 4.10** | (A) SEM image of a 10 x 10- $\mu\text{m}$  square of Au nanoparticles ( $h = 65$  nm) fabricated using a nanohole patch film with a 25- $\mu\text{m}$  pitch. (B) DF scattering image of Cu (left) and Ag (right) nanoparticles ( $h = 15$  nm) fabricated on a different portion of the mask used in (A). (C) DF image of Au (left) and Ag (right) nanoparticles ( $h = 65$  nm) fabricated using a 10- $\mu\text{m}$  circular nanohole patch film.

nanohole patches were used as masks for multi-scale patterning of different nanoparticles on the same substrate. **Figure 4.10A** is an SEM image of an Au nanoparticle array generated from a single 10- $\mu\text{m}$  square hole patch within a patch array ( $a_0 = 25 \mu\text{m}$ ). A different portion of this patch array-mask was also used to fabricate 100  $\mu\text{m}^2$ -areas of thin ( $h = 15 \text{ nm}$ ) Cu and Ag nanoparticles side-by-side; DF images indicated that some patches at the interface contained both materials (**Figure 4.10B**). Finally, **Figure 4.10C** shows that thicker ( $h = 65 \text{ nm}$ ) Au and Ag particles can be patterned into arrays of 10- $\mu\text{m}$  circular regions.

#### 4.8 Summary and Future Outlook

In summary, we have demonstrated how a new, multiscale nanofabrication technique can manufacture plasmonic metamaterials with unexpected optical properties. The scientific opportunities opened by such structures range from ultra-small light sources to highly sensitive refractive-index sensors to fluorescence enhanced substrates. The nanohole patches are particularly interesting because they appear to be focusing light in the far-field; we currently do not know if this can be attributed to the plasmon or to the geometry of the nanohole patches. Others have observed diffraction-based focusing from millimeter-scale annular rings that generate diffraction-less Bessel beams in the far field.<sup>134,135</sup> The profile of these beams appear to be similar to the beams emerging from the nanohole patches. Further study on far-field emission of the nanohole patches needs to be conducted. Our fabrication technique offers an accessible approach for multiscale nano-manufacturing over tens of square centimetres, and SIL could also be used to produce metal-dielectric nanostructures that exhibit negative refractive indices at

optical wavelengths or plasmonic nanostructures that can detect and identify analytes with exquisite sensitivity.

**CHAPTER 5**  
**ADDRESSABLE, LARGE-AREA NANOSCALE ORGANIC LIGHT-EMITTING**  
**DIODES**

## 5.1 Introduction

Advances in the fabrication and processing of macroscale organic light-emitting diodes (OLEDs) for commercial products such as full-color displays has generated new interest in making OLEDs at the nanoscale.<sup>136,137</sup> Making OLEDs smaller is advantageous because it permits higher device densities per unit area, allowing higher resolution displays that are more defect-tolerant and viewable at close range.<sup>138</sup> Furthermore, nano-OLEDs could be used as subwavelength light sources for high-resolution imaging techniques as well as nanoscale optical lithography.<sup>139</sup>

Although serial approaches have been employed for fabricating nano-OLEDs, the primary disadvantages of these methods include the small write sizes ( $\leq 0.2 \text{ mm}^2$ ) and the low densities ( $1 \times 10^4 \text{ pixels/mm}^2$ ) of the arrays.<sup>140,141</sup> We have developed a method to fabricate nano-OLED arrays over large areas ( $\sim \text{cm}^2$ ) and with pixel densities much larger than those reported using serial techniques such as electron-beam lithography (EBL). In contrast to those methods, we employed an inexpensive parallel technique using patterned polydimethylsiloxane (PDMS) as a photolithography mask to generate arrays of bas-relief holes in photoresist on a conductive substrate. These structures were used to assemble electroluminescent dye to produce nano-OLEDs with 250-nm diameters and defect densities that only depended on imperfections in the PDMS mask. We also demonstrated how these nano-OLEDs are addressable in one dimension (1D).

Progress toward nano-OLEDs has largely been achieved by defining the area of the electrical contacts. Nanosphere lithography has been used to fabricate sub-100 nm pixels by reducing the active area of the indium tin oxide (ITO) anode.<sup>142</sup> Nanoscale holes (60-200 nm in

diameter) within insulating materials such as  $\text{SiO}_2$ <sup>140</sup> or  $\text{Si}_3\text{N}_4$ <sup>141</sup> have been used to define nano-OLEDs based on polyfluorene<sup>140</sup> and poly-[2-methoxy-5-(2'-ethylhexyloxy)-1,4-phenylene vinylene].<sup>141</sup> Although EBL could confine the effective size of the anode, the nano-OLEDs could not be individually addressed because they were all patterned on the same electrical back plane.

OLEDs based on the electroluminescent ruthenium bipyridyl complex ( $\text{Ru}(\text{bpy})_3$ ) have received much attention because this dye molecule is an efficient and bright emitter.<sup>143-146</sup> Addressable 1D arrays of  $\text{Ru}(\text{bpy})_3(\text{ClO}_4)_2$ -based OLEDs have been fabricated on glass substrates patterned with five 0.9- $\mu\text{m}$  lines or “finger electrodes” of ITO on a 1.1  $\mu\text{m}$  pitch.<sup>147,148</sup> Although individual lines were contacted, one drawback was that the wet etching step used in this fabrication procedure generated small defects in the ITO lines. The ability to pattern addressable, nano-OLEDs over  $\text{cm}^2$ -areas is critical for producing practical devices and for testing the possibilities of confining light emission to nanoscale dimensions.

## 5.2 Fabrication of Nano-OLEDs

### 5.2.1 Synthesis of $\text{Ru}(\text{bpy})_3(\text{BF}_4)_2$

$\text{Ru}(\text{bpy})_3(\text{BF}_4)_2$ : Tris(2,2'-bipyridyl) ruthenium (II) chloride (0.201 g, Aldrich) was dissolved in Millipore water (6 mL) and heated to 95° C. Sodium tetrafluoroborate (0.229 g, Aldrich) was dissolved in Millipore water (1 mL) in a separate beaker and heated to 95° C. The aqueous sodium tetrafluoroborate solution was then added dropwise into the tris(2,2'-bipyridyl) ruthenium (II) chloride solution and stirred for 15 min at 95° C. As the reaction mixture was slowly cooled to room temperature over a one-hour period, tris(2,2'-bipyridyl) ruthenium (II) tetrafluoroborate [ $\text{Ru}(\text{bpy})_3(\text{BF}_4)_2$ ] crystals formed. After the reaction mixture was cooled for

another 20 min over an ice bath, the crystals were isolated and collected by vacuum filtration. Crystals were washed with ice-cold Millipore water (3 x 1 mL) and stored in a vacuum desiccator until they were used in the devices. 10 mg/mL stock solutions of Ru(bpy)<sub>3</sub>(BF<sub>4</sub>)<sub>2</sub> were prepared in acetonitrile prior to device patterning.

### 5.2.2 Fabrication of nanohole arrays in SU-8

Phase-shifting photolithography (PSP) was used to generate holes in negative photoresist. SU-8 was chosen as the resist layer because it is not conductive and passivates the conductive ITO electrode everywhere except the nanohole. SU-8 photoresist was spin-cast onto ITO-coated glass slides and exposed through an *h*-PDMS PSP photomask patterned with a 2- $\mu$ m array of 250-nm circular recessed posts. The resist was developed in PGMEA, and the samples were cleaned by sonication in water. A typical optical micrograph of the sample had 250-nm circular openings in SU-8 with few holes in the array missing (**Figure 5.2A**). Upon examining the composite (*h*-PDMS) mask used in the PSP step, we found that the missing holes in SU-8 were a consequence of defects in the PDMS mask. We carried out statistics on ten areas of the patterned SU-8 layer (each covering 7200  $\mu\text{m}^2$ ) and found that  $1.8 \pm 0.2\%$  of the holes were missing. Using PSP to define the hole sizes in SU-8 allowed us to pattern arrays of holes simultaneously and with much higher densities ( $2.6 \times 10^5$  pixels/ $\text{mm}^2$ ) than holes that EBL has produced in SiO<sub>2</sub> ( $1 \times 10^4$  pixels/ $\text{mm}^2$ ).<sup>140</sup>

### 5.2.3 Fabrication of ITO line arrays

Positive photoresist (Shipley 1805) was spin cast onto ITO coated glass slides. The photoresist was exposed through a *h*-PDMS PSP mask patterned with 350-nm wide line-recesses spaced by 15  $\mu\text{m}$ . After development in 351 Microposit, 350-nm lines of photoresist spaced by 15  $\mu\text{m}$  remained on the ITO. The photoresist acted as an etch mask in a  $\text{CH}_4/\text{H}_2$  plasma. The ITO was etched at a rate of 10 nm/min using flow rates of 5/25 sccm  $\text{CH}_4/\text{H}_2$  at a pressure of 11 mTorr and an RF power of 100 W. The photoresist was then lifted off by sonicating the samples in acetone and treating the residual organics with oxygen plasma to reveal lines of ITO that were 350-nm wide. The ITO was then cleaned by sonicating the samples for 5 minutes in Millipore water, followed by acetone, dichloromethane, and absolute ethanol.

### 5.2.4 Device Fabrication

**Figure 5.1** shows the complete procedure for the fabrication of  $\text{Ru}(\text{bpy})_3(\text{BF}_4)_2$ -based nano-OLEDs. Phase-shifting photolithography was used to fabricate large-area ( $>1 \text{ in.}^2$ ) nanohole arrays of 250-nm diameter holes in SU-8 on ITO/glass to define the active area of the OLEDs (**Figure 5.1A**).<sup>122,149,150</sup> When the  $\text{Ru}(\text{bpy})_3(\text{BF}_4)_2$  was spincast on this pattern, the holes were filled and electricity can pass through these nanoscale regions to generate highly confined electroluminescence. Addressable nano-OLEDs were fabricated following a similar procedure, except the ITO layer was first patterned into an array 1D electrodes (**Figure 5.1B**). Devices were assembled by spin-coating a solution of  $\text{Ru}(\text{bpy})_3(\text{BF}_4)_2$  onto the SU-8 nanohole arrays followed by a quick baking step and then placing an In/Ga eutectic cathode onto the  $\text{Ru}(\text{bpy})_3(\text{BF}_4)_2$  layer.

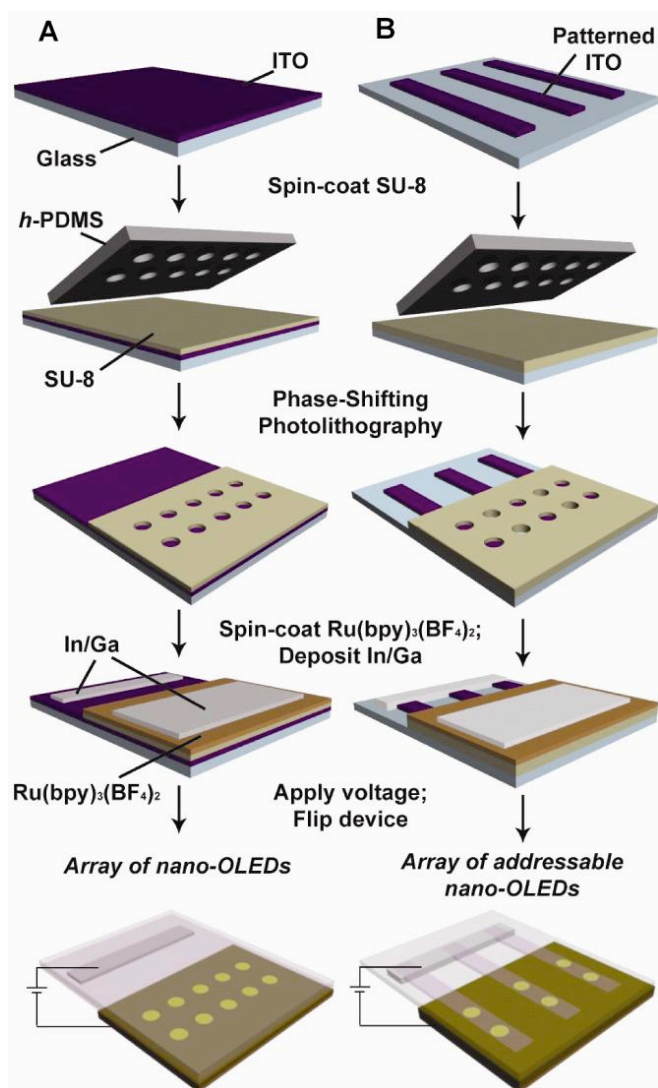


**Figure 5.1** | (A) Scheme for defining the anode area for fabricating nano-OLEDs. (B) Scheme for patterning addressable nano-OLEDs.

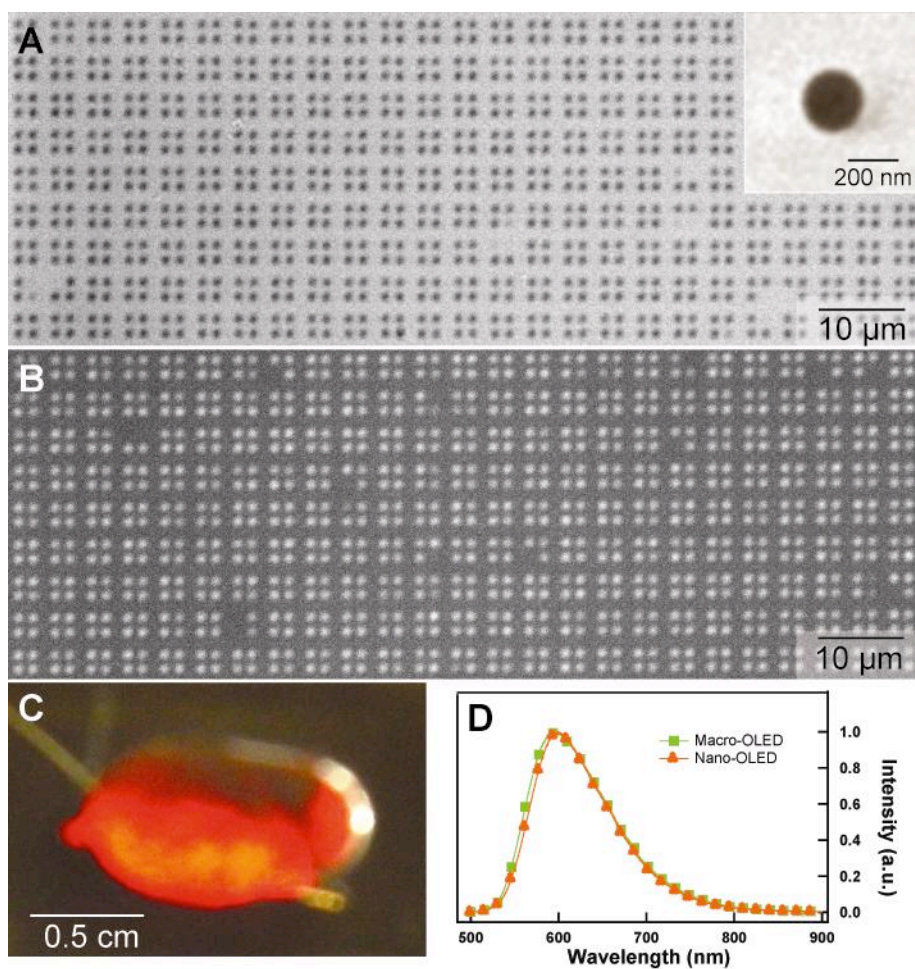


**Figure 5.2** | (A) Optical micrograph of 250-nm circular openings in SU-8 (inset: AFM image of a single nanohole). (B) EL image of nano-OLEDs operated at 3.9 V. (C) Photograph of large-area emission from the nano-OLED array. (D) EL spectra of nano-OLEDs (▲, orange line) and macroscale OLEDs (■, green line).

### 5.3 Characterization of Nano-OLEDs

We took a bright-field image of the nanopatterned SU-8 on ITO using an inverted optical microscope (**Figure 5.2A**). Later, we added the InGa electrode and applied a voltage to image the electroluminescence (EL) from individual nano-OLEDs in the same large-area array (**Figure 5.2B**). Only 2% of the nano-pixels viewed in a  $7200 \mu\text{m}^2$  area did not exhibit EL. Importantly, the density of defects matched the density of missing holes in the SU-8 pattern; thus, the number of defects in our arrays can be reduced to less than 2% simply by using a higher quality *h*-PDMS nanomask. Moreover, this defect density is significantly lower than the failure rate reported for nano-OLEDs prepared by EBL (10%),<sup>140</sup> where the primary cause of defects was incomplete etching of some of the holes. **Figure 5.2C** shows that EL can be observed over areas as large as  $0.7 \text{ cm}^2$ , which contain  $\sim 2 \times 10^7$  nano-OLEDs. The EL spectrum recorded from a  $0.07\text{-mm}^2$  area containing nearly  $2 \times 10^4$  nano-OLEDs exhibited an emission peak at 600 nm with a full-width-at-half-maximum (FWHM) of 150 nm (**Figure 5.2D**); this nano-OLED emission spectrum was similar to that from a single macroscale OLED ( $\sim 5 \text{ mm}^2$ ), as expected. Devices that were operated at 3.9 V in air showed bright EL that could be observed under ambient conditions for about two hours, a comparable lifetime to other reports of  $\text{Ru}(\text{bpy})_3$  -devices patterned in air.<sup>146,148</sup>

To address a single row of nano-OLEDs, we patterned SU-8 hole arrays on 350-nm wide lines of ITO separated by  $15 \mu\text{m}$ . Although the ITO lines could have been easily fabricated on the same pitch as the SU-8 holes, we prepared ITO lines with relatively large spacings so that each electrode could be individually addressed by hand using a sharpened aluminum wire. **Figure 5.3A** shows that a slight mismatch exists between the arrays of SU-8 holes and the ITO

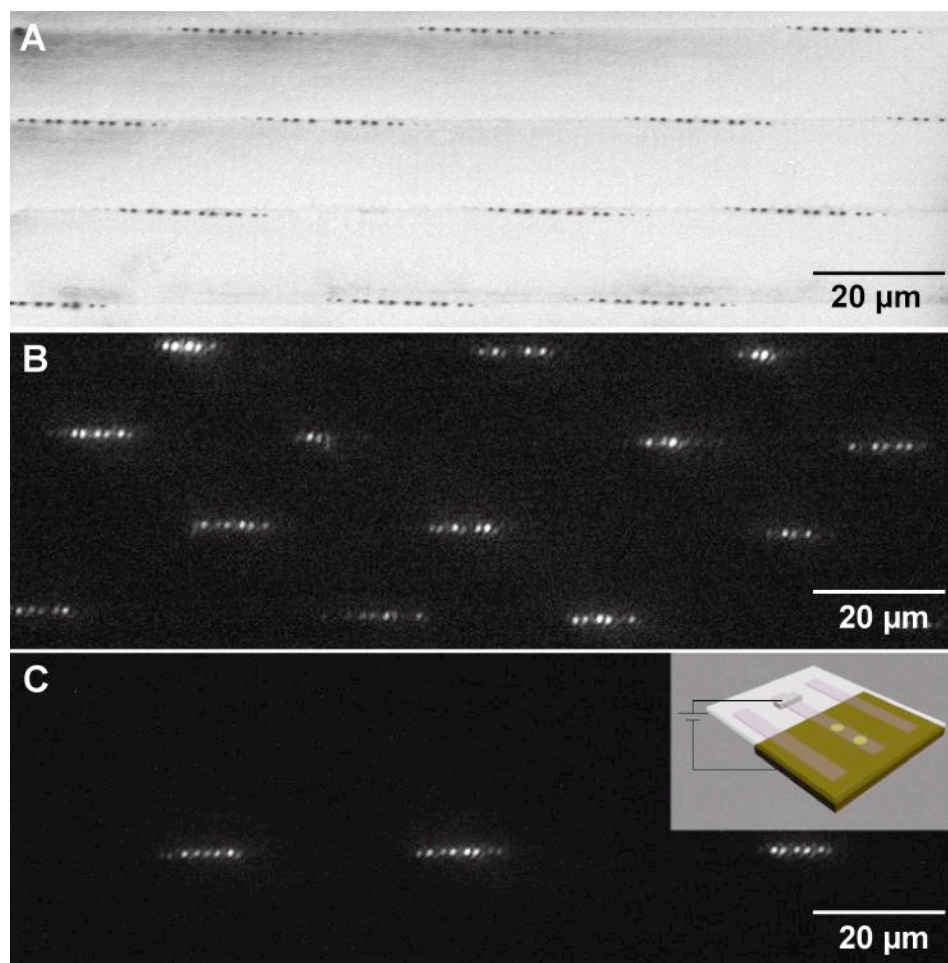


**Figure 5.3** | (A) SEM image of 250-nm circular openings in SU-8 patterned on 350-nm wide ITO lines spaced by 15 μm. The dark spots indicate where the holes are in contact with the ITO lines. (B) EL image of an array of addressable nano-OLEDs. (C) EL image of an individually addressed row of nano-OLEDs (inset: scheme of how this single row was addressed).

lines after patterning because of the challenge in manually aligning patterns with such small feature sizes. We were still able to observe EL from the nano-OLEDs in contact with the ITO even though the mismatch in alignment led to periodic discontinuities along each row (**Figure 5.3B**). By contacting a single ITO electrode, we observed EL only from nano-OLEDs in contact with this ITO line (**Figure 5.3C**). This row of nano-OLEDs is probably one of the smallest individually addressable light sources reported to date.

#### **5.4 Summary and Future Outlook**

In summary, we have developed a simple procedure to fabricate low-defect, nano-OLED arrays containing up to  $\sim 2 \times 10^7$  pixels over areas as large as  $0.7 \text{ cm}^2$ . Our patterning method has several advantages, including (1) it is parallel, and thus can be scaled up to fabricate even larger-area arrays of nano-OLEDs; (2) defects can be easily controlled using high quality PDMS photomasks; and (3) displays on flexible substrates are possible because our devices are fabricated in SU-8. One drawback is the difficulty in obtaining perfect registration between the patterned ITO lines and the SU-8 nanoholes when aligning the patterns by hand. This problem can be overcome by using more precise mechanical alignment techniques or by fabricating SU-8 hole arrays with larger spacings. Future applications of our patterning method include fully addressable nano-OLED arrays generated by patterning the cathode as well as the anode. Fabrication of arrays with individually addressable pixels is an important step toward useful high resolution devices.

## References

- (1) Maier, S. A.; Brongersma, M. L.; Kik, P. G.; Meltzer, S.; Requicha, A. A. G.; Atwater, H. A. "Plasmonics- A Route to Nanoscale Optical Devices" *Advanced Materials* **2001**, *13*, 1501-1505.
- (2) Ozbay, E. "Plasmonics: Merging Photonics and Electronics at Nanoscale Dimensions" *Science* **2006**, *311*, 189-193.
- (3) Barnes, W. L.; Dereux, A.; Ebbesen, T. W. "Surface Plasmon Subwavelength Optics" *Nature* **2003**, *424*, 824-830.
- (4) Brongersma, M. L.; Hartman, J. W.; Atwater, H. A. "Electromagnetic energy transfer and switching in nanoparticle chain arrays below the diffraction limit" *Physical Review B* **2000**, *62*, 16356-16359.
- (5) Quinten, M.; Leitner, A.; Krenn, J. R.; Aussenegg, F. R. "Electromagnetic energy transport via linear chains of silver nanoparticles" *Optics Letters* **1998**, *23*, 1331-1333.
- (6) Maier, S. A.; Barclay, P. E.; Johnson, T. J.; Friedman, M. D.; Painter, O. "Experimental demonstration of fiber-accessible metal nanoparticle plasmon waveguides for planar energy guiding and sensing" *Applied Physics Letters* **2005**, *86*, 071103.
- (7) Bozhevolnyi, S. I.; Erland, J.; Leosson, K.; Skovgaard, P. M. W.; Hvam, J. M. "Waveguiding in Surface Plasmon Polariton Band Gap Structures" *Physical Review Letters* **2001**, *86*, 3008-3011.
- (8) Ditlbacher, H.; Krenn, J. R.; Schider, G.; Leitner, A.; Aussenegg, F. R. "Two-dimensional optics with surface plasmon polaritons" *Applied Physics Letters* **2002**, *81*, 1762-1764.
- (9) Drezet, A.; Koller, D.; Hohenau, A.; Leitner, A.; Aussenegg, F. R.; Krenn, J. R. "Plasmonic Crystal Demultiplexer and Multiports" *Nano Letters* **2007**, *7*, 1697-1700.
- (10) Kitson, S. C.; Barnes, W. L.; Sambles, J. R. "A full photonic band gap for surface modes in the visible" *Physical Review Letters* **1996**, *77*, 2670-2673.
- (11) Saleh, B. E. A.; Teich, M. C. *Fundamentals of Photonics*; Wiley-Interscience, 1991.
- (12) Kawata, S. *Near-Field Optics and Surface Plasmon Polaritons*; Springer: Osaka, Japan, 2001.

- (13) Mock, J. J.; Barbic, M.; Smith, D. R.; Schultz, D. A.; Schultz, S. "Shape effects in plasmon resonance of individual colloidal silver nanoparticles" *Journal of Chemical Physics* **2002**, *116*, 6755-6759.
- (14) Lezec, H. J.; Degiron, A.; Devaux, E.; Linke, R. A.; Martin-Moreno, L.; Garcia-Vidal, F. J.; Ebbesen, T. W. "Beaming Light from a Subwavelength Aperture" *Science* **2002**, *297*, 820-822.
- (15) Bozhevolnyi, S. I.; Volkov, V. S.; Devaux, E.; Laluet, J.-Y.; Ebbesen, T. W. "Channel plasmon subwavelength waveguide components including interferometers and ring resonators" *Nature* **2006**, *440*, 508 - 511.
- (16) Bozhevolnyi, S. I.; Erland, J.; Leosson, K.; Skovgaard, P. M. W.; Hvam, J. n. M. "Waveguiding in Surface Plasmon Polariton Band Gap Structures" *Phys. Rev. Lett.* **2001**, *86*, 3008-3011.
- (17) Maier, S. A.; Brongersma, M. L.; Kik, P. G.; Meltzer, S.; Requicha, A. A. G.; Atwater, H. A. "Plasmonics-A Route to Nanoscale Optical Devices" *Adv. Mater.* **2001**, *13*, 1501-1505.
- (18) Wiley, B.; Sun, Y.; Mayers, B.; Xia, Y. "Shape-Controlled Synthesis of Metal Nanostructures: The Case of Silver" *Chemistry - A European Journal* **2004**, *11*, 454-463.
- (19) Jana, N. R.; Gearheart, L.; Murphy, C. J. "Wet chemical synthesis of silver nanorods and nanowires of controllable aspect ratio" *Chemical Communications* **2001**.
- (20) Hafner, J.; Nehl, C., Unpublished SEM image.
- (21) Ebbesen, T. W.; Lezec, H. J.; Ghaemi, H. F.; Thio, T.; Wolff, P. A. "Extraordinary optical transmission through sub-wavelength hole arrays" *Nature* **1998**, *391*, 667-669.
- (22) Lezec, H. J.; Degiron, A.; Devaux, E.; Linke, R. A.; Martin-Moreno, L.; Garcia-Vidal, F. J.; Ebbesen, T. W. "Beaming light from a subwavelength aperture" *Science* **2002**, *297*, 820-822.
- (23) Grigorenko, A. N.; Geim, A. K.; Gleeson, H. F.; Zhang, Y.; Firsov, A. A.; Khrushchev, I. Y.; Petrovic, J. "Nanofabricated media with negative permeability at visible frequencies" *Nature* **2005**, *438*, 335-338.
- (24) Dolling, G.; Wegener, M.; Soukoulis, C. M.; Linden, S. "Negative-index metamaterial at 780 nm wavelength" *Optics Letters* **2006**, *32*, 53-55.

- (25) Klein, M. W.; Enkrich, C.; Wegener, M.; Linden, S. "Second-Harmonic Generation from Magnetic Metamaterials" *Science* **2006**, *313*, 502-504.
- (26) Raether, H. *Surface Plasmons*; Springer: Berlin, 1988.
- (27) Gao, H.; Henzie, J.; Odom, T. W. "Direct Evidence for Surface Plasmon-Mediated Enhanced Light Transmission through Metallic Nanohole Arrays" *Nano Lett.* **2006**, *6*, 2104-2108.
- (28) Lamprecht, B.; Krenn, J. R.; Schider, G.; Ditlbacher, H.; Salerno, M.; Felidj, N. L. A.; Aussenegg, F. R. "Surface plasmon propagation in microscale metal stripes" *Applied Physics Letters* **2001**, *79*, 51.
- (29) Daniel, M.-C.; Astruc, D. "Gold Nanoparticles: Assembly, Supramolecular Chemistry, Quantum-Size-Related Properties, and Applications toward Biology, Catalysis, and Nanotechnology" *Chem. Rev.* **2004**, *104*, 293-346.
- (30) Xia, Y.; Halas, N. J. "Shape-Controlled Synthesis and Surface Plasmonic Properties of Metallic Nanostructures" *MRS Bull.* **2005**, *30*, 338-348.
- (31) Haes, A. J.; Haynes, C. L.; McFarland, A. D.; Schatz, G. C.; Van Duyne, R. P.; Zou, S. "Plasmonic Materials for Surface-Enhanced Sensing and Spectroscopy" *MRS Bulletin* **2005**, *30*, 368-375.
- (32) Bohren, C. F.; Huffman, D. R.; Wiley: New York, 1998, p 82.
- (33) Henzie, J.; Shuford, K. L.; Kwak, E.-S.; Schatz, G. C.; Odom, T. W. "Manipulating the Optical Properties of Pyramidal Nanoparticle Arrays" *J. Phys. Chem. B* **2006**, *110*, 14028.
- (34) Jain, P. K.; Lee, K. S.; El-Sayed, I. H.; El-Sayed, M. A. "Calculated Absorption and Scattering Properties of Gold Nanoparticles of Different Size, Shape, and Composition: Applications in Biological Imaging and Biomedicine" *J. Phys. Chem. B* **2006**, *110*, 7238-7248.
- (35) Murphy, C. J.; Sau, T. K.; Gole, A. M.; Orendorff, C. J.; Gao, J.; Gou, L.; Hunyadi, S. E.; Li, T. "Anisotropic Metal Nanoparticles: Synthesis, Assembly, and Optical Applications" *J. Phys. Chem. B* **2005**, *2005*, 13857.
- (36) Kumbhar, A. S.; Kinnan, M. K.; Chumanov, G. "Multipole Plasmon Resonances of Submicron Silver Particles" *J. Am. Chem. Soc.* **2005**, *127*, 12444-12445.
- (37) Millstone, J. E.; Park, S.; Shuford, K. L.; Qin, L.; Schatz, G. C.; Mirkin, C. A. "Observation of a Quadrupole Plasmon Mode for a Colloidal Solution of Gold Nanoprisms" *J. Am. Chem. Soc.* **2005**, *127*, 5312-5313.

- (38) Shuford, K. L.; Ratner, M. A.; Schatz, G. C. "Multipolar excitation in triangular nanoprisms" *J. Chem. Phys.* **2005**, *123*, 114713.
- (39) Kelly, K. L.; Coronado, E.; Zhao, L. L.; Schatz, G. C. *J. Phys. Chem. B* **2003**, *107*, 668.
- (40) Krenn, J. R.; Schider, G.; Rechberger, W.; Lamprecht, B.; Leitner, A.; Aussenegg, F. R.; Weeber, J. C. "Design of multipolar plasmon excitations in silver nanoparticles" *Appl. Phys. Lett.* **2000**, *77*, 3379-3381.
- (41) Wiley, B.; Sun, Y.; Chen, J.; Cang, H.; Li, Z.; Li, X.; Xia, Y. "Shape-Controlled Synthesis of Silver and Gold Nanostructures" *MRS Bulletin* **2005**, *30*, 356-361.
- (42) Shevchenko, E. V.; Talapin, D. V.; Kotov, N. A.; O'Brien, S.; Murray, C. B. "Structural diversity in binary nanoparticle superlattices" *Nature* **2006**, *439*, 55.
- (43) Klajin, R.; Bishop, K. J. M.; Grzybowski, B. A. "Light-controlled self-assembly of reversible and irreversible nanoparticle suprastructures" *Proceedings of the National Academy of Sciences* **2007**, *104*, 10305-10309.
- (44) Collier, C. P.; Saykally, R. J.; Shiang, J. J.; Henrichs, S. E.; Heath, J. R. "Reversible Tuning of Silver Quantum Dot Monolayers Through the Metal-Insulator Transition" *Science* **1997**, *277*, 1978-1981.
- (45) Tao, A. R.; Sinsermsuksakul, P.; Yang, P. "Tunable plasmonic lattices of silver nanocrystals" *Nature Nanotechnology* **2007**, *2*, 435.
- (46) Hicks, E. M.; Zou, S.; Schatz, G. C.; Spears, K. G.; Van Duyne, R. P.; Gunnarson, L.; Rindzevicius, T.; Kasemo, B.; Kall, M. "Controlling Plasmon Line Shapes through Diffractive Coupling in Linear Arrays of Cylindrical Nanoparticles Fabricated by Electron Beam Lithography" *Nano Lett.* **2005**, *5*, 1065-1070.
- (47) Haynes, C. L.; McFarland, A. D.; Zhao, L.; Van Duyne, R. P.; Schatz, G. C.; Gunnarsson, L.; Prikulis, J.; Kasemo, B.; Kaell, M. "Nanoparticle Optics: The Importance of Radiative Dipole Coupling in Two-Dimensional Nanoparticle Arrays" *Journal of Physical Chemistry B* **2003**, *107*, 7337-7342.
- (48) Gunnarsson, L.; Rindzevicius, T.; Prikulis, J.; Kasemo, B.; Kall, M.; Zou, S.; Schatz, G. C. "Confined Plasmons in Nanofabricated Single Silver Particle Pairs: Experimental Observations of Strong Interparticle Interactions" *Journal of Physical Chemistry B* **2005**, *109*, 1079-1087.

- (49) Grupp, D. E.; Lezec, H. J.; Thio, T.; Ebbesen, T. W. "Beyond the Bethe Limit: Tunable Enhanced Light Transmission Through a Single Sub-Wavelength Aperture" *Adv. Mater.* **1999**, *11*, 860-862.
- (50) Xia, Y.; Whitesides, G. M. "Soft lithography" *Annual Review of Materials Science* **1998**, *28*, 153-184.
- (51) Schimid, H.; Michel, B. "Siloxane Polymers for High-Resolution, High-Accuracy Soft Lithography" *Macromolecules* **2000**, *33*, 3042-3049.
- (52) Odom, T. W.; Love, J. C.; Paul, K. E.; Wolfe, D. B.; Whitesides, G. M. "Improved Pattern Transfer in Soft Lithography Using Composite Stamps" *Langmuir* **2002**, *18*, 5314.
- (53) Kwak, E.-S.; Henzie, J.; Chang, S.-H.; Gray, S. K.; Schatz, G. C.; Odom, T. W. "Surface Plasmon Standing Waves in Large-Area Subwavelength Hole Arrays" *Nano Letters* **2005**.
- (54) Odom, T. W.; Thalladi, V. R.; Love, J. C.; Whitesides, G. M. "Generation of 30-50 nm Structure Using Easily Fabricated, Composite PDMS Masks" *J. Am. Chem. Soc.* **2002**, *124*, 12112-12113.
- (55) Stender, C. L.; Greyson, E. C.; Odom, T. W. "Patterned MoS<sub>2</sub>-Nanostructures over cm<sup>2</sup>-Areas" *Advanced Materials In Press*, I.
- (56) Henzie, J.; Kwak, E.-S.; Odom, T. W. "Mesoscale Metallic Pyramids with Nanoscale Tips" *Nano Letters* **2005**, *5*, 1199-1202.
- (57) Greyson, E. C.; Babayan, Y.; Odom, T. W. "Directed growth of ordered arrays of small-diameter ZnO nanowires" *Advanced Materials (Weinheim, Germany)* **2004**, *16*, 1348-1352.
- (58) Gates, B. D.; Xu, Q.; Love, C. J.; Wolfe, D. B.; Whitesides, G. M. "Unconventional Nanofabrication" *Annual Review of Materials Research* **2004**, *34*, 339-372.
- (59) Love, C. J.; Wolfe, D. B.; Chabynyc, M. L.; Paul, K. E.; Whitesides, G. M. "Self-Assembled Monolayers of Alkanethiolates on Palladium Are Good Etch Resists" *Journal of the American Chemical Society* **2002**, *124*, 1576-1577.
- (60) Xia, Y.; Zhao, X.-M.; Whitesides, G. M. "Pattern transfer: Self-assembled monolayers as ultrathin resists" *Microelectronics Engineering* **1996**, *32*, 255-268.

- (61) Odom, T. W.; Love, C. J.; Wolfe, D. B.; Paul, K. E.; Whitesides, G. M. "Improved Pattern Transfer in Soft Lithography Using Composite Stamps" *Langmuir* **2002**, *18*, 5314-5320.
- (62) Childs, W. R.; Nuzzo, R. G. "Large-Area Patterning of Coinage-Metal Thin Films Using Decal Transfer Lithography" *Langmuir* **2005**, *21*, 195-202.
- (63) Loo, Y.-L.; Willett, R. L.; Baldwin, K. W.; Rogers, J. A. "Interfacial Chemistries for Nanoscale Transfer Printing" *Journal of the American Chemical Society* **2002**, *124*, 7654-7655.
- (64) Zaumseil, J.; Meitl, M. A.; Hsu, J. W. P.; Acharya, B. R.; Baldwin, K. W.; Loo, Y.-L.; Rogers, J. A. "Three-Dimensional and Multilayer Nanostructures Formed by Nanotransfer Printing" *Nano Letters* **2003**, *3*, 1223-1227.
- (65) Xu, Q.; Bao, J.; Rioux, R. M.; Perez-Castillejos, R.; Capasso, F.; Whitesides, G. M. "Fabrication of Large-Area Patterned Nanostructures for Optical Applications by Nanoskiving" *Nano Letters* **2007**, *7*, 2800-2805.
- (66) Stewart, M. E.; Mack, N. H.; Malyarchuk, V.; Soares, J. A. N. T.; Lee, T.-W.; Gray, S. K.; Nuzzo, R. G.; Rogers, J. A. "Quantitative multispectral biosensing and 1D imaging using quasi-3D plasmonic crystals" *Proceedings of the National Academy of Sciences of the United States of America* **2006**, *103*, 17143-17148.
- (67) Bethe, H. A. "Theory of diffraction by small holes" *Physical Review* **1944**, *66*, 163-182.
- (68) Genet, C.; Ebbesen, T. W. "Light in tiny holes" *Nature* **2006**, *445*, 39-46.
- (69) Ritchie, R. H. "Plasma Losses by Fast Electrons in Thin Films" *Physical Review* **1957**, *106*.
- (70) Chang, S.-H.; Gray, S. K.; Schatz, G. C. "Surface plasmon generation and light transmission by isolated nanoholes and arrays of nanoholes in thin metal films" *Opt. Comm.* **2005**.
- (71) Pendry, J. B.; Martín-Moreno, L.; Garcia-Vidal, F. J. "Mimicking Surface Plasmons with Structured Surfaces" *Science* **2005**, *305*, 847-848.
- (72) Garcia-Vidal, F. J.; Martín-Moreno, L.; Pendry, J. B. "Surfaces with holes in them: new plasmonic metamaterials" *Journal of Optics A* **2005**, *7*, S97-S101.

- (73) Jensen, T.; Duval, M.; Kelly, K.; Lizarides, A.; Schatz, G. C.; Van Duyne, R. P. "Nanosphere Lithography: Effect of the External Dielectric Medium on the Surface Plasmon Resonance Spectrum of a Periodic Array of Silver Nanoparticles" *J. Phys. Chem. B* **1999**, *103*, 9846-9853.
- (74) Novotny, L.; Bian, R. X.; Xie, X. S. "Theory of Nanometric Optical Tweezers" *Physical Review Letters* **1997**, *79*.
- (75) Kelly, K.; Coronado, E.; Zhao, L. L.; Schatz, G. C. "The Optical Properties of Metal Nanoparticles: The Influence of Size, Shape, and Dielectric Environment" *Journal of Physical Chemistry B* **2003**, *107*, 668-677.
- (76) Fischer, U. C.; Dereux, A.; Weeber, J. C. *Near-Field Optics and Surface Plasmon Polaritons* Berlin, 20001; Vol. 81.
- (77) Bian, R. X.; Dunn, R. C.; Xie, X. S.; Leung, P. T. "Single Molecule Emission Characteristics in Near-Field Microscopy" *Physical Review Letters* **1995**, *75*, 4772-4775.
- (78) Bohren, C. F.; Huffman, D. R. *Absorption and Scattering of Light by Small Particles*; Wiley: New York, 1998.
- (79) Nehl, C. L.; Grady, N. K.; Goodrich, G. P.; Tam, F.; Halas, N. J.; Hafner, J. H. "Scattering Spectra of Single Gold Nanoshells" *Nano Letters* **2004**, *4*, 2355-2359.
- (80) Charnay, C.; Lee, A.; Man, S.-Q.; Moran, C. E.; Radloff, C.; Bradley, R. K.; Halas, N. J. "Reduced symmetry metallodielectric nanoparticles: chemical synthesis and plasmonic properties" *Journal of Physical Chemistry B* **2003**, *107*, 7327-7333.
- (81) Krenn, J. R.; Dereux, A.; Weeber, J. C.; Bourillot, Y. L.; Goudonnet, J. P. "Squeezing the Optical Near-Field Zone by Plasmon Coupling of Metallic Nanoparticles" *Phys. Rev. Lett.* **1999**, *82*, 2590-2593.
- (82) Genolet, G.; Despont, M.; Vettiger, P.; Anselmetti, D.; Rooij, N. F. D. "All-photoplastic, soft cantilever cassette probe for scanning force microscopy" *Journal of Vacuum Science and Technology B* **2000**, *18*.
- (83) Hulteen, J. C.; Martin, C. R. J. "A general template-based method for the preparation of nanomaterials" *Journal of Materials Chemistry* **1997**, *7*, 1075-1087.
- (84) Nicewarner-Pena, S. R.; Freeman, R. G.; Reiss, B. D.; He, L.; Pena, D. J.; Walton, I. D.; Cromer, R.; Keating, C. D.; Natan, M. J. "Submicrometer Metallic Barcodes" *Science* **2001**, *294*, 137-141.
- (85) Park, S.; Lim, J.-H.; Chung, S.-W.; Mirkin, C. A. "Self-Assembly of Mesoscopic Metal-Polymer Amphiphiles" *Science* **2004**, *303*, 348-351.

- (86) Xu, Q.; Tonks, I.; Fuerstman, M. J.; Love, J. C.; Whitesides, G. M. "Fabrication of Free-Standing Metallic Pyramidal Shells" *Nano Letters* **2004**, *4*, 2509-2511.
- (87) Love, J. C.; Gates, B. D.; Wolfe, D. B.; Paul, K. E.; Whitesides, G. M. "Fabrication and wetting properties of metallic half-shells with submicron diameters" *Nano Letters* **2002**, *2*.
- (88) Lu, Y.; Lui, G. L.; Kim, J.; Mejia, Y. X.; Lee, L. P. "Nanophotonic Crescent Moon Structures with Sharp Edge for Ultrasensitive Biomolecular Detection by Local Electromagnetic Field Enhancement Effect " *Nano Letters* **2005**, *5*, 119-124.
- (89) Henzie, J.; Kwak, E. S.; Odom, T. W. "Mesoscale metallic pyramids with nanoscale tips" *Nano Letters* **2005**, *5*, 1199-1202.
- (90) Kwak, E. S.; Henzie, J.; Chang, S. H.; Gray, S. K.; Schatz, G. C.; Odom, T. W. "Surface Plasmon Standing Waves in Large-Area Subwavelength Hole Arrays" *Nano Lett.* **2005**, *5*, 1963-1967.
- (91) Odom, T. W.; Love, J. C.; Wolfe, D. B.; Paul, K. E.; Whitesides, G. M. *Langmuir* **2002**, *18*, 5314-5320.
- (92) Odom, T. W.; Love, J. C.; Thalladi, V. R.; Whitesides, G. M. "Generation of 30-50 nm Structures using Easily Fabricated, Composite PDMS Masks" *J. Am. Chem. Soc.* **2002**, *124*, 12211-12.
- (93) Greyson, E. C.; Babayan, Y.; Odom, T. W. *Adv. Mater.* **2004**, *16*, 1348-1352.
- (94) Henzie, J.; Shuford, K. L.; Kwak, E.-S.; Schatz, G. C.; Odom, T. W. "Manipulating the Optical Properties of Pyramidal Nanoparticle Arrays" *Journal of Physical Chemistry B* **2006**, *110*, 14028-14031.
- (95) Hasan, W.; Lee, J.; Henzie, J.; Odom, T. W. "Selective Functionalization and Spectral Identification of Gold Nanopyramids" *Journal of Physical Chemistry C* **2007**, *111*, 17176-17179.
- (96) Barnes, W. L.; Dereux, A.; Ebbesen, T. W. "Surface plasmon subwavelength optics" *Nature* **2003**, *424*, 824 - 830.
- (97) Devaux, E.; Ebbesen, T. W.; Weeber, J.-C.; Dereux, A. "Launching and decoupling surface plasmons via micro-gratings" *Appl. Phys. Lett.* **2003**, *83*, 4936-4938.

- (98) Chang, S.-H.; Gray, S. K.; Schatz, G. C. "Surface plasmon generation and light transmission by isolated nanoholes and arrays of nanoholes in thin metal films" *Opt. Express* **2005**, *13*, 3150.
- (99) Williams, S. M. R., K. R.; Teeters-Kennedy, S.; Stafford, A. D.; Bishop, S. R.; Lincoln, U. K.; Coe, J. V. "Use of the Extraordinary Infrared Transmission of Metallic Subwavelength Arrays To Study the Catalyzed Reaction of Methanol to Formaldehyde on Copper Oxide" *J. Phys. Chem. B* **2004**, *108*, 11833-11837.
- (100) Brolo, A. G.; Gordon, R.; Leathem, B.; Kavanah, K. L. "Surface Plasmon Sensor Based on the Enhanced Light Transmission through Arrays of Nanoholes in Gold Films" *Langmuir* **2004**, *20*, 4813-4815.
- (101) Brolo, A. G.; Arctander, E.; Gordan, R.; Leathem, V.; Kavanaugh, K. "Nanohole-enhanced Raman Scattering" *Nano Letters* **2005**, *4*, 2015-2018.
- (102) Odom, T. W.; Love, J. C.; Wolfe, D. B.; Paul, K. E.; Whitesides, G. M. *Langmuir* **2002**, *18*, 5314.
- (103) Odom, T. W.; Love, J. C.; Thalladi, V. R.; Whitesides, G. M. *J. Am. Chem. Soc.* **2002**, *124*, 12211.
- (104) Henzie, J.; Kwak, E.-S.; Odom, T. W. "Mesoscale Metallic Pyramids with Nanoscale Tips" *Nano Letters* **2005**, *ASAP*.
- (105) Hecht, B.; Bielefeldt, H.; Novotny, L.; Inouye, Y.; Pohl, D. W. "Local Excitation, Scattering, and Interference of Surface Plasmons" *Phys. Rev. Lett.* **1996**, *77*, 1889-1892.
- (106) Yin, L.; Vlasko-Vlasov, V. K.; Rydh, A.; Pearson, J.; Welp, U.; Chang, S.-H.; Gray, S. K.; Schatz, G. C.; Brown, D. B.; Kimball, C. W. "Surface plasmons at single nanoholes in Au films" *Appl. Phys. Lett.* **2004**, *85*, 467-469.
- (107) Chang, S.-H.; Gray, S. K.; Schatz, G. C. "Surface plasmon generation and light transmission by isolated nanoholes and arrays of nanoholes in thin metal films" *Optics Express* **2005**, *13*, 3150-3165.
- (108) Ordal, M. A.; Long, L. L.; Bell, R. J.; Bell, S. E.; Bell, R. R.; Alexander, R. W.; Ward, C. A. "Optical properties of the metals Al, Co, Cu, Au, Fe, Pb, Ni, Pd, Pt, Ag, Ti, and W in the infrared and far infrared" *Applied Optics* **1983**, *22*, 1099-1120.
- (109) Hecht, B.; Bielefeldt, H.; Novotny, L.; Inouye, Y.; Pohl, D. W. *Phys. Rev. Lett.* **1996**, *77*, 1889.

- (110) Martin-Moreno, L.; Garcia-Vidal, F. J.; Lezec, H. J.; Pellerin, K. M.; Thio, T.; Pendry, J. B.; Ebbesen, T. W. "Theory of Extraordinary Optical Transmission through Subwavelength Hole Arrays" *Phys. Rev. Lett.* **2001**, *86*, 1114-1117.
- (111) Cao, C.; Lalanne, P. "Negative Role of Surface Plasmons in the Transmission of Metallic Gratings with Very Narrow Slits" *Physical Review Letters* **2002**, *88*, 057403.
- (112) Lezec, H. J.; Thio, T. "Diffracted evanescent wave model for enhanced and suppressed optical transmission through subwavelength hole arrays" *Optics Express* **2004**, *12*, 3629-3651.
- (113) Sarrazin, M.; Vigneron, J.-P. "Light transmission assisted by Brewster-Zennek modes in chromium films carrying a subwavelength hole array" *Physical Review B* **2005**, *71*, 075404.
- (114) Prikulis, J.; Hanarp, P.; Olofsson, L.; Sutherland, D.; Kall, M. "Optical Spectroscopy of Nanometric Holes in Thin Gold Films" *Nano Letters* **2004**, *4*, 1003-1007.
- (115) Gao, H.; Henzie, J.; Odom, T. W. "Direct evidence for surface plasmon-mediated enhanced light transmission through metallic nanohole arrays" *Nano Letters* **2006**, *6*, 2104-2108.
- (116) Chang, S.-H.; Gray, S. K.; Schatz, G. C. "Surface plasmon generation and light transmission by isolated nanoholes and arrays of nanoholes in thin metal films" *Optics Express*, *13*, 3150-3165.
- (117) Kwak, E. S.; Henzie, J.; Chang, S. H.; Gray, S. K.; Schatz, G. C.; Odom, T. W. "Surface Plasmon Standing Waves in Large-Area Subwavelength Hole Arrays" *Nano Letters* **2005**, *5*, 1963.
- (118) Barnes, W. L.; Dereux, A.; Ebbesen, T. W. "Surface Plasmon Subwavelength Optics" *Nature* **2003**, *424*, 824-830.
- (119) Smith, H. I.; Hector, S. D.; Schattenburg, M. L.; Anderson, E. H. "A New Approach to High Fidelity E-Beam Lithography Based on an In-Situ, Global Fiducial Grid" *J. Vac. Sci. Technol. B* **1991**, *9*, 2992-2995.
- (120) Xia, Y.; Whitesides, G. M. "Soft Lithography" *Angewandte Chemie International Edition* **1998**, *37*, 550-575.
- (121) Liao, H.; Nehl, C. L.; Hafner, J. H. "Biomedical applications of plasmon resonant metal nanoparticles" *Nanomedicine* **2006**, *1*, 201-208.

- (122) Odom, T. W.; Love, J. C.; Wolfe, D. B.; Paul, K. E.; Whitesides, G. M. "Improved pattern transfer in soft lithography using composite stamps" *Langmuir* **2002**, *18*, 5314-5320.
- (123) Gao, H.; Henzie, J.; Odom, T. W. "Direct evidence for surface plasmon-mediated enhanced light transmission through metallic nanohole arrays" *Nano Letters* **2006**, *6*, 2104-2108.
- (124) Henzie, J.; Kwak, E. S.; Odom, T. W. "Mesoscale metallic pyramids with nanoscale tips" *Nano Letters* **2005**, *5*, 1199-1202.
- (125) van der Molen, K. L.; Segerink, F. B.; van Hulst, N. F.; Kuipers, L. "Influence of hole size on the extraordinary transmission through subwavelength hole arrays" *Applied Physics Letters* **2004**, *85*, 4316-4318.
- (126) Krishnan, A.; Thio, T.; Kim, T. J.; Lezec, H. J.; Ebbesen, T. W.; Wolff, P. A.; Pendry, J.; Martin-Moreno, L.; Garcia-Vidal, F. J. "Evanescently coupled resonance in surface plasmon enhanced transmission" *Optics Communications* **2001**, *200*, 1-7.
- (127) Sherry, L. J.; Chang, S.-H.; Schatz, G. C.; Van Duyne, R. P.; Wiley, B. J.; Xia, Y. "Localized Surface Plasmon Resonance Spectroscopy of Single Silver Nanocubes" *Nano Letters* **2005**, *5*, 2034-2038.
- (128) Hicks, E. M.; Zhang, X.; Zou, S.; Lyandres, O.; Spears, K. G.; Schatz, G. C.; Van Duyne, R. P. "Plasmonic Properties of Film over Nanowell Surfaces Fabricated by Nanosphere Lithography" *Journal of Physical Chemistry B* **2005**, *109*, 22351-22358.
- (129) Zayats, A. V., Personal communication.
- (130) Lakowicz, J. R. "Radiative decay engineering 5: metal-enhanced fluorescence and plasmon emission" *Analytical Biochemistry* **2005**, *337*, 171-194.
- (131) Anger, P.; Bharadwaj, P.; Novotny, L. "Enhancement and Quenching of Single-Molecule Fluorescence" *Physical Review Letters* **2006**, *96*, 113002.
- (132) Stephens, D. J.; Allan, V. J. "Light Microscopy Techniques for Live Cell Imaging" *Science* **2003**, *300*, 82-86.
- (133) Wang, H.; Brandl, D. W.; Nordlander, P.; Halas, N. J. "Plasmonic Nanostructures: Artificial Molecules" *Accounts of Chemical Research* **2007**, *40*, 53-62.
- (134) Basano, L.; Ottonello, P. "Demonstration experiments on nondiffracting beams generated by thermal light" *American Journal of Physics* **2005**, *73*, 826-830.

- (135) McGloin, D.; Dholakia, C. T. A. "Bessel beams: diffraction in a new light" *Contemporary Physics* **2005**, *46*, 15-28.
- (136) Shen, Z. L.; Burrows, P. E.; Bulovic, V.; Forrest, S. R.; Thompson, M. E. "Three-color, tunable, organic light-emitting devices" *Science* **1997**, *276*, 2009-2011.
- (137) Gustafsson, G.; Cao, Y.; Treacy, G. M.; Klavetter, F.; Colaneri, N.; Heeger, A. J. "Flexible Light-Emitting-Diodes Made from Soluble Conducting Polymers" *Nature* **1992**, *357*, 477-479.
- (138) Howard, W. E.; Prache, O. F. "Microdisplays based upon organic light-emitting diodes" *Ibm Journal of Research and Development* **2001**, *45*, 115-127.
- (139) Granstrom, M.; Berggren, M.; Inganas, O. "Micrometer-Sized and Nanometer-Sized Polymeric Light-Emitting-Diodes" *Science* **1995**, *267*, 1479-1481.
- (140) Boroumand, F. A.; Fry, P. W.; Lidzey, D. G. "Nanoscale conjugated-polymer light-emitting diodes" *Nano Letters* **2005**, *5*, 67-71.
- (141) Yamamoto, H.; Wilkinson, J.; Long, J. P.; Bussman, K.; Christodoulides, J. A.; Kafafi, Z. H. "Nanoscale organic light-emitting diodes" *Nano Letters* **2005**, *5*, 2485-2488.
- (142) Veinot, J. G. C.; Yan, H.; Smith, S. M.; Cui, J.; Huang, Q. L.; Marks, T. J. "Fabrication and properties of organic light-emitting "nanodiode" arrays" *Nano Letters* **2002**, *2*, 333-335.
- (143) Gao, F. G.; Bard, A. J. "Solid-state organic light-emitting diodes based on tris(2,2'-bipyridine)ruthenium(II) complexes" *Journal of the American Chemical Society* **2000**, *122*, 7426-7427.
- (144) Rudmann, H.; Rubner, M. F. "Single layer light-emitting devices with high efficiency and long lifetime based on tris(2,2'-bipyridyl) ruthenium(II) hexafluorophosphate" *Journal of Applied Physics* **2001**, *90*, 4338-4345.
- (145) Rudmann, H.; Shimada, S.; Rubner, M. F. "Solid-state light-emitting devices based on the tris-chelated ruthenium(II) complex. 4. High-efficiency light-emitting devices based on derivatives of the tris(2,2'-bipyridyl) ruthenium(II) complex" *Journal of the American Chemical Society* **2002**, *124*, 4918-4921.
- (146) Kalyuzhny, G.; Buda, M.; McNeill, J.; Barbara, P.; Bard, A. J. "Stability of thin-film solid-state electroluminescent devices based on tris(2,2'-bipyridine)ruthenium(II) complexes" *Journal of the American Chemical Society* **2003**, *125*, 6272-6283.

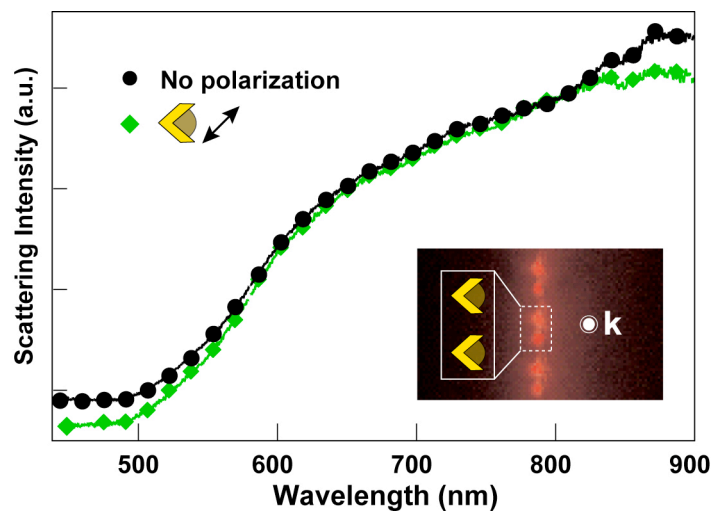
(147) Liu, C. Y.; Bard, A. J. "Individually addressable submicron scale light-emitting devices based on electroluminescence of solid Ru(bpy)<sub>3</sub>(ClO<sub>4</sub>)<sub>2</sub> films" *Journal of the American Chemical Society* **2002**, *124*, 4190-4191.

(148) Liu, C. Y.; Bard, A. J. "Highly efficient and bright electroluminescent Ru(bpy)<sub>3</sub>(ClO<sub>4</sub>)<sub>2</sub>/Alq<sub>3</sub> device" *Applied Physics Letters* **2005**, *87*, 061110.

(149) Henzie, J.; Barton, J. E.; Stender, C. L.; Odom, T. W. "Large-area Nanoscale Patterning: Chemistry meets Fabrication" *Accounts of Chemical Research* **2006**, *39*, 249-257.

(150) Odom, T. W.; Thalladi, V. R.; Love, J. C.; Whitesides, G. M. "Generation of 30-50 nm structures using easily fabricated, composite PDMS masks" *Journal of the American Chemical Society* **2002**, *124*, 12112-12113.

## APPENDIX I



Comparison of spectra with pyramids in orientation **II** revealed that the spectra acquired when the polarization vector was  $45^\circ$  was very similar to the spectra produced from unpolarized white light and was roughly the average of spectra from parallel and perpendicular polarization directions (compare with **Figure 2.9**).

## Joel Henzie

### EDUCATION

- B.S. 2000 University of Nebraska-Lincoln
- Ph.D. expected December 2007 Northwestern University

### PROFESSIONAL EXPERIENCE

- 2003-Present Research Assistant (Northwestern University, with Teri Odom)
- 2003 Teaching Assistant (Northwestern University)
- 2001-2003 Research Assistant (Arizona State University, with Devens Gust)
- 2000 Research Assistant (Columbia University, with Kenneth Eissenthal)
- 2000 Research Assistant (Biosphere 2 Center, with Leonard Fine)
- 1997-2000 Research Assistant (University of Nebraska-Lincoln, with Catherine Chia)

### HONORS AND AWARDS

- 2005-2007 Northwestern University Materials Research and Engineering Center (NU-MRSEC) Fellowship
- 2007 1<sup>st</sup> place prize at the Spring Materials Research Society (MRS) *Science as Art* competition
- 2006 NSF scholarship to attend the 56<sup>th</sup> Lindau Meeting of the Nobel Laureates in Germany
- 2004 Suchanski Fellowship, Northwestern University
- 2001-2002 National Science Foundation Integrative Graduate Education and Research Traineeship (NSF-IGERT), Arizona State University
- 2000 NSF Undergraduate Research Fellowship (NSF-REU), Columbia University
- 2000 Volvo Scholarship, Columbia University
- 1998 Howard Hughes Medical Institute (HHMI) Undergraduate Research Fellowship, University of Nebraska-Lincoln
- 1998 Beach-Byer Scholarship, University of Nebraska-Lincoln
- 1997 Mohr Research Scholarship, University of Nebraska-Lincoln

### PROFESSIONAL MEMBERSHIPS

American Chemical Society, American Physical Society, International Union of Pure and Applied Chemistry, Materials Research Society

### PUBLICATIONS

1. Lee, J., **Henzie, J.**; Odom, T. W.; *Manipulating the Optical Properties of*

- Individual and Arrays of Gold Nanopyramids*. [Book Chapter in “Nanostructures in Electronics and Photonics,” In Press (Pan Stanford Publications, Singapore); ed. F. Rahman.
2. **Henzie, J.**; Lee, M. H.; Odom, T. W.; *Multiscale Fabrication of Plasmonic Structures*. [Book Chapter, In Press (Wiley); ed. John A. Rogers]
  3. McMahan, J. M.; **Henzie, J.**; Odom, T. W.; Schatz, G. C.; Gray, S. K.; *Ultra-narrow Resonances from Wood’s Anomaly-Surface Plasmon Excitation Coupling in Thin Gold Films of Nanohole Arrays*. [Accepted (Optics Express)]
  4. Lee, M. H.; Gao, H.; **Henzie, J.**; Odom, T. W.; *Microscale Arrays of Nanoscale Holes*; Small; [Early View; doi: 10.1002/sml.200700499]
  5. Hasan, W.; Lee, J.; **Henzie, J.**; Odom, T. W.; *Selective Functionalization and Spectral Identification of Gold Nanopyramids*; J. Phys. Chem. C.; **2007**; ASAP
  6. **Henzie, J.**; Lee, M.H.; Odom, T. W.; *Multiscale Patterning of Plasmonic Metamaterials*; Nature Nanotech.; **2007**; 2, 549-554. [Featured on the Cover]
  7. Price, S.; **Henzie, J.**; Odom, T. W.; *Addressable, Large-Area Nanoscale Organic Light-Emitting Diodes*; Small; **2007**; 3, 372-374.
  8. Gao, H.; **Henzie, J.**; Odom, T. W.; *Direct Evidence for Surface-Plasmon Mediated Enhanced Light Transmission through Metallic Nanohole Arrays*; Nano Lett.; **2006**; 6, 2104-2108.
  9. **Henzie, J.**; Shuford, K. L.; Kwak, E.-S.; Schatz, G. C.; Odom, T. W.; *Manipulating the Optical Properties of Pyramidal Nanoparticle Arrays*; J. Phys. Chem. B; **2006**; 110, 14028-14031.
  10. **Henzie, J.**; Barton, J. B.; Stender, C. L.; Odom, T. W. *Large-area Nanoscale Patterning: Chemistry meets Fabrication*; Acct. Chem. Res.; **2006**; 39, 249-257.
  11. **Henzie, J.**; Kwak, E.-S.; Chang, S.-H.; Gray, S. K.; Schatz, G. C.; Odom, T. W.; *Surface Plasmon Standing Waves in Large-Area Subwavelength Hole Arrays*; Nano Lett.; **2005**; 5; 1963-1967.
  12. Odom, T. W., **Henzie, J.**, Babayan, Y., Greyson, E. C., Kwak, E.-S.; *Optical Properties of Surface-Patterned Nanostructures*; Talanta; **2005**; 67, 507-513.
  13. **Henzie, J.**; Kwak, E.-S.; Odom, T. W.; *Mesoscale Metallic Pyramids with Nanoscale Tips*; Nano Lett.; **2005**; 5(7); 1199-1202.
  14. Benderskii, A. V.; **Henzie, J.**; Basu, S.; Shang, X.; Eisenthal, K. B.; *Femtosecond Aqueous Solvation at a Positively Charged Surfactant/Water Interface*; J. Phys. Chem. B.; **2004**; 108(37); 14017-14024.

## PATENTS

1. *Preparation of mesoscale pyramid structures and arrays, and methods of isolation to facilitate characterization of orientation-dependent optical properties* Odom, T. W.; **Henzie, J.**; Kwak, E.-S. US 2007111366.
2. *Preparation of large-area subwavelength hole arrays* Odom, T. W.; **Henzie, J.**;

Kwak, E.-S.; Lee, M.-H.; NU25039, *Patent Pending*.

#### PRESENTATIONS AND POSTERS

1. Henzie, J.; Odom, T. W. *Soft interference lithography: A large-scale platform for nanophotonics*. ACS National Meeting. Spring 2007 [Presentation]
2. Henzie, J. Odom, T.W. *Manipulating the optical properties of gold nanopyramids*. GRC, Nanostructure Fabrication. 2006 [Poster]
3. Henzie, J. Odom, T.W. *Mesoscale metallic pyramids with nanoscale tips*. GRC, Clusters, Nanocrystals, and Nanostructures. 2005 [Poster]